

Dissertation
submitted to the
Combined Faculties of the Natural Sciences and Mathematics
of the Ruperto-Carola-University of Heidelberg. Germany
for the degree of
Doctor of Natural Sciences

Put forward by
Alda Lisseth Arias Suárez
born in: Chinácota

Oral examination: 17th of april, 2019

Probing the non-equilibrium dynamics and coherence properties of Rydberg-enhanced gases

Referees:

Prof. Dr. Shannon Whitlock

Prof. Dr. Markus Oberthaler

Alda Lisseth Arias Suarez

Probing the non-equilibrium dynamics and coherence properties of Rydberg-enhanced gases

Documentation, February 4, 2019

Referees: Prof. Dr. Shannon Whitlock and Prof. Dr. Markus Oberthaler

Supervisor: Prof. Dr. Shannon Whitlock

Heidelberg University

Physikalisches Institut

Department of physics and astronomy

Im Neuenheimer Feld 226

69120 Heidelberg

A quienes me dieron la vida, el coraje
y la motivación para realizar mis sueños.
Todo es gracias a ellos y para ellos . . .

List of publications

The results presented in this thesis are based on the following manuscripts and peer-reviewed publications:

- **Realization of a Rydberg-dressed Ramsey interferometer and electrometer**
A. Arias, G. Lothead, T. M. Wintermantel, S. Helmrich, S. Whitlock
Physical Review Letters 122, 053601 (2019)
- **A versatile, high-power 460nm laser system for Rydberg excitation of ultracold potassium**
A. Arias, S. Helmrich, C. Schweiger, L. Ardizzone, G. Lothead, S. Whitlock
Optics Express, Vol. 25, Issue 13, pp. 14829-14839 (2017)
- **Uncovering the nonequilibrium phase structure of an open quantum spin system**
S. Helmrich, A. Arias, and S. Whitlock
Physical Review A 98, 022109 (2018)
- **Observation of Self-Organised Criticality in an Ultracold Atomic Gas S.**
Helmrich, A. Arias, G. Lothead, M. Buchhold, S. Diehl, S. Whitlock
arXiv:1806.09931v1
- **Two-body interactions and decay of three-level Rydberg-dressed atoms**
S Helmrich, A Arias, N Pehoviak and S Whitlock
Journal of Physics B: Atomic, Molecular and Optical Physics, Vol. 49, (2016)

Abstract

This thesis describes studies on a Rydberg-dressed ultracold atom system as a versatile platform for non-equilibrium physics research, atom-light interactions analysis and atomic sensing applications. This work includes a description of the experimental system, an ultracold potassium atom setup where we can prepare a gas of atoms in an optical dipole trap and precisely control their ground state properties. To excite the atoms to strongly-interacting Rydberg states, we set up and characterize a high-power and widely tunable excitation laser system, for driving both single and two-photon Rydberg excitations. Together this establishes a unique system for studying the effects of driving, long-range interactions and dissipation (due to the relatively short lifetime of excited states) on many-body dynamics. Using this setup we study the phase structure of a driven-dissipative system out of equilibrium, where exploiting the atom loss rate as an observable, we discover different power-laws depending on the system parameters (i.e driving, dissipation and interaction). We study further in detail a regime which shows loss rates much larger than those for single particles, and discover that due to the Rydberg population decay the system evolves to a self-organized critical state. Our key observations can be well described by effectively classical models for the many-body dynamics, which we understand as a consequence of rapid dephasing of atomic coherences. To quantify the coherence of the atom-light interactions, we realize a Rydberg dressed interferometer. This technique combines the precision of atomic clock transitions with the exaggerated properties of Rydberg atoms such as their long-range interactions and extreme response to electric fields. Using the interferometer, we are able to characterize the Rydberg-dressed ensemble, including the effects of population decay and dephasing both of which affect the coherence time. This enables us to identify power fluctuations in the excitation laser as the dominant effects limiting the coherence in the system, which will be used in the experiment for future improvements of the coherence time. As an additional application, we demonstrate that the Rydberg dressed interferometer can be used to precisely measure static electric fields down to 17 mV/cm which is comparable to state-of-the-art electrometers. These results together highlight the versatility of the Rydberg platform and pave the way towards a better understanding of long-range interacting systems out-of-equilibrium. This work paves the way to new studies of non-equilibrium phenomena and applications of many-body quantum systems which make use of both quantum coherent and dissipative interactions.

Zusammenfassung

Diese Dissertation legt Untersuchungen an einem Rydberg-dressed ultrakalten Atomsystem als vielseitige Plattform für Forschungen zur Nichtgleichgewichtsphysik, zu Atom-Licht-Wechselwirkungen sowie zur atombasierten Metrologie dar. Die Arbeit umfasst die Beschreibung des experimentellen Aufbaus, welcher die Herstellung eines Gases von ultrakalten Kaliumatomen in einer Dipolfalle sowie die genaue Steuerung der Grundzustandseigenschaften erlaubt. Um die Atome zur stark wechselwirkenden Rydberg-Zuständen anzuregen, errichten und charakterisieren wir ein leistungsfähiges und weit einstellbares Lasersystem für die Ein- sowie Zwei-Photonen Rydberg-Anregung. Dies bildet zusammen ein einzigartiges System mit starkem Antrieb, langreichweitigen Wechselwirkungen und Dissipation aufgrund der begrenzten Lebensdauer der hochangeregten Atome. Mit diesem Aufbau erkunden wir die Phasenstruktur eines angetriebenen dissipativen Systems außerhalb des Gleichgewichts, wo die Atomverlustrate als Observable ausgenutzt wird, finden wir unterschiedliche Leistungsgesetze abhängig von den Systemparametern (d. h. Treiben, Dissipation und Interaktion). Wir untersuchen auch das langfristige dynamische Verhalten, wobei sich das System zu einem selbstorganisierten kritischen Zustand entwickelt. Die experimentellen Ergebnisse können als klassisches Vielkörperensemble beschrieben werden, da die Kohärenz bei den für die Messung relevanten Zeitskalen bereits verwaschen ist. Um die kohärente Entwicklung unseres Systems zu verbessern und zu verstehen, wie Kohärenz die Dynamik eines dissipativen Systems beeinflusst, erstellen wir ein Rydberg-dressed Interferometer. Diese Technik vereint die Präzision von Atomuhrübergängen mit den überhöhten Eigenschaften der Rydberg-Atome, wie beispielweise deren langreichweitigen Wechselwirkungen und hohe Empfindlichkeit für elektrische Felder. Mit dem Interferometer können wir das Rydberg-dressed Ensemble charakterisieren, insbesondere die Auswirkungen von Besetzungszerrfall und von Dephasierung, welche beide die Kohärenzzeit beeinflussen. Leistungsschwankungen des Anregungslasers stellen sich als größter Beitrag für die Dephasierung heraus und bilden gleichzeitig einen Ansatz für die zukünftige Verbesserung der experimentellen Kohärenzzeit. Zusätzlich demonstrieren wir die Anwendung des Rydberg-dressed Interferometers um statische elektrische Felder bis zu 17 mV/cm genau zu messen, was vergleichbar dem Stand der Technik von Elektrometern ist. Diese Ergebnisse verdeutlichen die Vielfältigkeit der Rydberg-Plattform und ebnet den Weg für ein besseres Verständnis von langreichweitig wechselwirkenden Systemen außerhalb des Gleichgewichts. Zudem legt diese Arbeit die Grundlage für zukünftige Untersuchungen, bei denen durch eine verbesserte Kohärenzzeit die Grenze zwischen isolierten und dissipativen Systemen erkundet werden kann, wobei Quanten- sowie klassische Fluktuationen konkurrieren.

Contents

1	Rydberg atoms: a versatile system for quantum simulations	1
2	The Rydberg platform: properties and models for the dynamics	7
2.1	Single atom Rydberg physics	8
2.1.1	Rydberg excitation of alkali atoms	8
2.1.2	Rydberg atom interaction with electric fields	9
2.1.3	Atom-light interaction for Rydberg excitation	10
2.2	Two-body Rydberg physics	13
2.2.1	Bare Rydberg interactions	13
2.2.2	Rydberg blockade and anti-blockade	15
2.2.3	Rydberg dressed interaction	16
2.2.4	Interactions: One vs two-photon excitation	17
2.3	Many-body physics using Rydberg atoms	21
2.3.1	The mean field treatment	21
2.3.2	Rate equation simulations: classical treatment	22
2.3.3	Towards a long-range interacting platform for non-equilibrium studies	23
3	Experimental platform for Rydberg dressed potassium	25
3.1	The ultracold atom system	26
3.1.1	The vacuum apparatus	27
3.1.2	Laser cooling and trapping of ^{39}K	28
3.1.3	Far detuned optical dipole trap	32
3.1.4	An adaptable program for experimental control and analysis	35
3.2	Atomic sample preparation	40
3.2.1	Magnetic field interaction with the ground state	40
3.2.2	Ground state control	42
3.2.3	Evaporative cooling	43
3.2.4	Spin polarization	45
3.2.5	Perspective for the ultracold atom platform	48
4	A versatile laser system for Rydberg excitation	49
4.1	A unique laser system for addressing ns, np and nd Rydberg states	50
4.1.1	Generation of the fundamental frequency light	51

4.1.2	Frequency doubling: Second harmonic generation	55
4.2	Characterization of the two-photon excitation system	57
4.2.1	Tunability and power	57
4.2.2	Linewidth and intensity noise	58
4.2.3	Long-term frequency stability characterization with ultracold ³⁹ K	61
4.2.4	Two-photon Rydberg spectroscopy	62
4.3	One-photon excitation system	65
4.3.1	Frequency lock approaches and noise measurements	65
4.3.2	Intensity noise	66
4.3.3	Laser and experimental setup characterization with the atomic sample	68
4.3.4	Perspectives for the Rydberg excitation system	70
5	Exploring non-equilibrium quantum matter with Rydberg atoms	71
5.1	Non-equilibrium phase structure	72
5.1.1	Model for a driven-dissipative Rydberg system	72
5.1.2	Loss rates measurements: key observable	74
5.1.3	Observation of scaling laws and phase diagram of the non- equilibrium system	76
5.2	Observation of self-organized criticality in a driven-dissipative Ryd- berg gas	79
5.2.1	Model for the dynamics	79
5.2.2	Signatures of SOC in the Rydberg ensemble	82
5.2.3	Towards studies of the role of quantum coherence in non- equilibrium systems	86
6	A Rydberg dressed interferometer	89
6.1	Theoretical model of a Rydberg-dressed interferometer	90
6.1.1	Ramsey interferometry	90
6.1.2	Rydberg dressed Ramsey signal	92
6.2	Ramsey interferometry of a Rydberg-dressed sample	95
6.2.1	Analysis of the Ramsey interferometry signals	95
6.3	Characterization of a Rydberg dressed ensemble	96
6.3.1	Atom-light coupling strength	97
6.3.2	Ramsey contrast: Dephasing and population decay	98
6.4	Realization of a sensitive Rydberg dressed electrometer	100
6.5	Perspectives for the Rydberg-dressed interferometer	102
7	Conclusion	105
	Appendices	111
A	An adaptable program for experimental control and analysis	113

A.1 Labview program modular structure	114
A.2 Modules: the principal devices and tasks in the experimental control program	118

Rydberg atoms: a versatile system for quantum simulations

Understanding how emergent macroscopic properties of many-body systems arise from their underlying microscopic details is one of the major challenges in physics, since the characteristics of the single components do not necessarily correspond to the collective behavior of the many-body system. For example, in certain materials at sufficiently low temperatures the interactions between the particles can give rise to collective quantum effects and new phenomena such as superfluidity [1, 2, 3] or superconductivity [4, 5, 6, 7], which still poses significant challenges to fully explain. Understanding how these effects come about would help to realize new materials with desirable properties and perhaps, discover totally new physical effects. However, the traditional approach based on building theoretical models to describe the relevant physics, including quantum effects, is severely limited by the complexity which scales exponentially with the number of particles and their degrees of freedom, making the computational approaches of quantum systems larger than a few tens of particles almost impossible.

A possible solution to this challenge is through quantum simulation [8, 9], where the system to be studied is mimicked in an experiment with components that can be controlled and measured more easily than the original. This can be done in a variety of systems ranging from ions [10, 11, 12], photons [13, 14, 15], ultracold atoms and molecules [16, 17] and superconducting circuits [18, 19, 20]. By understanding the system created in the lab new insights can be gained on the original many-body system under investigation, that is why quantum simulation holds great promise to study systems relevant for an ample spectrum of fields such as condensed matter physics, chemistry, high-energy physics and others [21].

Ultracold atoms are an ideal platform for quantum simulation. Success in this field is largely attributed to the development of techniques such as laser cooling and trapping [22] which have enabled an impressive level of control over essentially all ground state properties of ultracold atoms, including their atomic motion, spatial geometry, coherence, interaction properties and isolation from the environment. Moreover, by means of optical lattices or tweezers the atoms can be spatially confined to different geometries, including 1D, 2D and 3D geometries with different degrees of disorder [23]. In most cases, these trapped atomic systems base their dynamics on

relatively weak or short range interactions, e.g. Bose-Hubbard systems [24, 25, 26], Tonks-Girardeau gases [27, 28], BKT transition [29, 30, 31] and the unitary Fermi gas in the BCS-BEC crossover [32, 33, 34, 35, 36]. In real materials, the typical interactions are dominated by Coulomb interactions, where the main carriers of the dynamics are the electrons, which determine the consequent properties of the material. Therefore it is natural for quantum simulation to want to mimic the effect of long-range interactions, such that the simulation resembles more closely actual materials.

Our approach is to use Rydberg atoms to introduce such long-range interactions. Given their highly excited electronic states, Rydberg atoms exhibit strong van der Waals interactions, that can extend over typical inter-atomic distances. As a consequence, interesting collective effects can occur such as the Rydberg blockade [37, 38, 39, 40] which have been used to simulate magnetic phenomena [41, 42, 43, 44], to create fast and addressable entangled states for quantum information [45, 46, 47], and to realize new phases of matter [48, 49, 50, 51, 52, 53, 54, 55]. The main properties from the Rydberg atoms which are exploited in this thesis are:

- Long range interaction with tunable strength either via the principal quantum number or laser detuned excitation (Rydberg dressing). The interactions can be turned on and off at will via the excitation laser.
- Finite lifetime that introduces a dissipative character to the system such that it constrains the study of dipolar interactions with motional dynamics, but can also be employed to investigate the physics of open-quantum systems
- Sensitivity to external electric fields due to their high polarizability can be used for technological applications as an electrometer

In parallel other atomic and molecular platforms are used to simulate long-range interacting systems. The first alternative is to utilize magnetic atomic species (instead of the more typical alkali atoms) such as chromium, dysprosium and erbium [56, 57, 58], which feature magnetic dipole-dipole interactions. A second approach is to use ground state polar molecules interacting via dipolar interactions [59, 60, 61, 62], where the interaction between molecules has been observed through the collective dephasing dynamics of the ensemble [63]. One of the main advantages of Rydberg atoms over other approaches is the ability to tune the sign and strength of the interactions and also turn it off completely, which gives the system more flexibility compared to other long-range interacting particles.

A potential drawback of the Rydberg platform is the relatively short lifetime of

the excited atoms making the study of the system's dynamical evolution on long timescales challenging. To solve this issue Rydberg dressing as an off-resonant Rydberg excitation has been proposed [64, 37]. The idea is to create a ground state that acquires a small admixture of the Rydberg state, enhancing the long-range interaction while having a much longer lifetime than the bare Rydberg state. However, the systems complexity, reinforced by the interplay of interactions, driving and decay, have proven to be challenging in the creation of Rydberg-dressed systems [65]. Only a few experiments in the past years have been able to demonstrate the generation of Rydberg-dressed systems [53, 54, 55]. One can also embrace dissipation, and a number of recent studies have shown how the competition between continuous driving, long range interactions and spontaneous decay of the Rydberg states leads to the realization of new intrinsically non-equilibrium states of matter [66, 67, 68, 69, 70, 71, 72, 73, 74]. In this thesis we make use of this dissipative characteristic to carry out fundamental studies on non-equilibrium physics in a driven-dissipative system. Additionally, we use Rydberg dressing to create an enhanced interferometer, which allows us to characterize the coherence properties of the Rydberg dressed system and as a spin-off we realize an application of the interferometer for atomic sensing of electric fields.

As a first result in this thesis, we take advantage of the finite lifetime of Rydberg atoms to study the phase structure associated with its dissipative behavior and to investigate its non linear dynamical evolution. In this work we investigate the competition between driving, dissipation and strong interaction using the high tunability offered by our setup. We find out that the atom loss rate is an ideal observable for exploring the phase structure of a system driven out-of-equilibrium, and that power law scaling in different parameter regimes can be used to determine the regions of the phase structure. In a specific regime where facilitated excitation [75] increases the loss rate scaling, we investigate the long term dynamical response of the system. We observe a self-organized behavior to a quasi steady state which presents scale invariance and a strong response to perturbations. From this we conclude that our Rydberg platform can be used as a simulator for quantitative studies of self-organized criticality (SOC [76]). Furthermore, the theoretical models used to reproduce our results are classical approximations of the quantum master equation that describes our system. This can be justified since the time scales explored in the experiments are much longer compared to the coherence times. It is, however, an open question whether quantum effects would play a role in the non-equilibrium dynamics [77, 78], therefore it is desirable to have a coherent system where classical and quantum fluctuations can compete.

In the second part of this work we investigate how to characterize the coherence properties of our system, with the aim of finding the precise controls to increase the coherence times. As a main result, we present a technique based on interferometry,

where we Rydberg-dress one of the states involved in the interferometry and analyze the signal. The results help us to uncover the main properties of the Rydberg-dressed ensemble including the coupling strength to the Rydberg state and the coherence behavior in terms of population decay and pure dephasing. This method proves to be a precise way to characterize and optimize Rydberg-dressed systems [65, 53, 79, 80], and it could be also use to control and characterize atomic interactions in general [81, 82, 83, 84, 85, 80]. Based on this characterization we are able to identify the factor influencing the system decoherence the most, namely power fluctuations in the laser. This can be improved in future experiments, which should get our system closer to the regime where quantum coherence cannot be neglected, allowing us to study the competition between classical statistical fluctuations and quantum effects in a system driven out of equilibrium.

In general, the extremely precise creation and manipulation of quantum systems has enabled a variety of studies such as atom-light interactions [86], cavity quantum electrodynamics [87, 88] and strongly correlated matter [89, 90], to mention only a few. Usually fundamental research leads to a deeper understanding of mechanisms that enable the implementation of new technologies. For example with the accurate control and read out of different electronic states, atomic clocks based on trapped ensembles of neutral atoms or single ions have been built to enable the most precise measurements ever made [91]. Atomic clocks are employed for different applications such as defining future time and frequency standards [92, 93], investigating the physics of complex quantum systems [81], and realizing sensors capable of operating at the fundamental quantum limit [94, 95]. By design however, atomic clocks typically involve the coherent evolution of atoms that interact very weakly, either with one another or with external fields, seemingly precluding applications that could exploit dissipation or strong interactions. Similarly, Rydberg atoms have also encountered a variety of technological applications such as probing surface fields [96, 97, 98, 99], sensing using thermal vapours [100, 101] and quantum enhanced metrology [102, 103]. In this thesis we realize a metrological application where we take advantage of the precise control of ground state atoms and combine it with Rydberg atoms via dressing. In this sense we use the opposite approach of an atomic clock: we allow the system, via the Rydberg admixture, to strongly couple to the environment, enhancing the ensemble's sensitivity to interactions between the atoms or with external fields. This results in a system that combines the high precision of an atomic clock and the multiple properties of a Rydberg atom. Using this new platform we can perform precise measurements of static electric fields, with a sensitivity comparable to the most modern electrometers.

The outline of this thesis is as following: First a chapter regarding the theory background of Rydberg atoms and the latest studies on many-body systems are presented in chapter 2, this includes the main properties and interaction characteristics of a

Rydberg system. Chapter 3 introduces the experimental platform for ultracold potassium as the building block for the realization of a Rydberg enhanced system. This includes a description of the up-to-date experimental setup and the techniques used to prepare the atomic sample before exciting the ground state atoms to a Rydberg state. As a second experimental milestone, we present in chapter 4 a versatile laser system that can be used for both Rydberg excitation schemes, i.e. two-photon and single photon excitation. We show a detailed explanation and characterization of the laser setup and, as a proof of principle, we present the first Rydberg experiments for both schemes which are used to further characterize the experimental setup. The next part (chapter 5) focuses on a first application of our Rydberg platform to study non-equilibrium dynamics, there we explore the competition between coherent driving, decay and long-range interactions. We show that the different regimes can be differentiated in terms of scaling laws in the loss rate, uncovering the non-equilibrium phase structure of the system. We also study the dynamical response of the ensemble where dissipation and interaction compete and discover a striking self-organized critical behavior. In the final chapter (6) we explore the coherent response of a Rydberg dressed system combining the ground state control of an atomic clock transition and the detuned Rydberg excitation of one of the clock states. This Rydberg-dressed atom interferometer proves to be very useful to characterize the dressed system, especially regarding the dephasing and its possible causes. We show that the regime of strong Rydberg atom-light coupling can be reached with coherence times that are orders of magnitude longer than the bare Rydberg state lifetime. Moreover, we demonstrate a direct application of the Rydberg-dressed interferometer as a very sensitive electrometer exploiting the high polarizability of the Rydberg atoms to detect weak static electric fields, with a measured sensitivity already close to the state-of-the-art electrometers. Finally, chapter 7 discusses how these results pave the way for experiments that aim to explore many-body physics problems with long-range interactions and possible future technological applications in metrology.

The Rydberg platform: properties and models for the dynamics

Ultracold atom experiments have proven to be able to extremely precisely control the interactions and ground state properties of the involved atoms, ranging from Bose-Einstein condensation experiments [104, 105, 106] to studies with degenerate Fermi gases [107, 108, 109, 32, 33, 34, 35, 36]. Those interactions are typically of the contact type, where the particles need to come very close together to experience an effective interaction. However, as most particle interactions in matter are of long-range type, such as in strongly correlated electron matter [110] or nematic liquid crystals [111], it is important to be able to model/control these effects as well. Along these lines different types of particles have been used with some groundbreaking work in such diverse systems as, in polar molecules [112, 59, 113], highly magnetic atomic species [114, 115, 58, 116] and ions [10, 117, 118], for example. Rydberg atoms (highly excited electronic states) are another type of particle that can be used as a platform for studying long-range interacting systems [119, 120, 121] as is developed in this chapter within the theoretical framework of Rydberg physics.

This chapter comprises a review on the relevant characteristics of Rydberg atoms, including the main effects that are observed or exploited in our experiment. In the first part all the relevant characteristics of single Rydberg atoms are introduced, including the extreme scaling behavior of some properties. In the next part we concentrate on the interactions of Rydberg atoms with external environments such as electric fields and laser fields, describing the most common excitation schemes to Rydberg states and how to model it. The next section covers the two-body physics of this system, it focuses on Rydberg-Rydberg interactions which give rise to effects such as the Rydberg blockade. Using all these previous concepts, we calculate the Rydberg dressed interaction in a three-level system finding a favorable figure of merit with reduced scattering rates. In the last section of this chapter we summarize the most used techniques in this thesis to simulate many-body Rydberg dynamics. Part of the content of this chapter on the two-body Rydberg physics is based in the paper on "Two-body interactions and decay of three-level Rydberg dressed atoms" [122]. Additionally the many-body Rydberg physics describes the models we used to simulate the results presented in chapter 5 based on the paper "Uncovering the nonequilibrium phase structure of an open quantum spin system" [74].

2.1 Single atom Rydberg physics

Rydberg atoms are excited electronic states of atoms, with one or more electrons that have a high principal quantum number n . In the most simple case, the atom has only one electron (as in hydrogen) which can be excited to the n -state, resulting in an electron with binding energy [119]:

$$E_n = -\frac{R_y}{n^2}, \quad (2.1)$$

where R_y is the Rydberg constant and has the value:

$$\frac{Z^2 e^4 m_e}{16\pi^2 \epsilon_0 \hbar^2}. \quad (2.2)$$

The electronic configuration of these Rydberg atoms gives rise to enhanced properties that scale with the principal quantum number n , as for the binding energy (equation 2.1). Table 2.1 presents the main properties of Rydberg atoms with the corresponding scaling. We can see for example how the polarizability scales with a power law of n^7 , making the Rydberg atom very sensitive to electric fields. This is a result of the large dipole matrix elements coupling neighbor Rydberg states, which also gives rise to a strong long-range interaction of the dipole-dipole or van der Waals (vdw) type.

Property	Symbol	Scaling
Binding energy	E_n	n^{-2}
E difference between adjacent states	ΔE	n^{-3}
Radiative lifetime	τ_{rad}	n^3
Polarizability	α	n^7
Vdw interaction coefficient	C_6	n^{11}

Tab. 2.1.: Most relevant properties of Rydberg atoms and their corresponding scaling. This table shows the dependence of different properties as a power-law of the principal quantum number n .

2.1.1 Rydberg excitation of alkali atoms

Alkali metal atoms are those characterized by having only one valence electron (placed in the first column of the periodic table) similar to the hydrogen atom. The main difference with respect to hydrogen is the nuclear charge and the surrounding electrons fully occupying the lower energy shells. The presence of this electron cloud close to the nucleus partially screens the nuclear charge. Additionally, for low orbital angular momentum ($l \leq 3$) of the valence electron, the trajectory of this electron is elliptical enough that there is a finite probability for it to go through the screening electrons. This effect allows the valence electron to interact with the unscreened nucleus, modifying the coulomb potential. In addition the screening electrons can

be polarized by the valence electron creating an extra interaction that cannot be neglected.

The above mentioned interactions cause the binding energy of the Rydberg states to increase compared to the equivalent hydrogen state. Based on this, the binding energy for the alkali Rydberg atoms is defined as:

$$E_n = \frac{-R_y}{(n - \delta_{n,l,j})^2}, \quad (2.3)$$

where $\delta_{n,l,j}$ is the parameter known as the quantum defect, which depends on the quantum numbers n (principal quantum number), l (orbital angular momentum), j (spin and orbital angular momenta of the electron) of the specific Rydberg state. For Rydberg states with $l \geq 4$ the spectrum becomes hydrogenic and the quantum defect can be neglected. The precise value of the quantum defect is determined empirically via spectroscopy measurements, which in the case of potassium, the atom species used in the experiments of this thesis, can be found in [123]. The full value of the quantum defect is given by the series:

$$\delta_{n,l,j} = \delta_0 + \frac{\delta_2}{(n - \delta_0)^2} + \frac{\delta_4}{(n - \delta_0)^4} + \dots \quad (2.4)$$

All the Rydberg scaling properties presented for the hydrogen atom in table 2.1 are also valid for alkali Rydberg atoms, however the n quantum number needs to be modified by $n^* = n - \delta_{n,l,j}$.

2.1.2 Rydberg atom interaction with electric fields

The presence of an electric field in the proximity of an atom causes the energy levels of the atom to split and shift, this phenomenon is known as the Stark effect [124, 125]. Rydberg atoms due to the highly excited electron (i.e. dipole like charge distribution) are more sensitive to electric fields than ground state neutral atoms. Therefore it is important to understand this effect in order to either reduce the influence of the field or exploit it for different experimental purposes as we will see in later chapters (see 4 and 6). For the scope of this thesis, we concentrate only on the effect of a small constant electric field on a Rydberg atom, other effects can be found for example in [119].

Assuming that the constant electric field (ϵ) is in the z direction, the energy states of the atom can be calculated via perturbation theory, where the bare atom Hamiltonian is modified by the perturbation:

$$H_\epsilon = \hat{d} \cdot \hat{\epsilon} = e\epsilon z \quad (2.5)$$

The first order correction term $\Delta E = e\epsilon\langle\psi_{n,l,m}|z|\psi_{n,l,m}\rangle$ is zero for the states with $l \leq 3$ since the core potential lifts the l degeneracy. Therefore the first energy shift contribution is given by:

$$\Delta E_\epsilon = -\epsilon^2 \sum_{n'l'm'/nlm} \frac{|\langle\psi_{n,l,m}|z|\psi_{n',l',m'}\rangle|^2}{E_{n'} - E_n} \quad (2.6)$$

The energy shift of the state due to a small electric field can be rewritten as $\Delta E_\epsilon = -\frac{1}{2}\alpha\epsilon^2$, with α the polarizability of the atom. In the case of a Rydberg atom, one can immediately infer the scaling of the polarizability since the energy difference between adjacent levels scale as n^{-3} (see table 2.1) and the dipole moment scales with the electron orbit radius as n^2 then $|\langle\psi_{n,l,m}|z|\psi_{n',l',m'}\rangle|^2 \propto n^4$. This results in the scaling of the polarizability as n^7 , which clearly shows the sensitivity of Rydberg atoms to electric fields, specially for large n states. Compared to the polarizability of a ground state atom, Rydberg atoms are suited for applications in electrometry [126] as it is shown in chapter 6.

2.1.3 Atom-light interaction for Rydberg excitation

To precisely excite a valence electron of the atom to a high n quantum number, a laser field is typically required. In experiments with ultracold atoms this excitation is carried often via a single laser field or two different fields where one of the lasers address an intermediate excited state. Figure 2.1 shows these two possibilities with $|g\rangle, |e\rangle, |r\rangle$ representing the ground, intermediate and Rydberg state respectively.

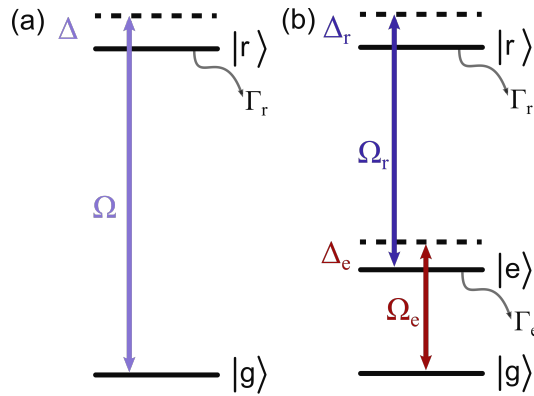


Fig. 2.1.: Schematic representation of the one- and two-photon excitation process. (a) Rydberg excitation via a single laser field, with driving frequency Ω and detuning Δ . Since only two levels are involved the decay of population depends mainly on the Rydberg lifetime Γ_r . (b) Rydberg excitation via an intermediate state ($|e\rangle$) in a three-level system. The laser driving the excitation to $|e\rangle$ is typically detuned to avoid strong decay from the state $|e\rangle$.

The simplest scenario is a single photon excitation (2.1) which can be understood as

a two-level system interacting with a classical electromagnetic field (the laser). The Hamiltonian that describes this interaction is:

$$H_{one} = \frac{\Omega}{2}|g\rangle\langle r| - \frac{\Delta}{2}|r\rangle\langle r| + h.c. \quad (2.7)$$

with Δ the frequency difference between the laser and the atomic transition, and $\Omega = \frac{eE_0\langle g|\hat{r}|r\rangle}{\hbar}$ the atom-light coupling between $|g\rangle$ and $|r\rangle$, also known as the Rabi frequency. Since the dipole matrix element in Ω is small for high-lying Rydberg atoms, we would require in the actual experiments high laser power to compensate this (see chapter 4). The Hamiltonian is already presented in the rotating wave approximation [127], where the fast evolving terms are averaged out and therefore neglected. The master equation that describes the dynamics is $\dot{\hat{\rho}} = -\frac{i}{\hbar} [\hat{H}, \hat{\rho}]$, where $\hat{\rho}$ is the density matrix operator that contains the probability distribution of each state of the basis on the diagonal, and the coherences between different states on the off-diagonal.

In addition to the coupling field, one needs to take into account the dissipation in the system for example due to the finite lifetime of the Rydberg state, which can lead to decay of population and also dephasing. Therefore the time evolution of the atomic system (represented by the density matrix operator $\hat{\rho}$) needs to be described by the Liouville equation [128]:

$$\dot{\hat{\rho}} = -\frac{i}{\hbar} [\hat{H}, \hat{\rho}] + \mathcal{L}[\rho], \quad (2.8)$$

with $\mathcal{L}[\rho]$ the Lindblad superoperator [129] describes all of the dissipative non-unitary processes present in the system. \hat{L} is used to model the decay and dephasing from Rydberg or other rapidly decaying states and given by:

$$\mathcal{L}[\rho] = -\frac{1}{2} \sum_m \left[\hat{L}_m^\dagger \hat{L}_m \hat{\rho} + \hat{\rho} \hat{L}_m^\dagger \hat{L}_m - 2\hat{L}_m \hat{\rho} \hat{L}_m^\dagger \right], \quad (2.9)$$

where \hat{L}_m is the Lindblad operator describing the m th decay of the system. In the two-level scheme we will use: $\hat{L}_{rg} = \sqrt{\Gamma_r}|g\rangle\langle r|$ which corresponds to the decay from the Rydberg state to the ground state with rate Γ_r . The resulting time evolution of the population in one of the two states oscillates in time with frequency $\Omega' = \sqrt{\Omega_r^2 + \Delta_r^2}$ with damping on the time scale of Γ_r . Additionally dephasing due to laser noise also contributes to the dissipative non-unitary process which we usually model as $\hat{L}_{de} = \sqrt{\gamma_{de}}|r\rangle\langle r|$, with γ_{de} the laser noise which affects the excitation to the Rydberg states. In actual experiments is then important to reduce such dephasing terms by properly stabilizing the excitation laser system, as it will be shown in chapter 4.

The three-level system can be similarly studied by the time evolution of the density

matrix in equation 2.8, with the Hamiltonian:

$$H_{two} = \frac{\Omega_e}{2}|g\rangle\langle e| - \frac{\Delta_e}{2}|e\rangle\langle e| + \frac{\Omega_r}{2}|e\rangle\langle r| - \frac{\Delta_r}{2}|r\rangle\langle r| + h.c. \quad (2.10)$$

which includes the couplings Ω_e and Ω_r between the ground and the excited state and the excited state with the Rydberg state respectively. The detunings for each laser field correspond to Δ_e and Δ_r , as depicted in fig. 2.1. The Lindblad operators represent the decay from the Rydberg state ($\hat{L}_{re} = \sqrt{\Gamma_r}|e\rangle\langle r|$) and from the intermediate state ($\hat{L}_{eg} = \sqrt{\Gamma_e}|g\rangle\langle e|$). The superoperator $\mathcal{L}[\rho]$ in the matrix form is:

$$\mathcal{L}[\rho] = \begin{pmatrix} \Gamma_e \rho_{ee} & -\frac{1}{2}\Gamma_e \rho_{ge} & -\frac{1}{2}\Gamma_r \rho_{gr} \\ -\frac{1}{2}\Gamma_e \rho_{eg} & -\Gamma_e \rho_{ee} + \Gamma_r \rho_{rr} & -\frac{1}{2}(\Gamma_e + \Gamma_r) \rho_{er} \\ -\frac{1}{2}\Gamma_r \rho_{rg} & -\frac{1}{2}(\Gamma_e + \Gamma_r) \rho_{re} & -\Gamma_r \rho_{rr} \end{pmatrix} \quad (2.11)$$

where the ρ_{ij} correspond to the ij time-dependent matrix element of the density matrix $\hat{\rho}$.

Electromagnetic induced transparency (EIT).

Electromagnetic induced transparency is an interference phenomenon in a three-level system (like the one in figure 2.10 (a) for a two-photon excitation scheme) where two pair of states are coupled via two different laser fields: one weak compared to the second one, i.e. $\Omega_e \ll \Omega_r$. The emergent non-linearity through a strong coupling field gives rise to the transparency of the medium (the atoms) which otherwise are strongly absorbing [130]. This phenomenon has been exploited in different applications as to realize strong electro-optic effects in vapor cells [131] or to slow down light [132, 133, 134, 135].

To understand how the medium can become transparent to a laser field close to resonance, we start by diagonalizing the three-level Hamiltonian presented in equation 2.10 and extract the eigenstates in the case of two-photon resonance, i.e. $\Delta_e + \Delta_r = 0$. Which results in [130]:

$$|+\rangle = \sin \theta \sin \phi |g\rangle + \cos \phi |e\rangle + \cos \theta \sin \phi |r\rangle \quad (2.12)$$

$$|-\rangle = \sin \theta \cos \phi |g\rangle - \sin \phi |e\rangle + \cos \theta \cos \phi |r\rangle \quad (2.13)$$

$$|d\rangle = \cos \theta |g\rangle - \sin \theta |r\rangle \quad (2.14)$$

with θ and ϕ the angles defined as: $\tan \theta = \frac{\Omega_e}{\Omega_r}$ and $\tan 2\phi = \frac{\sqrt{\Omega_e^2 + \Omega_r^2}}{\Delta_e}$. The transparency phenomenon occurs in the weak limit with $\Omega_e \ll \Omega_r, \Gamma_e$, making the angle θ very small, such that $|d\rangle = |g\rangle$ becomes a dark state to the laser field and $|+\rangle, |-\rangle$ interfere destructively with each other.

2.2 Two-body Rydberg physics

As presented in the introduction to this chapter the long-range interaction is one of the most important properties of Rydberg states that can be exploited for quantum simulation, quantum information, and the creation of new states of matter [121, 120, 49]. This section focuses on the interaction between two atoms in the bare Rydberg state or dressed ground states such that they have Rydberg-like properties. The first part presents the theory on bare Rydberg-Rydberg interactions and the most relevant features, while the second part introduces the concept of Rydberg dressing. We compare two excitation techniques (one- and two-photon), finding different advantages regarding the interaction strength vs the dissipation.

2.2.1 Bare Rydberg interactions

In a classical picture, the two Rydberg atoms can be seen as charge distributions with a negative part (the valence electron) and a positive part (the screened nucleus). In the case the separation between the two atoms is larger than its own size, the interaction is dominated by the electrostatic interaction of the valence electrons, which can be expanded in multipole moments [136, 137]. In the case of neutral atoms, the first and main term contributing from the expansion is the dipole-dipole interaction, (since the whole atom is neutral, i.e. has no monopole contribution). In the quantum mechanical picture a similar treatment can be performed, where the position vectors become position operators, the dipole-dipole coupling can be described by the interaction potential:

$$\hat{V} \approx \frac{1}{4\pi\epsilon_0 R^3} \left(\hat{d}_1 \cdot \hat{d}_2 - 3 \left(\hat{d}_1 \cdot \hat{r} \right) \left(\hat{d}_2 \cdot \hat{r} \right) \right), \quad (2.15)$$

with \hat{r} the position operator normalized by the inter-atomic distance (R) and \hat{d}_i the electric transition dipole operator. Describing each atom by the two principal quantum numbers n, l and assuming that only two adjacent states are close in energy compared to all other states, we can reduce the system to a two-level. For example taking $|ns, ns\rangle$ as the initial atomic state and the adjacent pair state closest in energy $|np, (n-1)p\rangle$. The eigen-energies of the system are:

$$\Delta E_{\pm} = \frac{\delta_{nl}}{2} \pm \frac{1}{2} \sqrt{\delta_{nl}^2 + \left(\frac{C_3}{R^3} \right)^2} \quad (2.16)$$

with $C_3 = R^3 \langle ns, ns | \hat{V} | np, (n-1)p \rangle$ the interaction coefficient and $\delta_{nl} = 2E_{ns} - E_{np} - E_{(n-1)p}$ the energy difference between the pair states. The interaction shows two limits depending on the separation between the atoms. In the case the atoms are very close ($C_3/R^3 \gg \delta_{nl}$), the states $|ns, ns\rangle$ and $|np, (n-1)p\rangle$ are strongly admixed

and the eigenenergies are $\Delta E \approx \pm C_3/R^3$. On the other hand, if $C_3/R^3 \ll \delta_{nl}$ the states are hardly admixed and the energy of the $|ns, ns\rangle$ can be approximated as

$$\Delta E \approx \frac{1}{2\delta} \left(\frac{C_3}{R^3} \right)^2 \quad (2.17)$$

which is known as the van der Waals interaction, with $C_6 = C_3^2$ the interaction coefficient. In this limit, the effect of the interaction is a shift in the energy of the pair state $|ns, ns\rangle$.

It is possible to tune the interactions from one regime to another by adjusting δ , assuming that it is already small enough, one can use a small DC field to shift the pair state difference such that δ becomes zero. This is known as a Förster resonance [138], which has been capitalized on with Rydberg atoms such as in the creation of a single-photon transistor [139] and also proposed as a way to engineer distance dependent interactions [41].

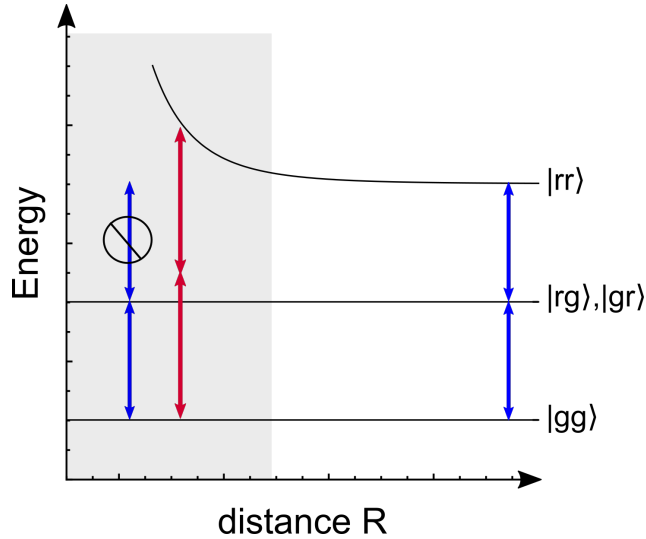


Fig. 2.2.: Schematic representation of the blockade and antiblockade Rydberg effects. In the case the laser is resonant with the Rydberg transition (blue), a second Rydberg excitation is hindered for a separation smaller than the blockade radius R_B . When the laser is detuned (red arrow), there is a preferred distance to excite a second Rydberg atom.

In our experiments the inter-atomic distance maintains the system in the van der Waals regime such that the effective Rydberg-Rydberg interaction behaves as $1/R^6$. Due to this power law decay of the interaction with respect to the interparticle distance, the interactions are long-range such that an excitation can affect the state of the surrounding atoms beyond the nearest neighbors, as we will see in the next section.

2.2.2 Rydberg blockade and anti-blockade

Considering a set of two atoms (as in figure 2.2) that can be excited and interact depending on the separation R as $\propto 1/R^6$. In the simple two-level case the pair of atoms can be described via the four-states basis $\{|gg\rangle, |gr\rangle, |rg\rangle, |rr\rangle\}$. Figure 2.2 shows the energy dependence for each pair state as a function of the inter-atomic distance R , assuming that the interaction is van der Waals, which is always the case in our experiments. Since only two Rydberg atoms can strongly interact (i.e. Rydberg-ground and ground-ground interactions are neglected), the energy landscape is only affected for $|rr\rangle$.

Considering the case where the laser field that drives the transition is on resonance with the excitation of a single atom, there is a region in R (shaded in fig. 2.2) where the laser is no longer resonant for a second excitation due to the energy shift from the van der Waals interaction. This effect is known as the Rydberg blockade, proposed first by [37, 38] and observed in [39, 40], since the presence of an excited atom blocks the excitation of the surrounding atoms within a radius R_B .

The blockade occurs for the atoms within a sphere or radius R_B that is determined by the bandwidth of the excitation laser, which for small dephasing is dominated by the power broadening such that:

$$\hbar\Omega = \frac{C_6}{R_B^6} \Rightarrow R_B = \left(\frac{\hbar\Omega}{C_6} \right)^{1/6} \quad (2.18)$$

where in the case the laser linewidth $\Delta\nu$ is larger than the Rabi frequency one should change Ω for $\Delta\nu$ to determine the blockade radius. It is important to understand that the concept of blockade does not correspond to a hard sphere condition since there is always some probability to excite Rydberg atoms off-resonantly. Extending the idea of Rydberg blockade to an ensemble of N atoms within the R_B radius the system will oscillate between a state with all atoms in the ground state and a superposition of all states with only one Rydberg excitation i.e. $\frac{1}{\sqrt{N}} \sum_{j=1}^N |ggg..r_j..g\rangle$. The frequency of the oscillation is enhanced by $\sqrt{N}\Omega$ which emphasizes the many-body nature of the system.

A related effect to the blockade occurs when the laser is detuned from resonance, the presence of a Rydberg atom can help to excite another one in the vicinity such that the interaction energy shift is compensated by the detuning. This facilitated excitation is known as the antiblockade [75] (observed for the first time by [46]) and have been investigated theoretically and experimentally for instance in the dynamical formation of Rydberg aggregates [70, 140, 72], to study kinetic constraints [73, 141] and Rydberg excitation avalanches [142].

2.2.3 Rydberg dressed interaction

The strong long-range interaction between two Rydberg states is a remarkable property of Rydberg atoms, that make this platform favorable for a variety of applications such quantum information [45, 46, 47], quantum simulation of magnetic phenomena [41, 42, 43, 44], and to realize new types of quantum matter [48, 49, 50, 51, 52, 53, 54, 55]. However up to here we have only considered the interactions without including the inherent dissipation of the Rydberg state due to its finite lifetime. The typical time scales for the Rydberg decay (tens of microseconds) are not compatible with the usual time the system requires to equilibrate (tens of milliseconds). Rydberg dressing has been proposed [64, 37] as an approach to overcome this challenge, where the most common way to increase the lifetime of the Rydberg system is via a detuned excitation. This creates a dressed state that corresponds mostly to the ground state with a small Rydberg admixture [143] resulting in a still long-range interacting system but with longer lifetimes.

We consider the far-detuned regime where $\Delta \gg \Omega$ for the two-level case (figure 2.1b). The system can be described as a superposition of the ground and the Rydberg states: $|\tilde{g}\rangle \sim |g\rangle + \beta|R\rangle$ with $\beta = \frac{\Omega}{2|\Delta|} \ll 1$, where β^2 describes the probability of finding the atom in the Rydberg state $|r\rangle$. Therefore the Rydberg admixture can be controlled by adjusting the detuning and Rabi coupling. The admixture leads to an effective lifetime of the dressed state: $\tau_{eff} = \tau/\beta^2$ which is increased by a factor of β^{-2} . The interaction potential will depend on the sign of the detuning in the two-level case (explored in detail in section 2.2.4), where in the case the detuning can compensate the interaction energy (i.e. $\Delta = V(R)$, facilitation condition), an avoiding crossing occurs at the facilitation distance which mixes the ground and Rydberg state strongly (see fig. 2.3b). On the other hand, if the detuning has the opposite sign to compensate the interaction, an effective soft-core potential is created [143] such that the interaction flattens, this comes from the Rydberg blockade effect. As a result the dressed potential, outside the characteristic distance of the soft-core potential ($\sim R_B$), can be approximated via perturbation theory as an energy shift $V_{dress}(r) \approx \beta^4 V(r)$. These characteristics together can be exploited to create Rydberg enhanced atoms that can evolve coherently within the motional dynamics time scale of the system while still interacting at long range.

Within the framework of quantum simulation with long-range interacting particles and quantum information, this particular approach has been extensively explored theoretically for different purposes such as engineering exotic states of matter [48, 49, 50, 51, 144, 42, 145] or as a platform for quantum computation [146] and quantum annealing [147]. However, experimentally the success is not as evident due to the system's complexity, it is a challenge to create Rydberg-dressed systems [65],

where anomalous interaction broadening has been observed [148, 149]. Only few experiments in the past years have been able to demonstrate the generation of Rydberg-dressed systems [53, 54, 55], making it still an ongoing project how to characterize and manipulate such systems. In chapter 6 we demonstrate a Rydberg-dressed interferometer that can be used for such characterizations. In the next section the approach of Rydberg dressing will be further explored, concentrating on the interaction between two-dressed atoms, and comparing one and two-photon excitation approaches.

2.2.4 Interactions: One vs two-photon excitation

Given the promising characteristics of Rydberg-dressed atoms for studying dipolar interactions with motional dynamics, we want to investigate in more detail the advantages of the two different excitation schemes and, in particular, compare them. For this we consider only the interaction between two Rydberg dressed atoms for each excitation scenario. We aim to calculate and compare the effective interaction potential with the photon scattering rate (directly related to the Rydberg-dressed system decay). We use a quantum master equation treatment which includes spontaneous decay from the excited states, as in eq. 2.8, using a Hamiltonian that consists of three parts $\hat{H} = \hat{H}_1 + \hat{H}_2 + \hat{V}$, where $\hat{H}_{1,2}$ are the individual atom-light Hamiltonians in the rotating wave approximation and $\hat{V} = V|r_1\rangle|r_2\rangle\langle r_1|\langle r_2|$ is the two-body interaction between bare Rydberg states. Focusing on the three-level system (Fig 2.1a), in which each atom is composed of a long lived ground state $|g\rangle$ coupled to the Rydberg state $|r\rangle$ via a short lived intermediate state $|e\rangle$, the Hamiltonian for one of the particles (as in eq.2.10) is:

$$\begin{aligned} \hat{H}_j = & \frac{\Omega_e}{2}|g_j\rangle\langle e_j| + \frac{\Omega_r}{2}|e_j\rangle\langle r_j| \\ & - \frac{\Delta_e}{2}|e_j\rangle\langle e_j| - \frac{\Delta}{2}|r_j\rangle\langle r_j| + \text{H.c.} \end{aligned} \quad (2.19)$$

Here $\Omega_{e,r}$ denote the Rabi frequencies of the respective laser fields and Δ_e , $\Delta = \Delta_e + \Delta_r$ refer to the one photon and two photon detunings, respectively. Additionally, we include the spontaneous decay of the excited states via the superoperator \mathcal{L} (see eq.2.9), which includes two decay operators: $\sqrt{\Gamma_e}|g_j\rangle\langle e_j|$ and $\sqrt{\Gamma_r}|e_j\rangle\langle r_j|$, $\Gamma_{e/r}$ the spontaneous decay rate of the particle j from $|e\rangle$ and $|r\rangle$. While the two-level case has relatively few tuning parameters (Ω and Δ), the three-level case presents additional possibilities through independent tuning of Ω_e , Ω_r , Δ_e and Δ .

For these calculations we assume that couplings to other Rydberg states are negligible and the interactions between atoms in the $|g\rangle$ or $|e\rangle$ states are much weaker. Usually $\Gamma_e \gg \Gamma_r$ such that the internal degrees of freedom reach the steady state on a timescale $\sim \Gamma_e^{-1}$ which is typically much faster than motional timescales. Un-

der these assumptions, it is sufficient to calculate the steady state values of the dressed potential and residual scattering rate for each value of V without explicitly considering the motion of the particles. However care must be taken applying the same reasoning to atoms with metastable intermediate states for which equilibrium is reached on longer time scales or to the two-level case where Γ_r^{-1} would be the timescale reference and could be of the same order of the atomic motion.

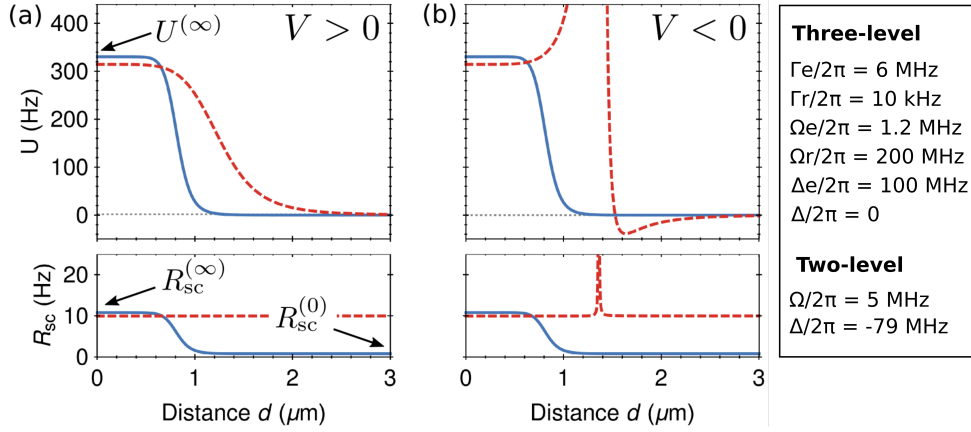


Fig. 2.3.: Simulation on the two-body interaction and scattering rate for one and two-photon excitation. Comparison of the interaction strength $U(C_6/d^6)$ and scattering rate $R_{sc}(C_6/d^6)$ for two-level (dashed red lines) and three-level systems (solid blue lines) assuming repulsive van der Waals interactions between Rydberg states and $\Delta = 0, \Delta_e > 0$ (three-level) and $\Delta < 0$ (two-level). (b) Same as in (a) but for attractive van der Waals interactions. The parameters used for the calculations are given in the text. Figure adapted from [122].

One vs two-photon: interaction potential and scattering rate.

Having the basis to simulate the Hamiltonians for the one and two-photon scheme, we proceed to investigate the influence of an intermediate state on the shape and strength of the dressed interactions. We calculate the interaction potential $U(V)$ by solving the master equation for steady state ($\dot{\rho} = 0$) followed by computing the expectation value $U(V) = \text{Tr}[\hat{H}\rho] - \text{Tr}[\hat{H}\rho]_{V=0}$, where we include the latter term to subtract the single particle light shifts. Similarly, we calculate the dressed-atom decay rate (per atom) as $R_{sc} = (1/2) \sum_{\{\hat{L}\}} \text{Tr}[\hat{L}\rho\hat{L}^\dagger]$, which in the many-body system is the term that contributes to the heating of the ensemble and loss of dressed atoms. Figure 2.3 shows calculated two-body dressed state potential energy surfaces $U(C_6/d^6)$ and decay rates $R_{sc}(C_6/d^6)$ comparing the two-level and three-level systems. For this we have assumed van der Waals interactions with strength $C_6/2\pi = \pm 1.0$ GHz μm^6 , which is of the order of magnitude for alkali atoms excited to $n \sim 40$. The table in figure 2.3 show the parameters used for the calculations which were chosen such that both systems exhibit similarly small decay rates ($\lesssim 10$ Hz) and long-range effective interactions which ‘soften’ to a constant value $U^{(\infty)} = (U(V = \infty))$ at short distances ($d \sim 0$) as a consequence of the Rydberg blockade [38]. We note however that the three-level dressed potential

is considerably sharper (box-like) than for the two-level scheme, and its range is shorter due to the larger excitation bandwidth resulting in a smaller blockade radius. Another important difference between the three-level and two-level cases concerns the dependence on the sign of the bare-state interactions. In the two-level case the sign of V and Δ must be opposite to avoid level crossings which deform the potential and give rise to strongly enhanced decay (Fig. 2.3b red dashed line). In contrast, the shape and sign of the potential in the three-level case can be made independent of the sign of V since we can use Δ_e as a tuning parameter.

We now concentrate on the dressed-atom decay, where we observe a distinguishing feature for the three-level case. The decay rate here can be strongly spatially dependent, while for the two-level case the rate is almost constant everywhere and only shows a small reduction of R_{sc} at short distances. We examine two particular limits in the three-level system: $V = 0$ and $V \rightarrow \infty$ (related to very large and short interparticle distance, respectively). For large separations of the particles (i.e. dilute-gas experiments) the residual decay rate $R_{sc}^{(0)} = R_{sc}(V = 0)$ is minimized due to destructive interference of the intermediate state population due to electromagnetically induced transparency (EIT). On the contrary, at short distances (i.e. dense gases) the Rydberg blockade effect breaks the EIT condition leading to increased decay rates which plateau at a value $R_{sc}^{(\infty)} = R_{sc}(V \rightarrow \infty)$. This distance dependent decay may find applications in quantum state engineering via dissipation [150] or novel cooling techniques [151, 152, 153].

Figure of merit for two-photon excitation.

We take advantage of the different tuning parameters in the three-level system (i.e. $\Omega_e, \Omega_r, \Delta_e, \Delta$) to search for an optimal regime that maximizes the interaction potential $U^{(\infty)}$ while R_{sc} remains small. To ensure a small Rydberg state population we concentrate on the Autler-Townes regime [154] (two-photon resonance), focusing on the parameter region $\Omega_r \gg \Gamma_e \gg \Gamma_r$ and $\Omega_r \gg \Omega_e$. We analyze the case for small interparticle distances (i.e. $V \rightarrow \infty$) where we have already estimated a significant interaction $U^{(\infty)}$ (fig. 2.3). The characteristic decay rate $R_{sc}^{(\infty)}$ is plotted in figure 2.4a for the three-level system as a function of the intermediate- and two-photon detunings. The Autler-Townes doublet is clearly seen as bright bands for $\Delta_e = \Omega_r^2/(4\Delta)$ with a distinct minimum at $\Delta = 0$ caused by destructive interference of the intermediate state amplitude. We additionally observe two features for $\Delta_e = -(\Delta \pm \sqrt{\Delta^2 + \Omega_r^2})/2$ (Fig. 2.4b), which correspond to cooperative resonances between the two-atom ground state and the $|e_1\rangle|e_2\rangle$, $|e_1\rangle|r_2\rangle$ and $|r_1\rangle|e_2\rangle$ states.

In order to identify an optimal regime with large Rydberg-dressed interactions and at the same time small decay, we define a figure-of-merit for Rydberg dressing $f = U^{(\infty)}/R_{sc}^{(\infty)}$ and calculate it as a function of the two detunings, Δ_e and Δ . Figure 2.4b

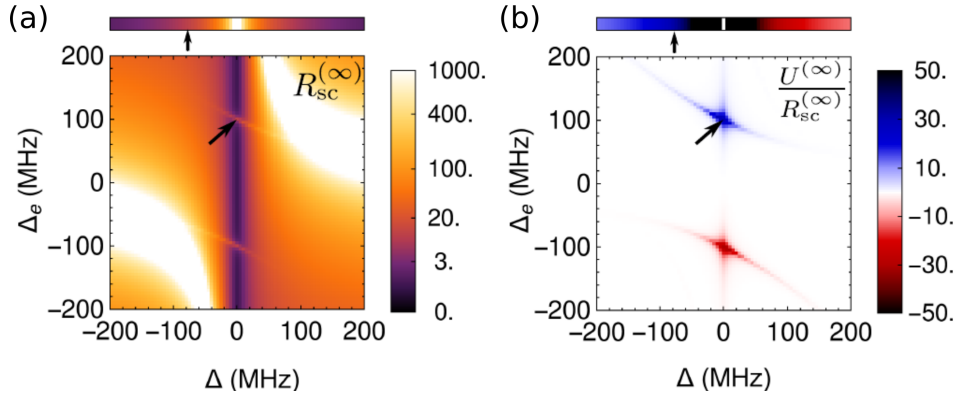


Fig. 2.4.: Analysis of the interaction potential and the scattering rate for the two-photon excitation scheme. (a) Decay rate per atom $R_{sc}^{(\infty)}$ for $V \rightarrow \infty$ corresponding to the fully blockaded limit. (b) Figure of merit $f = U^{(\infty)}/R_{sc}^{(\infty)}$, used to determine the optimal dressing conditions, where blue corresponds to repulsive and red to attractive interactions. The horizontal bars above each plot show the two-level parameters on the same colorscale as a function of the detuning Δ . Figure adapted from [122].

shows two optimal regions of repulsive (blue) and attractive (red) interactions where $U^{(\infty)}$ is large but $R_{sc}^{(\infty)}$ is relatively small because of the cooperative resonances. This reflects an enhancement, particular of the three-level system which does not appear in a two-level scheme. The optimal detunings are clearly revealed as dark crosses at the intersection of the two-photon resonance line and the cooperative resonances at $(\Delta, \Delta_e) = (0, \pm\Omega_r/2)$. A similar approach has been proposed, using molecular resonances to enhance a favorable regime, for specific pair distances and Rydberg states [41], however the cooperative enhancement reported here do not depend in principle of the Rydberg state and preserves the soft-core nature of the dressed potential since it is not mixed with molecular resonances. Additionally we expect that this cooperative effect is also present for more than two atoms [155], which may be beneficial to create collective many-body interactions in Rydberg dressing [65].

These results let us find a parameter regime where the interaction is enhanced while the scattering rate that leads to heating and dephasing is kept small in a three-level system. Despite the advantage of a single-photon excitation scheme where no intermediate state is involved (i.e. the scattering rate is only affected by the spontaneous decay from the Rydberg state), the two-photon excitation scheme also presents a competitive region with a remarkable figure of merit. Using these results we built a versatile laser system that can be used for both excitation processes, taking care of the most important requirements for Rydberg-dressed excitations, i.e. high laser power and low noise (see chapter 4).

2.3 Many-body physics using Rydberg atoms

The complexity due to the interactions increases exponentially when we start adding more interacting particles to the system. Solving the master equation of the ensemble (eq.2.8) is already very difficult for 10 particles because of the large Hilbert space. That is why simulations are usually based on approximations, depending on the particular characteristics of the system studied, which reduces the Hilbert space making possible the calculations. In this section we will introduce two models we have used to simulate the results of our driven-dissipative Rydberg experiments.

2.3.1 The mean field treatment

Mean field theory is one of the most common approximations used to reduce the complexity of many-body Hamiltonians. The approximation relies on averaging the interaction of one particle with the rest to an effective field, thus reducing the many-body problem to a one body problem, which strongly decreases the computational cost, while still some insight about the many-body behavior can be obtained.

In our particular many-body problem, we concentrate on the long-range Rydberg interactions for which we have to take into account the blockade effect which does not allow for a second Rydberg excitation below an interparticle distance (R_B , see section 2.2.2). The approximation in our case of the mean field interaction V_i for particle i is:

$$\sum_{i \neq j} V_{ji} f_R g_2(|r_j - r_i|) \quad (2.20)$$

with $V_{ji} = C_6/(|r_j - r_i|)^6$ the van der Waals interaction, f_r the Rydberg fraction and $g_2(|r|)$ the two-point correlation function. In the specific case of Rydberg interactions g_2 can be modeled as the step function $g_2(r) = \Theta(|r| - R_{Ryd})$ [156], where R_{Ryd} is the characteristic distance defining the blockade and facilitation radius. Next we replace the sum by an integral to calculate the effective interaction:

$$V_j \approx \int_{R_{Ryd}}^{\infty} f_R n_0 V_j i d^3 r_i \quad (2.21)$$

with n_0 the local density. This is a good approximation in the case the mean interparticle distance is much smaller than the characteristic distance R_{Ryd} , which is fulfilled in our experimental conditions. To calculate the effective interaction we need to impose the Rydberg blockade condition such that on average only one excitation is present within the blockade radius, which implies $\int f_R n_0 (1 - g_2(r)) d^3 r = 1$. Based

on this, we can integrate the interaction, using spherical symmetry

$$V_j = C_6 n_0 \left(\frac{4}{3} \pi f_R \right)^3 \quad (2.22)$$

which allows us to introduce the mean field interaction in the single particle Hamiltonian as an energy shift.

This model has been already investigated in Rydberg atoms and shown to reproduce the critical behavior related to the antiferromagnetic Ising model without including any dissipation [156, 157, 158]. In our simulations we include the mean field interaction in the full master equation (2.8) to model the open system dynamics. In chapter 5 we will see that the mean field approximation is useful to describe some regimes of our driven-dissipative system but fails for other parameter regions, that is why we explore another approximation for the dynamics in the next section.

2.3.2 Rate equation simulations: classical treatment

An efficient way to compute the behavior of many-body systems is via numerical rate equation (RE) simulations. The basic idea of the RE approach is to describe the excitation dynamics in terms of stochastic jumps between classical configurations approximated by single-particle transition probabilities. This approximation to classical systems allows us to computationally include the effect of disordered particles (e.g. atoms randomly distributed in a trap) or the influence of the potential landscape (e.g. position dependent energy shifts in the presence of an optical dipole trap). RE models enable efficient simulation of the steady-state and dynamics of large systems comparable to those realized in experiments. RE is valid to simulate quantum systems in the long term dynamics, where coherence is washed out due to decay and dephasing in the system. That is why RE simulations have proven very successful in reproducing the behavior of driven-dissipative Rydberg systems (in the presence of dephasing) [159, 160, 161, 155, 162]. We will show in chapter 5 that such simulations are appropriate to reproduce the experimental observations of a strongly interacting driven-dissipative system.

The rate equation model is based on the full quantum master equation 2.8 at long time scales (t) larger than the coherence time of the system (γ_{de}^{-1}), such that the coherence can be neglected and the treatment becomes classical. Starting from the quantum master equation we can adiabatically eliminate the coherences for each atom [159, 75, 163], i.e. set the temporal evolution of the off-diagonal terms to zero ($\dot{\rho}_{ij} = 0$ for $i \neq j$). This leads to the time evolution of the atoms described by single

jump rates:

$$\Gamma_r^j = \frac{\Omega^2(\Gamma + \gamma_{de})}{(\Gamma + \gamma_{de})^2 + 4(\Delta - V_j)^2}, \quad \Gamma_g^j = \Gamma_r^j + \Gamma \quad (2.23)$$

where $\Gamma_{g/r}^j$ is the jump rate of the ground or the Rydberg state of the j th particle and $V_j = \sum_k V_{jk} n^k$ accounts for van der Waals interactions on atom j depending on the instantaneous configuration of all other particles around. We approximate the slow loss out of the two-level subspace by evolving the classical rate equations from the fully excited state (blockaded) until the average fraction of Rydberg excitations has converged to its asymptotic value. This classical rate equation can be solved in an efficient way, including the temporal evolution, by means of Monte Carlo simulations.

This model also allows us to include the effect of atomic motion which we found necessary to introduce in the RE model to reproduce the observations of our experiment (see chapter 5). Thermal atomic motion can play a significant role in the dynamics especially in the facilitated excitation regime (for $\Delta > 0$) which can be interpreted as the atoms passing through the facilitation shell and undergoing a Landau-Zener transition [164, 165]. This can be incorporated in the RE model by adding a second term to Γ_r in Eq. (2.23) accounting for the velocity dependent Landau-Zener transition probability and the Maxwell-Boltzmann velocity distribution as well as the finite lifetime of the Rydberg state (see appendix in [74]).

Another advantage of this model is that the local position of each atom at each particular time can be simulated. This enables the inclusion of the atom density distribution along the trap and also the spatial dependence of the light shift caused by the trapping potential. As we will see in chapter 5, the scattering rate behavior of the data cannot be reproduced by a homogeneous system simulation. Furthermore, it may be surprising in general that the RE model can reproduce the system behavior since it neglects any coherence. We attribute this to the fact that our experiments focus on a relatively simple observable in the long time limit after which any observable effects of coherent dynamics are effectively washed out. Nevertheless striking characteristics of the driven-dissipative can be observed and simulated.

2.3.3 Towards a long-range interacting platform for non-equilibrium studies

This chapter has covered the most important characteristics of Rydberg atoms, including single body properties such as their high sensitivity to electric fields. We additionally present the different emergent effects, such as Rydberg blockade and facilitation, arising from the Rydberg-Rydberg interactions. Furthermore we have introduced the concept of Rydberg dressing, as a detuned excitation where the

ground state acquires the interaction properties of the Rydberg atom while keeping the decay rate small. For this approach we defined two main requirements: a high-power excitation laser to compensate for the small dipole coupling and low laser noise to avoid extra dephasing in the system. Furthermore, we focused on studying the two different Rydberg dressing schemes: one- or two-photon excitation. Based on simulations of the two-body interaction and decay rates, we encountered a favorable regime for the three-level system, where cooperative effects reduced the decay rate while keeping the interaction large. Moving towards studies in the many-body regime with long range interactions we have also presented two main models used to describe the dynamics of a Rydberg system: mean field theory and the rate equation model. These models will prove to be very useful to describe our results in chapter 5

All characteristics from Rydberg atoms combined to offer a platform for studies of many-body systems. In particular this system is well suited for studying physics out of equilibrium given the inherent properties of the Rydberg atoms, i.e finite lifetime, atom-light coupling and long-range interactions. Non-equilibrium phenomena corresponds to the physical situations where the system is constantly in contact with the environment such that it exchanges conserved quantities like energy or particles. This coupling can be characterized as a macroscopic current that drives the system out of the equilibrium state to a dynamical evolution [166]. Non-equilibrium phenomena is usually classified in two general types depending on how the system is coupled to the environment [167]: continuously driven out of equilibrium or suddenly changed (quench) followed by the relaxation to an equilibrium state. The Rydberg platform provides a testbed for both types of phenomena since the laser coupling to Rydberg states can either be continuously on or switched suddenly (quench). The following two chapters (3 and 4) will present the experimental platform for realizing long-range interacting Rydberg atoms while chapter 5 shows a direct application for the studies of non-equilibrium dynamics.

Experimental platform for Rydberg dressed potassium

To perform precision measurements and study the dynamics of a quantum system, a good control over the particles and advanced techniques for manipulation, excitation and read-out are required. One of the main conditions is a well isolated system from the environment, as it is necessary for example in the case of an atomic clock to prevent frequency shifts caused by external factors. The second requirement is the control of external degrees of freedom (such as the atoms kinetic energy) and the internal electronic states of the atoms. The next condition is a precise and versatile detection of the particles including the discrimination between atoms in different internal states. This allows for a complete analysis of the system and its dynamics. The final prerequisite is more specific to our system, namely that, the Rydberg excitation laser system should be powerful, tunable and with low noise as it is concluded from chapter 2. In this chapter we concentrate on the different approaches we have used to fulfill all these requirements to create an ultracold platform, except for the last one, which is further described in detail in the chapter 4.

This chapter covers a complete overview of the experimental platform regarding the atom sample preparation in the ground states without any Rydberg excitation. The first part covers a detailed description on the main components of the experiment including the vacuum apparatus, the laser system for cooling and trapping and the experimental program used for control, read out and analysis. In the second part of this chapter the main ingredients for the preparation of the atomic sample are described. This includes the control of external magnetic fields, the evaporative cooling mechanism to reduce the atom sample temperature to hundreds of nK, the radio-frequency control of the atom population in the hyperfine ground states and the spin polarization technique used to prepare the sample in a single $|F, m_f\rangle$ state. The result is a compact and controllable experimental platform which is the starting point for the creation of Rydberg excited states and for the following studies on non-equilibrium phenomena and coherence properties of the Rydberg ensemble.

3.1 The ultracold atom system

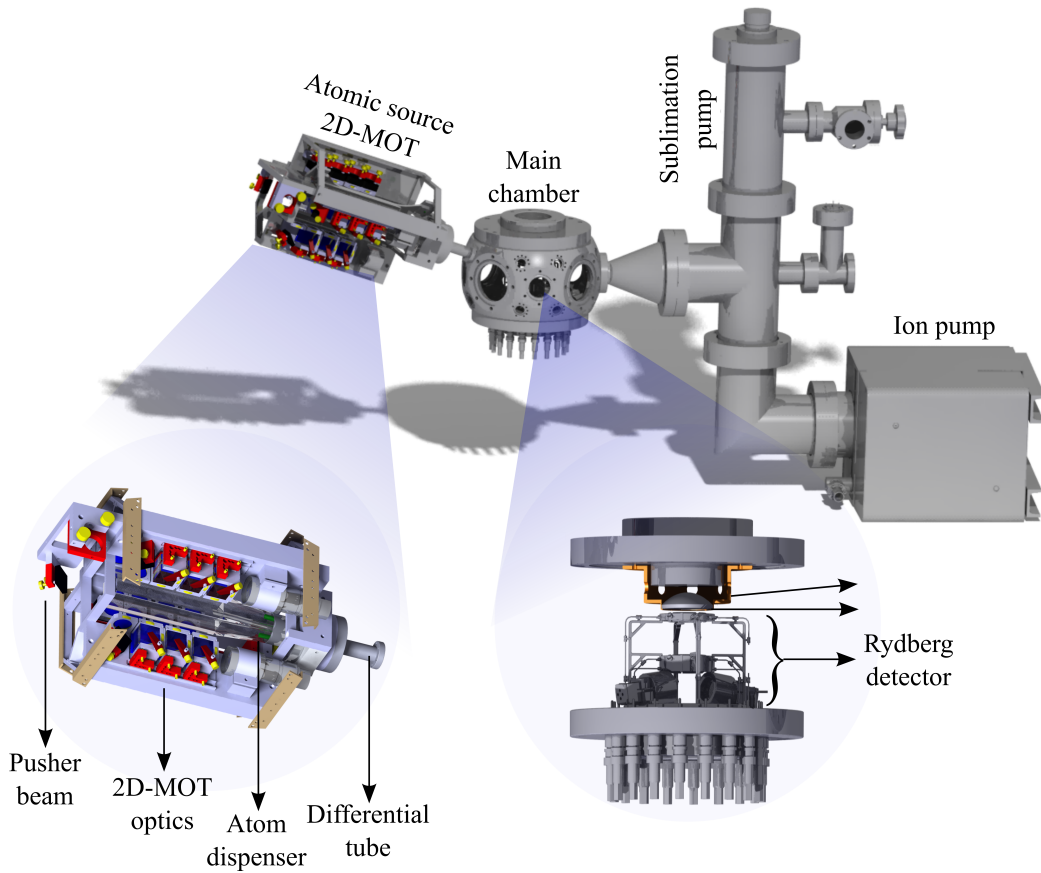


Fig. 3.1.: Overview of the experimental apparatus. All the main parts in the experimental setup are depicted in here. The atom source (left) is a potassium dispenser placed inside a glass cell, where the optics around it constitute the 2D MOT (see zoom in) which creates an atom beam cold in the transversal directions that is pushed towards the main chamber (center in the figure). The atoms go through a differential tube into the main chamber, where they are trapped and cooled further. Inside the chamber a MCP Rydberg detector, a high resolution imaging lens and a radio-frequency antenna are placed for state control and manipulation. The high vacuum in the chamber is mainly maintained via the ion pump and the sublimation pump (right to the main chamber). Image adapted from [168].

The starting point of most of the experiments performed within this thesis is an ultracold atomic sample of potassium atoms trapped in a crossed optical dipole trap. We achieved typical temperatures of $\sim 20\mu\text{K}$, with peak densities of $2 \times 10^{10}\text{cm}^{-3}$, although much lower temperatures have been achieved with the apparatus (see section 3.2.3). In this part of the chapter, the experimental apparatus is introduced and the techniques corresponding to the first stages of trapping and cooling are presented.

3.1.1 The vacuum apparatus

In order to fulfill the condition of good isolation from the environment we make use of a mechanical, which is mainly based on a vacuum chamber¹. This allows to obtain quite low pressures of about 10^{-10} mbar, which is necessary to reduce collisions between the trapped atoms and the background particles. Otherwise losses caused by these collisions will dominate over the actual dynamics of the system and the experiment would not be reliable as an ultracold atom platform.

In order to achieve and maintain the low pressure inside the vacuum chamber, a set of vacuum pumps are needed (see figure 3.1). The first one is an 125 l/s ion pump² which ionizes the gas inside the chamber and attract the ions towards the pump using a high electrical potential. The second one corresponds to a titanium-sublimation pump³ which by means of high current sublimates a titanium filament. The titanium attaches to the internal walls of the chamber and since it is very reactive, any particle that touches the wall will react with the titanium forming a solid component, thereby reducing the pressure.

We combine the steel vacuum system with viewports to enable optical access of the different laser beams required for cooling, trapping and Rydberg excitation. The main chamber has ten main viewports (placed in the horizontal plane and the vertical axis) plus some small ones. They are made of fused silica, vacuum sealed and adequately coated depending on the laser wavelength and power planned to go through. The great amount of viewports allows ample optical access, giving high flexibility in the number of beams used in the experiment and their wavelength.

Inside the main chamber three additional elements have been included (see zoom in, figure 3.1). A high resolution imaging lens⁴ designed for single site fluorescence imaging (section 3.1.3). The lens has a focal length of 32 mm, numerical aperture of 0.62 and a special coating⁵ in order to avoid accumulation of charges on the lens surface which can affect any measurement due to the sensitivity of the Rydberg atoms to electric fields (see chapter 2, section 2.1.2). The second element in the main chamber is a radio frequency antenna, made out of a coil wrapped around the inside-vacuum lens holder. The third component is a Rydberg detector made of an electrode structure that enables the compensation of stray electric fields, the generation of a homogeneous electric field and the creation of high electric fields to ionize the Rydberg atoms and accelerate those ions. Additionally two deflection

¹Kimball Physics. 8 Multi-Cf Spherical Square MCF800-SphSq-G2E4C4A16.

²Agilent technologies. VacIon Plus 150 Ion Pump StarCell

³Agilent technologies. TSP Cartridge Filament Source

⁴Asphericon A45-32 HPX

⁵ITO (Indium thin oxide) coating

rings are used for controlling the trajectory of the ionized atoms towards the micro-channel plate (MCP). All these elements combined contribute to a better control and measurement of the atomic sample as explained in further detail in the following sections.

3.1.2 Laser cooling and trapping of ^{39}K

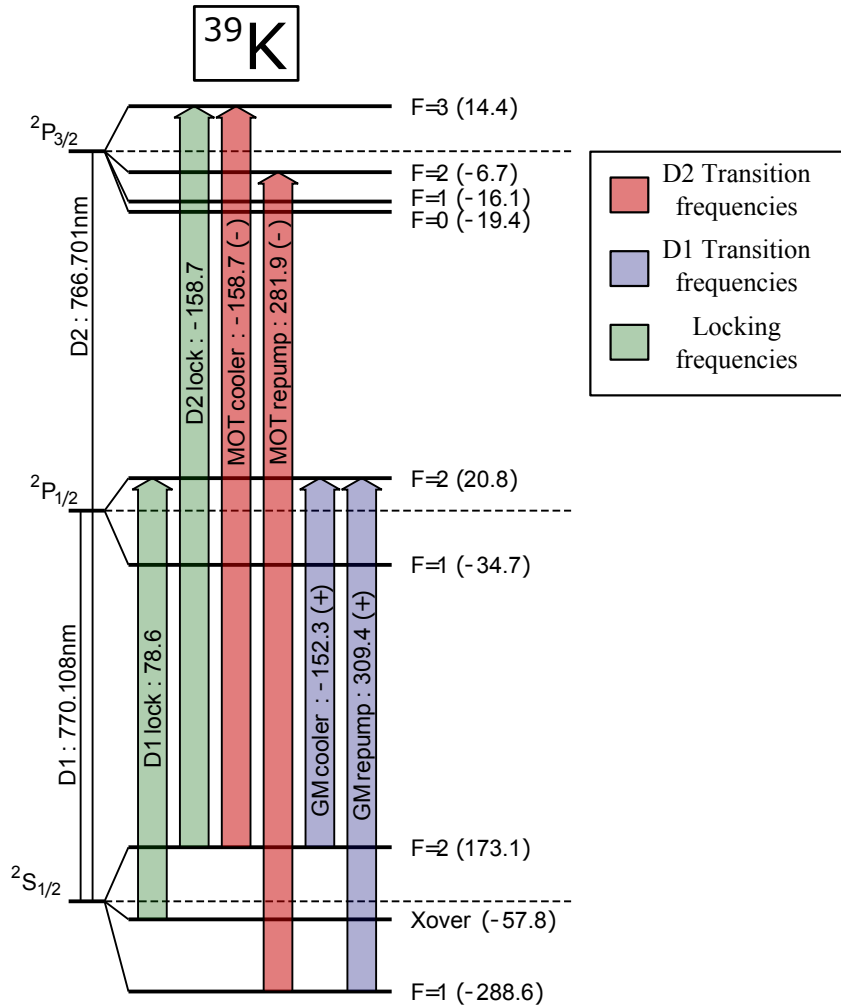


Fig. 3.2.: Level scheme of potassium 39 and laser beam frequencies for the MOT. Two main transitions in ^{39}K : $|4S_{1/2}\rangle \rightarrow |4P_{1/2}\rangle$ and $|4S_{1/2}\rangle \rightarrow |4P_{3/2}\rangle$ (D1 and D2 transitions respectively) are depicted with their corresponding hyperfine splitting. The blue arrows represent the cooling and repumping beam frequencies for the D1 transition while the red arrows represent the same for the D2 transition. The green arrows correspond to the two frequencies (for the D1 and D2) used for locking the two lasers to the spectroscopy signal. Figure adapted from [169]

An important requirement for our ultracold platform is the control of the atoms in terms of the external degrees of freedom, e.g. thermal motion and spatial confinement. In our case we have chosen to work with potassium because it has stable bosonic and fermionic isotopes, i.e. ^{39}K , ^{40}K and ^{41}K . This particular characteristic allows for versatility, since in the quantum regime the dynamics will be governed

either by bosonic or fermionic statistics, and furthermore, by including Rydberg excitations a competition between the particular statistics of the ground state and the long range interactions can lead to new states of quantum matter [48, 49, 50, 51].

Level scheme of potassium 39. Within this thesis only potassium 39 has been used, nevertheless the experiment has been planned and executed with the capability of trapping and cooling two isotopes (^{39}K and ^{40}K) [170]. Figure 3.2 shows the level scheme for the valence electron in potassium 39, regarding the ground state ($4S_{1/2}$) and the first two excited states ($4P_{1/2}$ and $4P_{3/2}$). The transition between the ground state and the first excited state is usually referred as the D1 transition while for the second excited state is the D2. In the experiment we have two different diode lasers specialized to address each of the transitions, which allow some flexibility for better cooling and trapping as explained in the following.

Laser system for simultaneous cooling and trapping. For the first trapping and cooling stages we exploit the D1 and D2 transitions (see figure 3.2). In the experiment two diode lasers⁶ at the corresponding wavelengths (767 nm and 770 nm) for both transitions are used. A couple of mW are passed through a heated potassium vapour cell (temperature 60°C) and by means of modulation transfer spectroscopy (MTS) [171, 172] we obtain an error signal for locking the laser to the $|4s_{1/2}, F = 2\rangle \rightarrow |4p_{3/2}, F' = 3\rangle$ transition of ^{39}K [173]. This locking technique has the advantage of suppressing open transitions and crossover resonances while enhancing the cycling transitions, thus leading to a stronger and more robust error signal [174]. The measured locked 767 nm laser linewidth is 120 ± 20 kHz. The main light is fibered coupled and combined into the first amplification stage which is based on a home built tapered amplifier [175] that can be seeded with either one of the light beams. We allow for the amplification of one of the wavelengths or the other via an electro-optical modulator which change the polarization of the beams, which with a beam splitter can be selected. The current amplification is from about 10 mW of seed light to 500 mW of amplified power. This light is again fiber coupled (for beam pointing and spatial mode filtering) and redistributed into other three amplification stages (TAs), namely for the 3D cooler, the 2D cooler and the repumping branch (see fig. 3.3). Before the amplification stage each light beam goes through an acousto-optical modulator (AOM) in a double pass configuration in order to shift the light frequency such that each beam can address the required transitions (see scheme in figure 3.3). After amplification and frequency shifting, each beam goes into a fiber to the science chamber (figure 3.1). More precisely the laser light for cooling and repumping is combined in a homebuilt module by means of waveplates and beam splitter cubes as described in [170]. The combined light is then coupled to fibers which are distributed along the three main axis in the

⁶Toptica. Tunable diode laser, DL pro

experiment to cool and trap as explained in the next part. The versatility of this setup includes the possibility for trapping potassium 40, even if the energy splitting and atomic transitions are considerably different to potassium 39 [176]. The current design allows for a readjustment of the frequencies by changing the diffraction order of some of the AOMs in double pass configuration as presented in [170]. Based on this compact, versatile and high power setup, we are able to cool and trap potassium, as shown below.

Atomic source and magneto-optical trap. The experiment starts at the atomic source, which is a dispenser ⁷ set in a glass cell (sketched in figure 3.1). This is heated by a DC current of about 2 A, releasing potassium into the glass cell. The atoms are first cooled within this glass cell via a two-dimensional magneto optical trap (2D MOT) and then directed into the main chamber to be trapped in a 3D MOT.

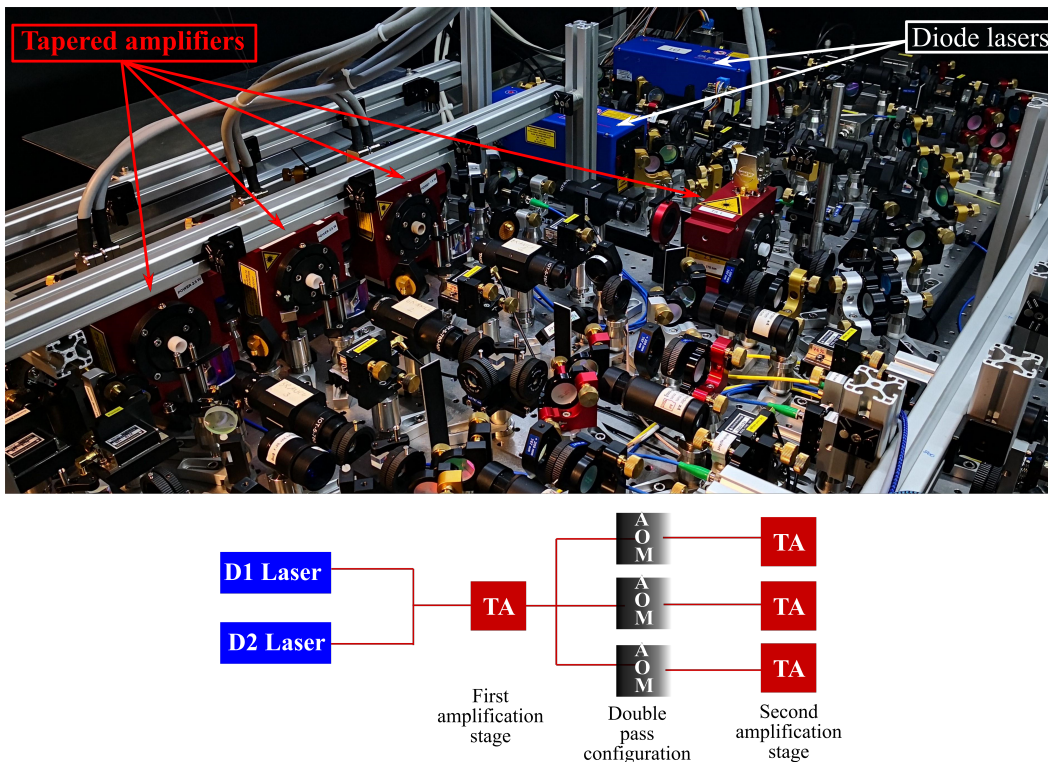


Fig. 3.3.: A versatile and compact laser system for laser cooling and trapping. Upper figure shows a picture of the condensed experimental setup with all the main components (diode lasers, tapered amplifiers and acousto-optical modulators) for cooling and trapping in the MOT. The lower figure is a simplified scheme of the power amplification and beam distribution of the laser system.

The general principle of a MOT is to exploit velocity dependent absorption of photons which by reemission reduce in average the kinetic energy of the atoms. Additionally

⁷Alvatec AS-3-K-100-F

a magnetic gradient is combined with red-detuned circularly polarized light, to spatially confine the atoms, where the ones propagating in the opposite direction of the beam are more likely to go under a cooling transition. This generates a net force pushing the atoms in average towards the center (in the direction of the zero magnetic field). In order to trap and cool all atoms in the ground state we make use of two different transitions: $|4S_{1/2}, F = 1\rangle \rightarrow |4P_{3/2}, F = 2\rangle$ and $|4S_{1/2}, F = 2\rangle \rightarrow |4P_{3/2}, F = 3\rangle$, what we call the repump and cooling beams respectively (see figure 3.2). This avoids the atoms to accumulate in one a hyperfine-ground state that is not addressed via the lasers.

Inside the glass cell in the 2D-MOT the atoms are cooled down in the transversal plane by eight retro-reflected beams, four in each direction (the designed was implemented from [177]). This creates a relatively cold atom beam that is directed through a differential pumping tube into the main experimental chamber. We make use of an extra beam resonant with the cooling transition to push the atoms towards the center of the main chamber (named pusher in figure 3.1). In the chamber six counter propagating beams (combining cooling and repumping light in one beam through the homebuilt module [170]) are used, two per axis. This combined with a magnetic quadrupole field (created by a pair of coils in an anti-Helmholtz configuration) allows us to trap and cool the atom cloud down to few mK.

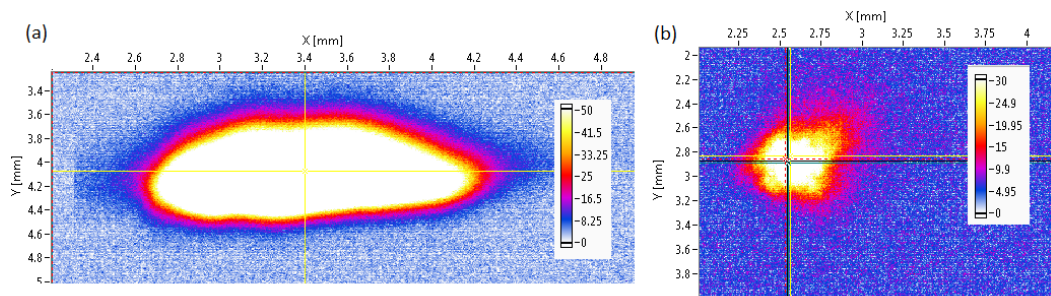


Fig. 3.4.: Potassium 39 and potassium 40 in a MOT (a)Fluorescence image for ^{39}K in the compressed MOT. (b)Fluorescence image of ^{40}K in a MOT, which has a natural abundance of 0.01%.

With the aim of enhancing the atom loading into the dipole trap, a large spatial overlap between the MOT and the dipole trap (introduced in the next section) is required. However the MOT is originally large (\sim mm size) in order to trap as much atoms as possible coming from the 2D MOT. Due to that we need to add an intermediate step that reduces the spatial distribution of the atoms, such that an efficient load into the dipole trap is possible. This step is referred to as the compressed MOT where we ramp up the magnetic field gradient to make the spatial confinement tighter and we also adapt the detuning of the cooler and repumper beams since the energy levels of the atoms are further split due to the high magnetic

field. Figure 3.4(a) shows a fluorescence image of the compressed MOT for ^{39}K and as a comparison in (b) the fluorescence for a normal MOT of ^{40}K is presented. This gives us a good spatial confinement for the overlap with the dipole trap, however lower temperatures are also necessary since the dipole trap has a finite trap depth $\sim 1\text{mK}$ and atoms with such temperatures will easily leave the trap. That is why we use an extra cooling technique, presented in the next section.

Gray molasses. The basic principle is based on blue-detuned driving transitions from the ground states to excited states where at least one of the ground states ($|F, m_f\rangle$) is dark, i.e. not coupled to the light. In order to achieve this, the two coupled hyperfine states should have total angular momentum such that $F \leq F'$, where $'$ indicates the excited state. Additionally the light field that drives the transitions has to be circularly-polarized and counter propagating such that the bright states (the ones addressed by the light field) experience an oscillating potential [178]. An atom moving through this field will climb up the potential hill losing kinetic energy and increasing the probability of being excited, afterwards it will decay either to the dark state or to one of the bright states to repeat again the process. This is in principle the Sisyphus cooling mechanism [178] where by climbing up the potential hill, the atom loses in average kinetic energy. The atoms could in principle quickly accumulate in the dark state, however due to motional coupling they can go back to a potential valley of a bright state close by in energy. This enables the atoms to further undergo the Sisyphus cooling scheme.

For the specific case of ^{39}K this technique has been developed in detail in [179, 180]. We use the D1 transition because of the larger hyperfine splitting (compared to D2) which allows to resolve the addressed state better (see figure 3.2). Two different light frequencies are then used to drive each hyperfine ground state with a blue detuning. The involved transitions are: $|F = 1, m_f\rangle \rightarrow |F' = 2, m_f\rangle$ (repumper light) and $|F = 2, m_f\rangle \rightarrow |F' = 2, m_f\rangle$ (cooler light), following the requirement: $F \leq F'$. This cooling technique allows us to reduce the cloud temperature to tens of μK , which is an excellent starting point to load the atoms into the optical dipole trap, as we will see in the following.

3.1.3 Far detuned optical dipole trap

Basic principle of an optical dipole trap. Optical dipole traps (ODT) have become a standard technique used in ultracold atoms [181]. This approach is based on the interaction of the ground state atoms with a laser far detuned from any electronic transition. One of the main advantage is the possibility of trapping atoms in different states and even from different species at the same time. Furthermore, given that the frequency is far-detuned from any resonance, the amount of scattered photons

is reduced, resulting in a small heating and long lifetime of the atoms in the trap, which then is only limited by the background collisions and other possible collisions within the trap.

In the semi-classical approximation where the atom is considered a two-level system and the light a classical radiation field, the atom experiences an oscillating dipole moment in the presence of the laser field. This dipole in turn will interact with the laser electric field creating an induced dipole moment $U \sim P \times E$, with P the induced dipole moment which oscillates with the laser frequency and E the laser electric field. P depends on the atom polarizability which can be estimated by considering the atom as a classical damped harmonic oscillator [181]. This leads to $U \sim I/\Delta$, with I the laser intensity and Δ its detuning. This relation shows a relevant characteristic of ODTs: for $\Delta < 0$, U is negative and therefore the atoms are attracted towards the intensity maximum of the trapping laser, while in the opposite case ($\Delta > 0$) atoms are trapped at the minimum intensity. This characteristic allows to manipulate the potential landscape by a combination of different laser traps. For our experiment we only use red-detuned ($\Delta < 0$) optical traps.

The ODT laser system and its atom loading. Given the relation of the trapping potential with the laser intensity and the detuning, it is necessary to compensate a large detuning (to reduce off-resonant scattering) with a high intensity laser. In our experiment we make use of a Mephisto MOPA laser system, which consists of a stable low-power single-frequency laser diode and four amplification stages, which have a Nd:YAG crystal that works as a resonator with its end faces as mirrors. The result is a maximum output power of 55 W at a wavelength of 1064 nm.

We couple part of the dipole trap beam into a fiber and focus the output beam into the atoms to a waist of 100 μm , afterwards the beam is reflected and focus again into the atoms. This creates a shallow-angle crossed dipole trap with double the intensity compared to only just one beam. This is the trap where we perform most of the main experiments presented in the framework of this thesis, if not stated otherwise. Figure 3.5 shows an absorption image of the atoms confined in the optical dipole trap.

In order to load the atoms into this trap, we exploit the gray molasses cooling technique such that we cool and load the atoms simultaneously. To optimize the loading we scan the detuning of both cooler and repumper beams and compared the atom cloud optical density after letting the atoms expand without the trap for 6 ms. Further characterization of the gray molasses in our system can be found in the master thesis [168]. The final result is an atomic cloud with approximately 10^5 atoms, an atom density up to $2 \times 10^5 \text{ cm}^{-3}$ and with typical temperatures of $\sim 20 \mu\text{K}$. This is the starting point for the characterization of the Rydberg system and the

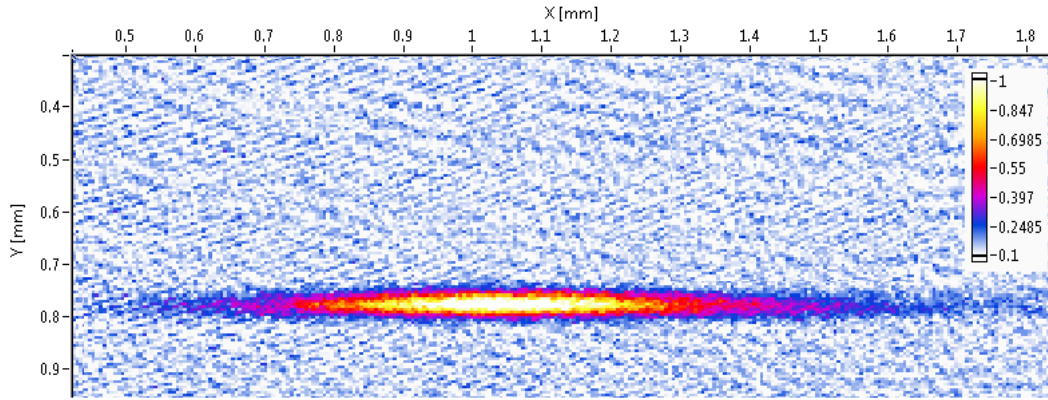


Fig. 3.5.: Absorption image of potassium 39 in a tight optical dipole trap. Atom are loaded from the compress MOT into the ODT while they are cooled via gray molasses.

experimental realization of a Rydberg-dressed atomic clock.

Versatile trap design: Towards a quantum gas microscope. Besides the cross dipole trap, the experiment has been designed such that other types of traps (i.e. lattices and two-dimensional traps) can be created from the same optical dipole trap laser system. The two-dimensional trap is made by a single light sheet in the horizontal plane that strongly confines the atoms in the vertical direction. It is built by taking part of the dipole trap light and shaping the beam with a 4f setup of two spherical lenses and two cylindrical lenses (further details in [168]). The lattice is created out of three interfering beams: two counter propagating (done by retro-reflection of one beam) and a third one perpendicular to them in the horizontal plane (the specific design can be found in [182]). All three beams create a pattern of vertical tubes that can be confined in the vertical direction with the pancake trap, to create a 3D trap.

Besides the versatility in the trapping geometry, we want to combine these traps to create a confined lattice in the focal plane of the in-vacuum lens to perform single atom fluorescence imaging, a technique also known as quantum gas microscopy [183, 184]. The basic principle of this technique is to resolve each atom trapped in a single site via fluorescence imaging. However since a good signal to noise ratio from a single atoms is required to gather enough fluorescence usually requires long exposure times to the light (of the order of a second). That is why a cooling technique is required while collecting the atoms fluorescence such that the atoms are not heated and remain trapped. In our case, we plan to use gray molasses to keep the atoms cooled down while taking the fluorescence image. As discussed in the conclusion chapter 7, this capability opens new possibilities having a better spatial control and high resolution detection.

3.1.4 An adaptable program for experimental control and analysis

Based on the experimental set up, it is clear that there is a big set of parameters that required to be initialized and controlled during an experimental sequence. Those parameters are related to different devices such the power of a laser beam determined by the RF power that goes into the AOM. In order to achieve consistent and reproducible experiments we require a program that can control all the devices in the setup. Such a program would have the advantage of time saving due to automation and also give the user an overview of the whole experiment and the possible parameters that can be adjusted.

Given the complexity in our experiment this experimental control program has been designed based upon four criteria:

- An independent structural program such that new devices can be easily implemented, this is crucial since our experiment is growing and needs new capabilities over time
- Flexibility to adjust the experimental sequence including all relevant parameters and also devices, which should be able to be deactivated, activated or used in different parts of the sequence
- Automation of processes should be possible, for example repeat continuously a sequence or scan a parameter with a different value in each sequence
- The acquired data from the measurement should be properly saved as well as all the devices characteristics and parameters of the sequence such that the exact configuration can be recovered anytime

In our case we base our program in a well-known programming language for experimental physics, Labview. This has the advantage of a higher level programming structure, i.e. it does not required to program the low-level hardware commands. Especially since most of the hardware use in ultracold atom experiments come with labview programs to interface the device, such a hardware programming is not necessary. The first version of this experimental control program was developed in the group of prof. Matthias Weidemüller, within a master thesis project. Further programming like the inclusion of new camera devices and utilities, new logic box hardware and data saving facilities, have been done within this thesis.

Labview program modular structure

Labview is an user oriented program based on a visual programming language. It implements user interfaces directly into the developing code and is based mainly on virtual instruments (VIs) which are subroutines with adjustable inputs and outputs. The general design of our program is that it can be structured in sections that work independently and can communicate with each other. This is very convenient for our purposes since we can use one section for each type of device or task (what we call module), and utilize a overall structure to manage those modules, for further detail see appendix A.

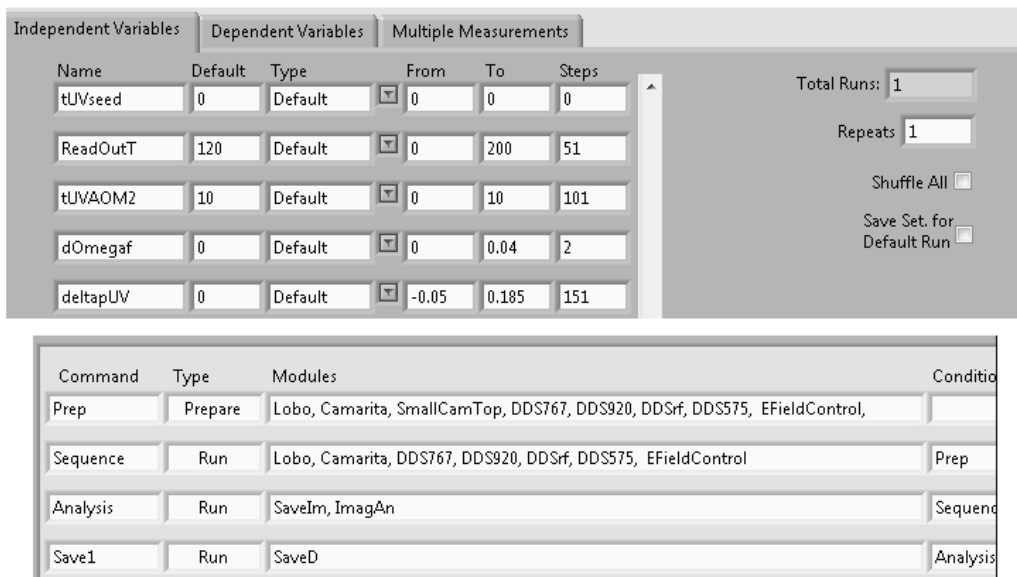


Fig. 3.6.: The variable controller and run controller. The upper panel shows the interface of the *variable controller*, where a list of all variables are shown. Depending of the type of attribute (third column) the variable can have always the same value (Default) during a scan or it can change every run. The lower panel shows the *run controller* interface. It is mainly a list with the order in which the modules have to be prepare and run.

The main program was designed with two sub parts (shown in fig. 3.6) for a better control of the devices and tasks. The first one is the *run controller* which takes care of triggering the execution of the modules and of the order in which they are prepared and run, since not all the modules have to run in parallel. For example the image analysis module should run after the images are acquired, i.e. after the camera module is run. The second part is the *variable controller*, which manages the values of all variables used in the experiment. This is particularly useful for scanning a parameter in the experiment such as a laser frequency or a beam power. The variable value can be changed every run either in a linear fashion, a logarithmic one or a double ramp where the variable is scanned from the initial to the final value and then backwards. Figure 3.6 shows an example of both controllers interfaces. The

variable controller has an additional functionality: multiple measurements, where many scans of different variables can be set to run.

The main VI that loads and connects all the necessary elements for running the experimental control program is the "QD-Control.vi", the corresponding user interface is depicted in figure 3.7. It includes the commands to start or stop a run, to load a specific configuration (including all the parameters of the modules) and to save the current sequence. Additionally below the start run button a list of all types of run can be displayed to choose the run mode. This includes: a default run mode where all variables are fixed to its default value, a controlled run mode where all the variables selected as "linear", "logarithmic" or "tomo" are scanned within the given range values (see variable controller in figure 3.6), and a multiple run mode, to do many scans of different variables one after the other.

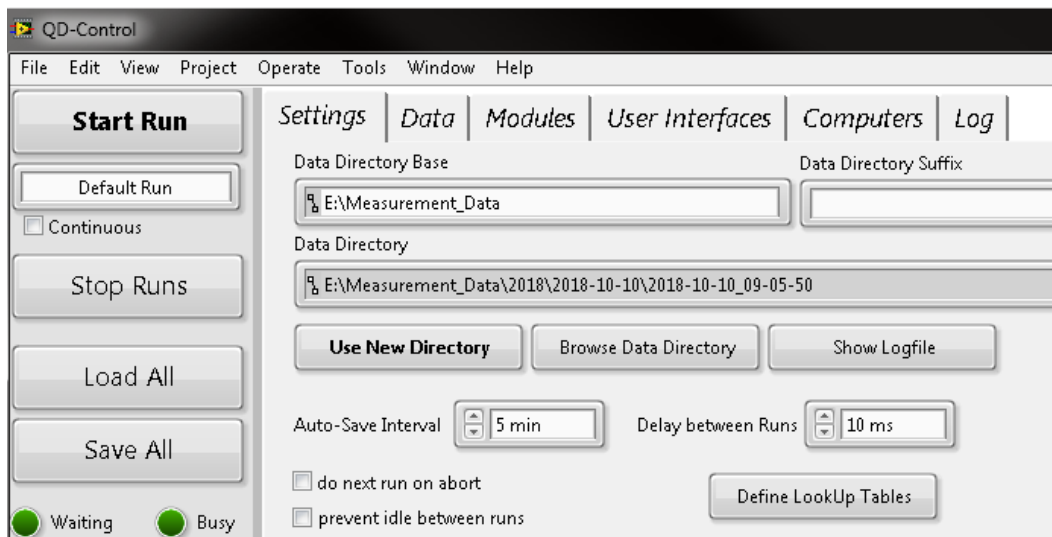


Fig. 3.7.: Main window of the experimental control program. The left column shows a set of buttons to start, stop, load and save the experimental sequence. The right panel contains the basic settings to determine the folder where the data has to be saved.

The right panel in the main interface shown in figure 3.7 has a set of different tabs that control or show all the relevant attributes in the program. The settings tab include all the parameters to create and use the directory where the data has to be saved. The data tab shows the data (name and type) that is common for all modules like the fitted parameters from an absorption image. The modules tab is mainly the interface for managing the modules, which includes a list of all the created modules, their respective type, location within the user interface and whether it is activated or not. Within this tab is possible to create new modules or delete the existing ones. The user interfaces tab is used to create a lab interface in order to arrange all modules and controllers in a window. The computers tab is a module to log and control other computers with the same experimental program, one being the master

computer and the rest the slaves. This can be used to trigger a parallel program that can be focused only in one device or task, e.g. image analysis or oscilloscope read out. The last tab log shows all the logging details of the specific computer.

For this program we have also implemented an extra dynamical component, which consists of an active loading of the modules every time the program is launched. This has the advantage that depending on the instruments and tasks required for the experiment, it is possible to choose to load only certain modules. For example while testing an specific device, it is not required to have all the devices connected or in the case that a new setup is used where less modules are required this would avoid the time consuming task of installing drivers for devices that are not used. The way the program is dynamically loaded is by reading a simple text file with a list of the modules that are to be used in the experiment.

Logic box: control for most of the devices. The logic box (LB) is a device based on a field programmable gate array (FPGA) design for controlling and reading different instruments. This LB was designed and created by the electronic workshop of the physics institute at the university of Heidelberg. Within the design a Labview library (the *logic pool*) has been developed with the basic VIs to control the Hardware, facilitating the programing since all the low-level commands are embedded in the library. Based on this we have created a module in the actor framework that can control all the types of logic boxes created up to now.

The main components of the LB in our case are: digital input/output (DIO), digital-analog converter (DAC) and analog-digital converter (ADC). The DIO generates a binary output, i.e. transistor-transistor logic (TTL) signal with maximum voltage of 3.4 V. The DAC channels can generate voltage outputs within ranges (that can be adjusted) for $\pm 5V$ and $\pm 10V$. The ADC inputs are used for readout of voltages such the signal from an oscilloscope or a photodiode. The applications of the logic box vary from trigger signals to control of the output of some instruments. In our case we used the logic box for many different purposes such the control of the acousto-optical modulators (turning them on and off, change the frequency and diffraction power), sending trigger signals like the one required for the cameras to know when to record a picture, sending combined TTL signals to set the position of a translation stage or read out the voltage value of a photodiode measuring the intensity of a beam.

Figure 3.8 shows the main interface used for controlling the logic boxes in the experiment. The "define channels" button allows the user to define the settings of the logic boxes. The user can choose which LB is the master, which sets the trigger and clock signal for the other LBs. Additionally the user can name each channel in the LBs and change settings like the voltage range of the DACs. Based on the channel names, the user is able to manipulate the channel's value and create

sequences with different channels and timings as shown in figure 3.8. The program allows the user to create as much sequences as needed (called sub-sequences) which can be put together to create the main sequence (right panel in figure 3.8). The sub-sequences can be turned on/off, repeated and shifted at will, which is very useful for example when debugging a problem in the whole sequence, one could turn off some subsequences and check if the result is the expected one with those few subsequences on. In brief, the logic box module is the core of the experimental sequence where most of the devices are set and controlled.

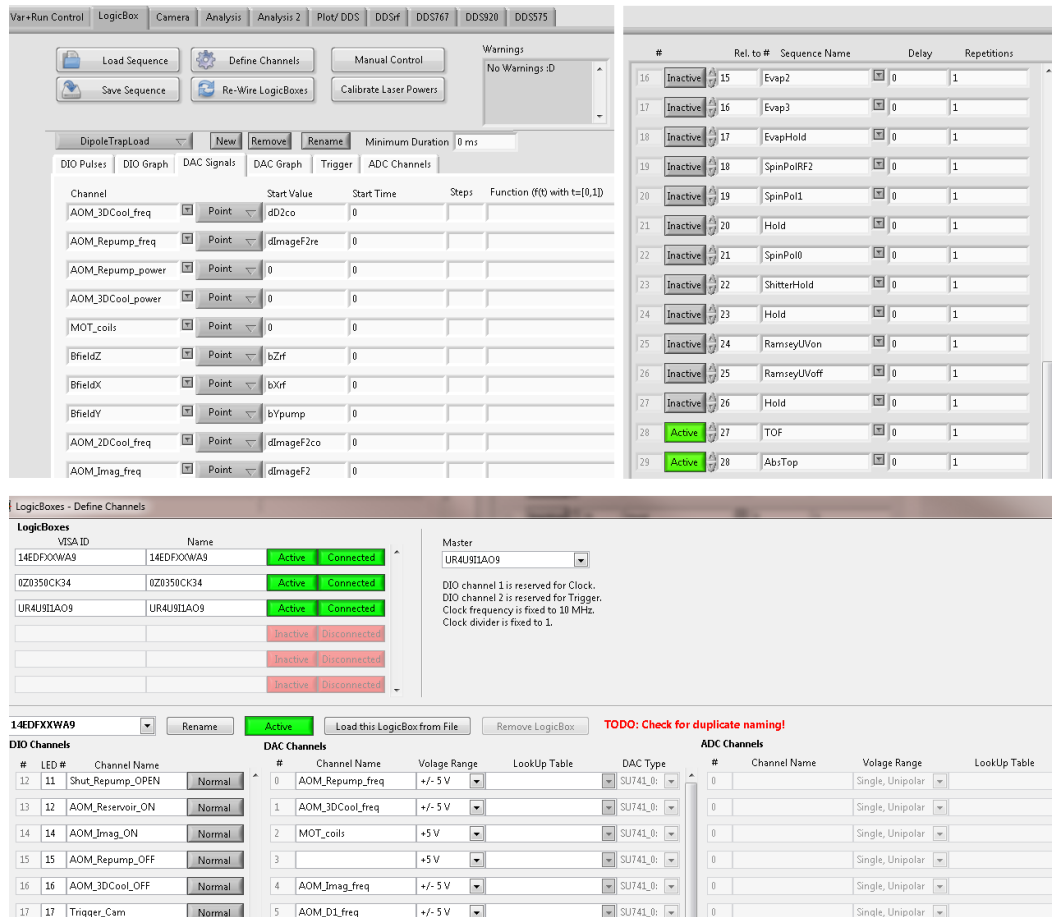


Fig. 3.8.: Logic box module interface. (Upper panel left) Main logic box window where a subsequence can be created by including the different channels that must change, their values and timings. (Upper panel right) List of all subsequences and the order they should be run, including a delay time in between and a number of repetitions, if necessary. (Bottom panel) Main window to define the channels in each logic box. In the upper part the logic boxes that are connected can be activated, and one of them must be chosen as the master box. In the lower part, all types of channels belonging to a specific logic box are listed, their names and some attributes can be changed.

Within this thesis I have also modified and implemented different modules to manipulate the experimental machine. This included a flexible module for absorption and fluorescence imaging with different cameras, an analysis module for the taken

images and a set of modules for saving the raw images and the analyzed data. A detailed explanation of the experimental control program and its most important modules can be found in appendix A. With this program we are able to have reproducible experiments, automatic data collection and the flexibility to adapt it for future updates in the experiment.

3.2 Atomic sample preparation

Having shown the capabilities of the experimental setup to trap and cool the atoms up to densities of $\sim 10^{10} \text{ cm}^{-3}$ and $\sim 20 \mu\text{K}$ temperature, we still required a fine control of the internal state of the atom (as one of the main conditions for a suitable ultracold platform). In this section we present a set of techniques to achieve such control of the atoms in the ground state via magnetic field manipulation, radio-frequency excitation, atom cooling through evaporation and spin polarization of the sample. Combining all of these techniques we can obtain a polarized sample with temperatures of the order of 100 nK.

3.2.1 Magnetic field interaction with the ground state

The presence of an external magnetic field affects the energy levels of the atom due to the interaction of the magnetic field with the magnetic moment of the atom, this energy shift is known as the *Zeeman effect*. In the case of a relatively weak magnetic field, the interaction Hamiltonian can be treated as a perturbation. In particular, for states with quantum number $J = 1/2$ (i.e. $L = 0$, as in the ground state of ^{39}K : $4S_{1/2}$), a good basis can be defined and the Hamiltonian can be solved analytically leading to the Breit-Rabi formula, which in the case of a large hyperfine splitting (462 MHz for $4S_{1/2}$ in ^{39}K) can be approximated to:

$$\Delta E(B) = g_F m_f \mu_B B, \quad (3.1)$$

with g_f the Landé factor, μ_B the Bohr magneton and $F = J + I$ the good quantum number representing the coupling of the electron total angular momentum (J) and the nuclear spin (I). m_f is the second good quantum number with $m_f = \{F, F - 1, \dots, -F + 1, -F\}$. At zero magnetic field ($\Delta E = 0$) all states are degenerate, and the degeneracy is lifted when an external magnetic field is applied.

We first exploit the Zeeman effect to null all residual magnetic fields in all directions. The main idea is to use a set of compensation coils (placed around the main chamber) to minimize the magnetic field. The procedure to do this is, we scan the magnetic field in each direction independently and for each value we drive all the transitions

from $|F = 1, m_f\rangle$ to $|F = 2, m'_f\rangle$ (This is done with the RF antenna, see next section). Figure 3.9 shows a scan of the magnetic field in the z-direction and the frequency position of all the ground state transitions (scan with the RF antenna, see section 3.2.2). We perform the same measurement in the other two directions and extract the magnetic field required to compensate for the residual magnetic field.

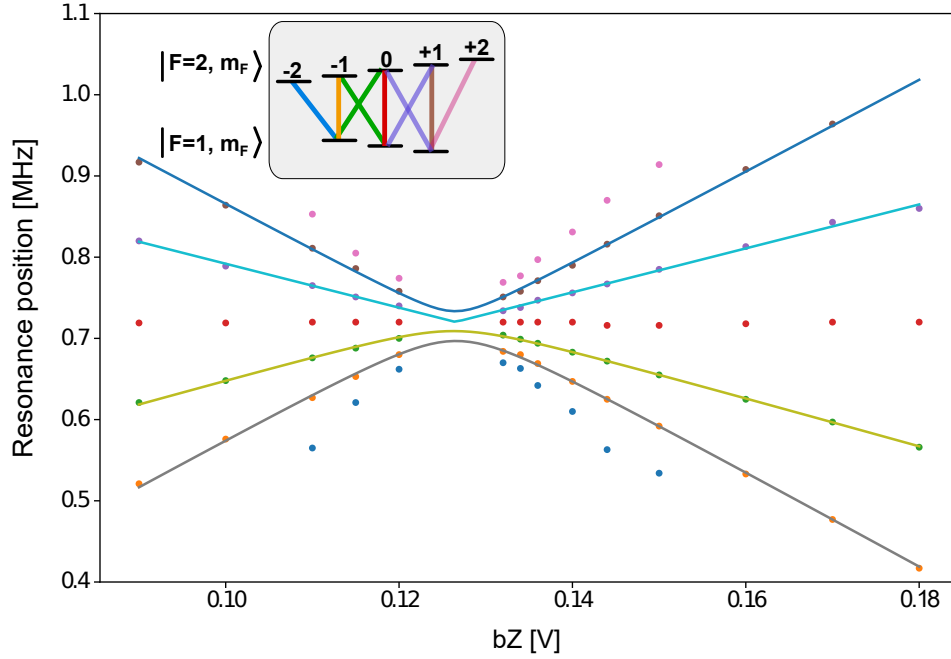


Fig. 3.9.: Magnetic field nulling. Resonance frequency of the ground state m_f transitions as a function of the applied magnetic field in the z-direction. By fitting the resonance splitting, the applied voltage to minimize the magnetic field is found to be 0.126 V.

Having set the external magnetic field to zero, we can now apply a small field in one of the directions to define the quantization axis and resolve the m_F states in the ground state of potassium ($4S_{1/2}$). This allow us to address all the different m_f separately. In particular, we use this capability to create a sample with all atoms prepared in one of the $|F = 1, m_f\rangle$ states, which is the starting point of two important procedures in the experiment. The first one is evaporative cooling which requires a particular state preparation in the state $|F = 1, m_f = -1\rangle$ to enhance the elastic collisions (see section 3.2.3). The second procedure concerns the Rydberg dressed atomic clock detailed in chapter 6, where the sample needs to be polarized in the $m_F = 0$ state which is in first order insensitive to the magnetic field, as we can see in figure 3.9.

3.2.2 Ground state control

For the purpose of driving the hyperfine ground state transition in ^{39}K (462 MHz splitting, see figure 3.2), we included a RF antenna in our setup. This is made of a coil wrapped around the inside-vacuum lens holder (shown in figure 3.1). The antenna driving frequency is controlled via a DDS (Direct Digital Synthesis) AD9914 from Analog devices⁸. This is a frequency synthesizer based on a reference clock with a fixed frequency, whose signal is supplied by a 10 MHz Rubidium frequency standard⁹, and is further multiply by 250 by the DDS to produce a clock speed of 2.5 GHz.

In order to control the DDS an Arduino microprocessor¹⁰ is used, which based on parallel communication manipulates the DDS to send the right frequency. The whole module is handled by the experimental control (see section above 3.1.4), with a program created in Professor Jochim's group, and further modified and implemented in our structural main program described within this thesis. The module is designed to change the driving frequency of the antenna to a single value, different values at different times, or a ramp in order to sweep the frequency. Those settings are loaded in the form of a list at the beginning of each sequence into the Arduino. During the sequence a trigger signal is sent (through the logic box) every time the next setting in the list needs to be activated. The Arduino receives the trigger and communicate the new settings to the DDS.

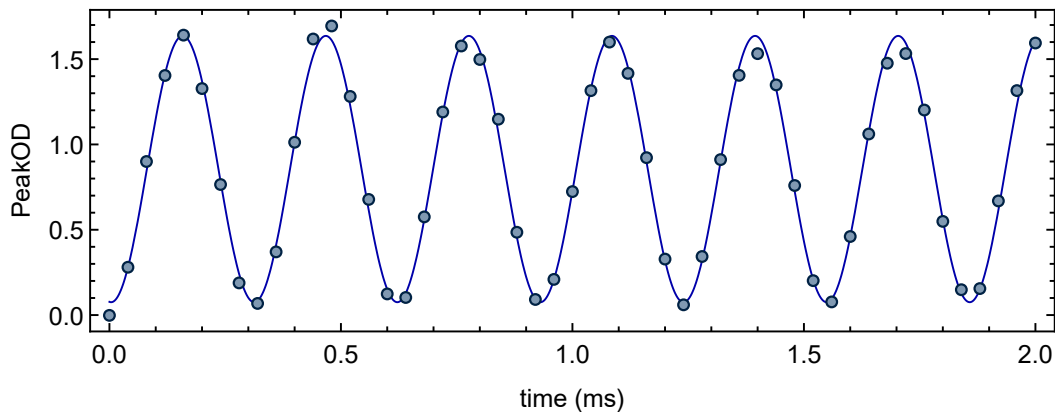


Fig. 3.10.: Rabi oscillations between the $|F = 1, m_f = 0\rangle$ and $|F = 2, m_f = 0\rangle$ states. Measurement of the atom population in the $|F = 2, m_f = 0\rangle$ state as a function of the pulse length of the RF field. The Rabi frequency is extracted from the fit $\Omega_{RF}/2\pi = 3.2$ KHz.

Rabi oscillations between the two hyperfine states. To characterize the control over the ground states, we start with all atoms in $|F = 1, m_f\rangle$ and identify the

⁸<https://www.analog.com/media/en/technical-documentation/data-sheets/ad9914.pdf>

⁹FS725 from Stanford Research Systems

¹⁰Ref: Arduino due

$|F = 1, m_f = 0\rangle \rightarrow |F = 2, m_f = 0\rangle$ transition (the one used for the Rydberg-dressed interferometer in chapter 6), as shown in figure 3.9. We measure the population oscillation between these two states by measuring the atoms in $|F = 2, m_f = 0\rangle$ as a function of the RF pulse length. Figure 3.10 shows the Rabi oscillation between the two involved states, from where we can fit the RF Rabi frequency to $\Omega_{RF}/2\pi = 3.2$ KHz and also determine the pulse length for driving π and $\pi/2$ transitions, for state manipulation.

In order to determine the exact transition frequency of the hyperfine ground state we perform a π pulse (that on resonance should transfer all the atoms to the $|F = 2, m_f = 0\rangle$ state) for different frequencies around the transition. The result is presented in figure 3.11, from this measurement we can determine the center frequency by fitting a *Sinc* function, which is the Fourier transform of the squared π pulse we apply.

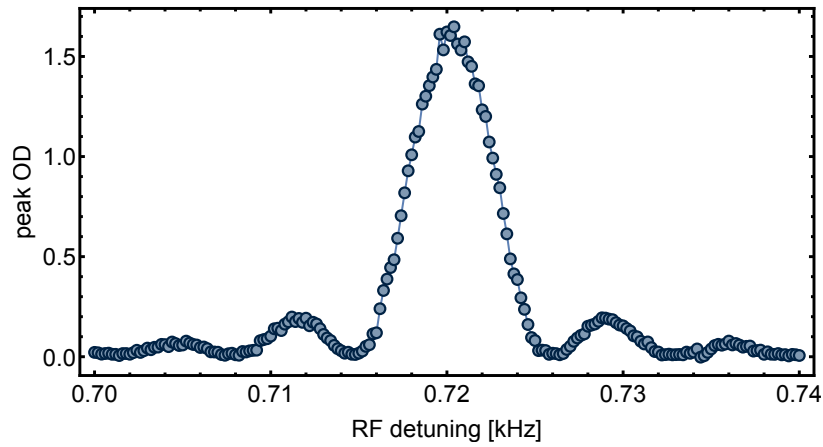


Fig. 3.11.: Frequency determination of the $|F = 1, m_f = 0\rangle$ to $|F = 2, m_f = 0\rangle$ transition. RF frequency scan where we measure the peak optical density as a function of the RF frequency after a π pulse is applied. The result presents a Sinc function behavior due to the square RF pulse applied.

3.2.3 Evaporative cooling

Evaporative cooling is a well developed method in ultracold atoms to reduced the kinetic energy of the atoms while keeping relatively high densities. Its principle is based on the reduction of the trapping potential (either magnetic or optic) to allow particles with higher kinetic energy to leave the trap. After the hot atoms leave and due to thermalization through collisions the center kinetic energy (therefore the temperature) of the atomic cloud is reduced.

One of the key features in evaporative cooling is thermalization, which occurs

through elastic collisions (where there is not change of the internal states of the particles involved), that redistribute the kinetic energy among the atoms. In order to have an effective cooling, it is necessary to enhance those collisions, either by increasing the atom density or by the well known Feshbach resonances [185].

A Feshbach resonance corresponds to the resonant coupling of a pair of colliding atoms with a molecular state which is close energetically. The scattering properties of those atoms at typical ultracold temperatures can be describe in terms of lower partial waves (s-wave scattering).

In the case of potassium 39 eight resonances have been experimentally measured [186] and some more predicted theoretically [176]). We infer from those values that for magnetic fields $B < 300$, the Feshbach resonances are very narrow for m_f values of 0 and +1, which would require a magnetic field control below a Gauss to adjust the collisional rate. On the other hand, the collisions between m_f states -1 are some tens of Gauss broad and therefore easier to manipulate and less sensitive to magnetic field fluctuations, which is why we decide to prepare the atoms in $|4S_{1/2}, F = 1, m_f = -1\rangle$.

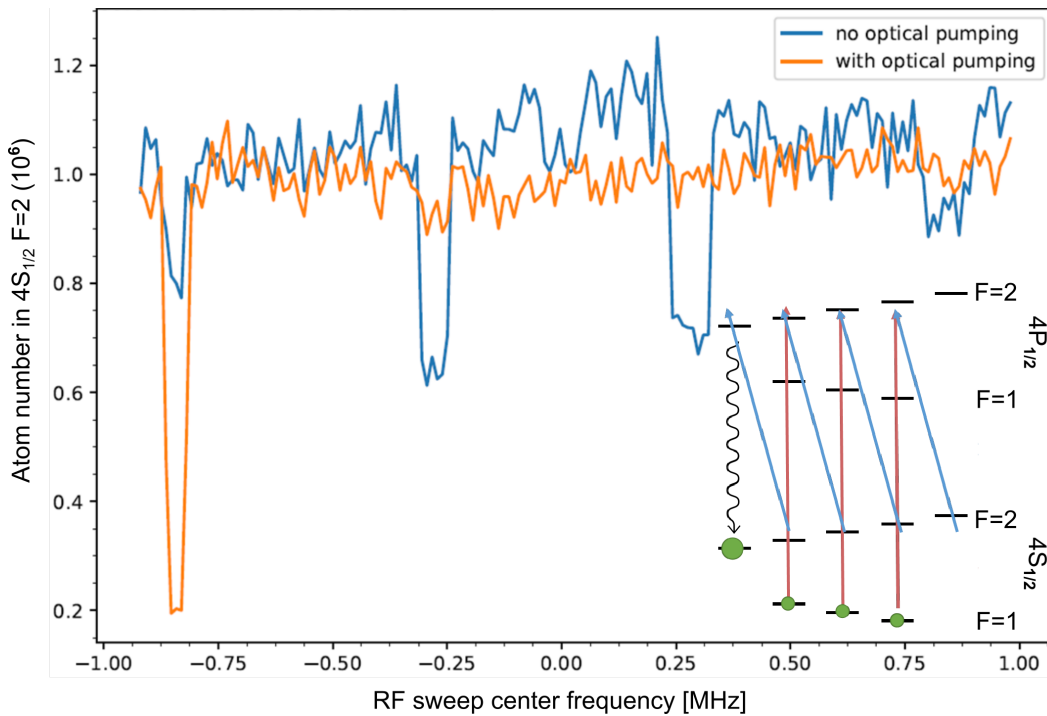


Fig. 3.12.: Population transfer efficiency to the $|F = 2, m_f = -2\rangle$ state. The atoms number in $F = 2$ is measured as a function of the Rf sweep frequency for two cases: with (orange) and without (blue) population transfer. In the polarized sample case it is clear that only the transition $|F = 2, m_f = -2\rangle \rightarrow |F = 1, m_f = -1\rangle$ is addressed. The sub-figure shows the population transfer scheme after preparing the atoms in the $|4S_{1/2}, F = 1\rangle$. A cooler and a repumper beam to the $D1$ transition are used to transfer the atoms to the $|F = 2, m_f = -2\rangle$.

State preparation for evaporation. We start with all the atoms in the $|4S_{1/2}, F = 1\rangle$ equally distributed over the m_f states. This initial state can be easily achieved by using only the cooling light of the $D2$ transition that will drive the atoms out of the $|F = 2, m_f\rangle$ states until they all accumulate in $|F = 1, m_f\rangle$. Right after, the repumper light for the $D1$ transition is turned on, as well as the cooling light which is σ polarized. The second beam helps to accumulate all atoms in the $|F = 2, m_f = -2\rangle$ state, as shown in the sub-figure 3.12. Finally we use a RF frequency sweep to transfer the atoms from $|F = 2, m_f = -2\rangle$ to $|F = 1, m_f = -1\rangle$. This is possible by a Landau-Zener transition through the avoiding crossings of the two states involved.

We characterize the state preparation efficiency by comparing the population transfer from the $|F = 2, m_f\rangle$ states, the results are presented in figure 3.12. The atom number in the $F = 2$ state is measured as a function of the RF sweep frequency, if a transition from $|F = 2, m_f\rangle$ to $|F = 1, m'_f\rangle$ is resonant, some population will be transfer to $|F = 1, m'_f\rangle$ and a deep in the measurement should be observed. We clearly measure a distributions of atoms over all m_f states without any state preparation (blue data). Using this optical transfer technique (sketched in subfigure 3.12), we accumulate about 95% of the population in the $|F = 2, m_f = -2\rangle$ state.

After polarizing the sample, we set the appropriate magnetic field to enhance collisions, and proceed to cool the atoms. The evaporation is done in three steps, reducing the ODT power in optimized time frame based on the atom temperature and density. At the end of the evaporation sequence we obtain densities of $\sim 10^{12}\text{cm}^{-3}$ in a trap depth of $\sim 50\mu\text{K}$ with temperatures down to 50nK temperature. This achievement of evaporative cooling has been attained in the last upgrade of our experimental setup and therefore was not used during the experiments shown in chapter 5 and 6. Nevertheless reducing the thermal motion of atoms is key for future experiments as it is discussed in the conclusion chapter 7.

3.2.4 Spin polarization

In order to perform the measurements related to the Rydberg-dressed atomic clock, we require spin polarize the atoms such that all of them are trapped in the ground state $|0\rangle = |4S_{1/2}, F = 1, m_F = 0\rangle$. We have chosen this specific state to be able to drive magnetically insensitive (see figure 3.9) Rabi pulses between the $|0\rangle$ state and the $|1\rangle = |4S_{1/2}, F = 2, m_F = 0\rangle$, this assures at least in first order that the transition frequency is not affected by magnetic field distributions. To achieve spin polarization, we mainly combine the cooling and trapping beams in the MOT (see section Figure 3.1.2) to distribute the atoms in one of the ground states or to resonantly expelled them from the trap. We also use the ground state manipulation through the RF antenna (section section 3.2.2) in order to drive specific

m_f transitions between the hyperfine ground states. The exact sequence we perform for spin polarizing the sample is based on [187] and sketched in figure 3.13.

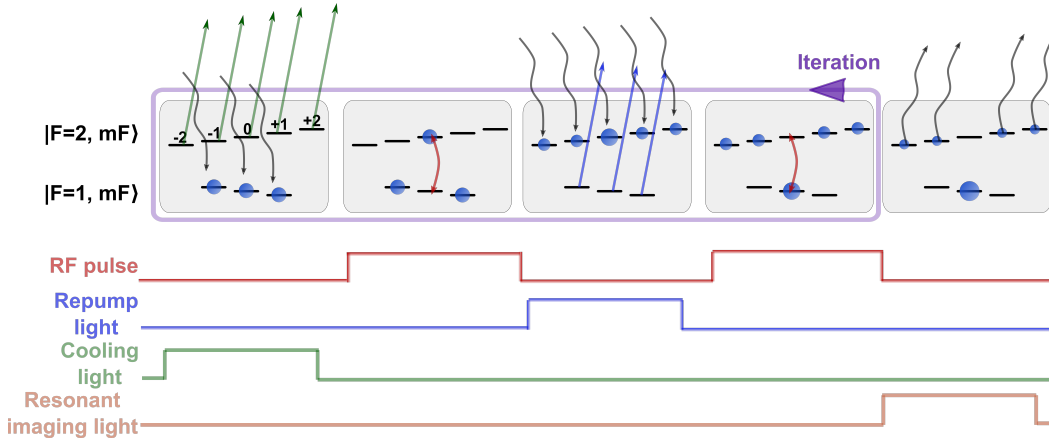


Fig. 3.13.: Spin polarization sequence. We start with all atoms distributed in the $|4S_{1/2}, F = 1\rangle$ state. An RF pulse is used to transfer the atoms from the $|0\rangle$ state to the $|1\rangle$ state. By means of the repumping beam we transfer the rest of the population in $F = 1$ to $F = 2$ redistributing the atoms over all five m_F states. The atoms accumulated in the $|1\rangle$ state are afterwards transferred via a RF π pulse back to the $|0\rangle$. Up to here the sequence can be repeated to accumulate more atoms in $|0\rangle$. After 3 repetitions a resonant pulse is applied to atoms in the $|4S_{1/2}, F = 2\rangle$ state to remove them, resulting in a pure sample with all the atoms in the $|0\rangle$ state.

We start by keeping the cooling beam on for few milliseconds to assure that all the atoms are pumped to the manifold of the $|F = 1, m_f\rangle$ state. A $\pi/2$ RF pulse is applied immediately after, which brings all the atoms in the state $|0\rangle$ to $|1\rangle$. This step in principle should pump a third of the initial population in $|F = 1, m_f\rangle$ into the $|1\rangle$ state, assuming that the atoms are equally distributed over the manifold. As a third step of the polarization process we transfer the remaining atoms in $|F = 1, m_f\rangle$ to the $|F = 2, m_f\rangle$ state using the repump beam. Since we expect to redistribute the amount of atoms equally over the m_F states, the population in the $|1\rangle$ state should increase. As a final step we apply a second $\pi/2$ pulse to bring back the atoms from $|1\rangle$ to $|0\rangle$. The sequence is repeated a couple of times to increase the accumulation of atoms in the $|0\rangle$ state, in our case we iterate this sequence only 3 times, since we do not measure a clearly improvement after the third repetition. After the iterations we finally apply a resonant pulse, the imaging beam on resonance with the transition $|4P_{3/2}, F = 3\rangle$, to get rid of the remaining atoms in the $|4S_{1/2}, F = 2, m_f\rangle$ states.

Spin polarization efficiency. We quantify the sample purity after the spin polarization technique is applied by performing spectroscopy on the $|F = 1, m_f\rangle \rightarrow |F = 2, m'_f\rangle$ transitions. Figure 3.14 shows the population distribution as a function of the RF frequency, comparing before and after the sample is spin polarized (a) and (b) respectively). In the case of no spin polarization, we identify all transitions

$|F = 1, m_f\rangle \rightarrow |F = 2, m'_f\rangle$ with $m'_f = m_f, m_f \pm 1$, with similar population distribution over all the transitions. The measurement is performed only for frequencies below the $|0\rangle \rightarrow |1\rangle$ transition but the results are mirrored for higher frequencies. After having performed the spin polarization sequence the transitions that do not involve the state $|F = 1, m_f = 0\rangle$ are noticeably reduced, almost eliminated, as shown in figure 3.14(b), where we expect the sample purity to be larger than 90%. We additionally observe an approximately 10% increase in the population transferred for $|0\rangle \rightarrow |1\rangle$ this corresponds to the accumulation of atoms in $|0\rangle$ through the iterations in the spin polarization sequence. On the other hand we observe that the second peak from right to left in figure 3.14(b) is reduced to almost a half, this is because the contribution from the transition $|F = 1, m_f = -1\rangle \rightarrow |F = 2, m_f = 0\rangle$ is negligible since most of the atoms are in the $|F = 1, m_f = 0\rangle$ state.

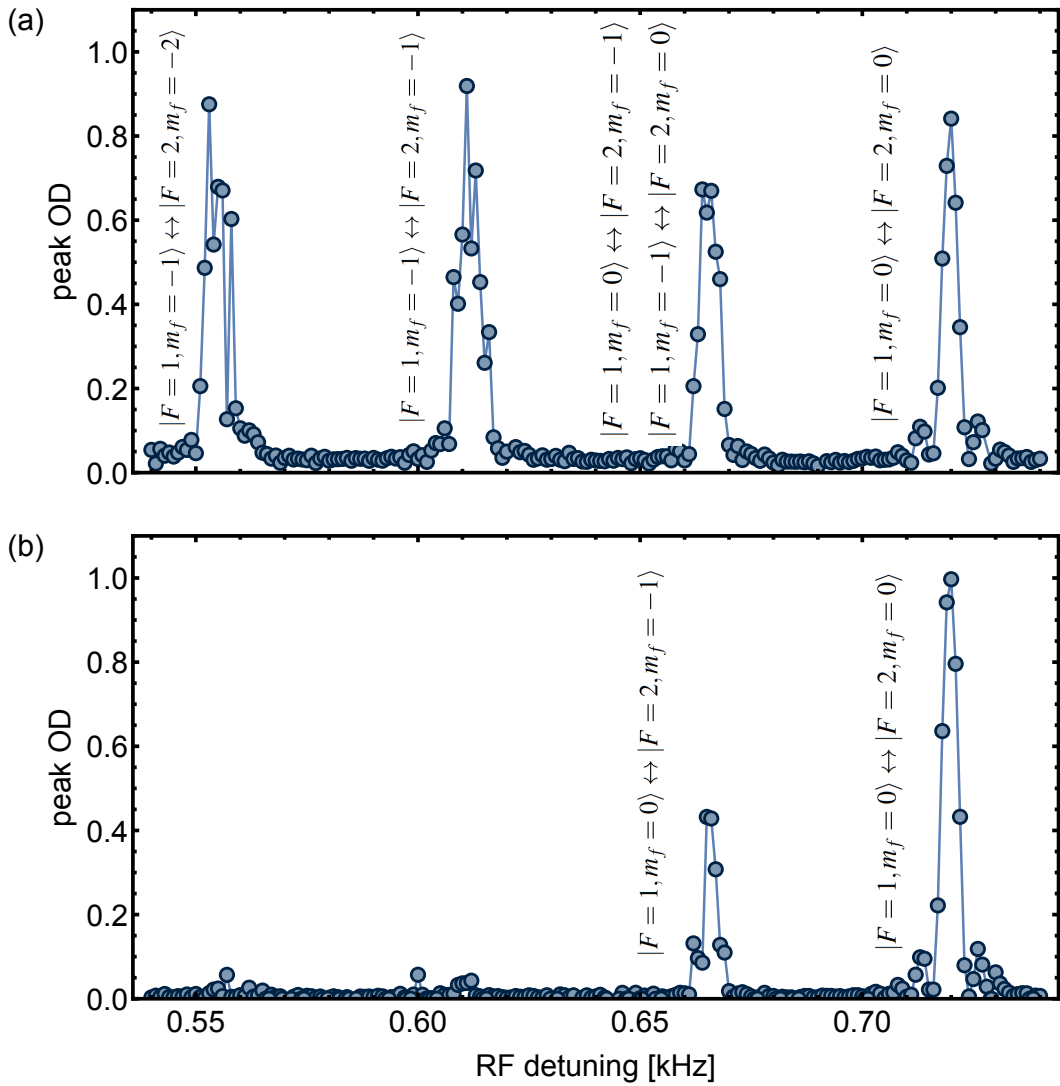


Fig. 3.14.: **Spin polarization efficiency.** Peak optical density as a function of the RF driving frequency. (a) Population distribution of the different transitions before the spin polarization technique is applied. (b) Population distribution of the different transitions after spin polarizing the sample.

3.2.5 Perspective for the ultracold atom platform

The new ultracold atom platform for potassium presented in this chapter is a compact design that allows for manipulation of the atoms in terms of their ground state, spatial confinement and temperature. This includes a well isolated vacuum apparatus (pressure $\sim 10^{-10}$ mbar) and a versatile laser system to trap two different isotopes of potassium (^{39}K and ^{40}K). We implemented the technique of gray molasses cooling and with it achieved temperatures down to $20\mu\text{K}$ (far below the Doppler temperature), making it possible to directly load an optical trap, where all the experiments for this thesis take place. In a later experimental update we could go to even lower temperatures ~ 50 nK by means of evaporative cooling, which combined with the flexibility in the trap geometry paves the way for future studies (see conclusion chapter 7). Furthermore we proved to be able to control different internal degrees of freedom of the particles, using a set of techniques, e.g. magnetic field nulling, radio-frequency state transfer and optical pumping. Moreover, the automation through an experimental control program combined with the good stability of the experimental conditions allow for reproducible experiments and automatic data collection.

The construction of a highly controllable ultracold potassium experiment is the building block for the experiments we want to perform with a Rydberg platform. The second step is to be able to create and control Rydberg atoms, in the next chapter a full description and characterization of the laser system for Rydberg excitation is presented. These together will allow us to create a platform for studying non-equilibrium phenomena based on the driven-dissipative behavior of the Rydberg system.

A versatile laser system for Rydberg excitation

We have seen in chapter 2 the advantages of Rydberg dressing regarding longer decay times that will allow to study the dynamics of the long-range interacting system. In particular we studied the different strengths and weaknesses of one- and two-photon Rydberg excitation, while the former avoids the decay and dephasing of the intermediate state, the second scheme offers more tunability through a larger parameter set and an optimized regime where the interaction is large while the decay is kept low. Based on these results, we have built a versatile laser system, which is able to address both excitation schemes. In this chapter we present the complete laser setup, including its characterization regarding output power, tunability and laser noise, and we also show related experiments with ultracold atoms to further characterize the laser system. This chapter is partially based on the publication "Versatile, high-power 460 nm laser system for Rydberg excitation of ultracold potassium"[188].

The chapter starts by presenting the laser system that can be used for either single or two-photon Rydberg excitation. We include a general introduction on the laser system, the main components and how they work together to achieve high laser standards. The system is characterized first for the two-photon excitation scheme, including laser noise measurements, frequency stability and spectroscopy of highly excited Rydberg atoms. In the last part of this chapter we present the characterization of the single-photon excitation laser focused on the intensity and frequency noise, and additional experiments performed with Rydberg atoms to measure directly the atom-light interaction response. This laser system combined with the ultracold potassium setup allow us to perform the studies on non-equilibrium phenomena (see chapter 5) and on coherence properties of a Rydberg ensemble.

4.1 A unique laser system for addressing ns, np and nd Rydberg states

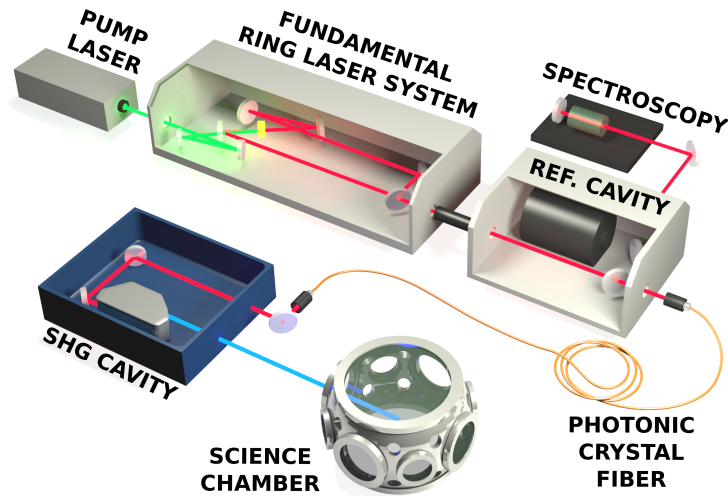


Fig. 4.1.: Main elements of the laser system used for Rydberg excitation. The fundamental frequency light is generated by a laser gain medium (Ti:Sa crystal or dye jet) in a continuous wave ring-laser system, pumped by a solid-state laser system (pump). A small fraction of the produced light is picked off to stabilize the laser frequency to an external reference cavity, while the main power is coupled to a fiber and frequency-doubled by a SHG cavity. Figure adapted from [188]. For further details see text.

As stated previously (see chapter 2) one of the main challenges in Rydberg dressing is to get into a regime with sufficiently strong Rydberg-Rydberg interaction while possible decoherence processes are minimized. In the specific case of two-photon Rydberg excitation one of the main sources of decoherence is due to the coupling to a short-lived intermediate state (in our case $4 P_{3/2}$). This can be overcome by detuning the laser frequency far from the intermediate state, reducing its population and therefore the decay from that state. However, this implies that high intensities for the second step of the excitation are required in order to compensate the reduced dipole transition coupling. On the other hand, one-photon Rydberg excitation avoids this problem since none intermediate state is involved, and therefore the decoherence is limited by other factors such the frequency and intensity noise of the laser system, and the population decay from the Rydberg state, which can be reduced again by a large detuning from resonance, requiring also a high-power excitation laser. Based on these criteria, the ideal laser system not only requires high power, but also narrow linewidth and intensity stability.

This section presents a detailed description of the laser system, which can be adapted for both types of Rydberg excitation schemes. The complete system is composed of four main elements (see figure 4.1). A diode-pumped solid-state laser¹ delivers

¹Spectra-Physics Millennia eV

up to 25 W of light at a wavelength of 532 nm. This laser acts as a incoherent source to generate the fundamental light, therefore its linewidth is not relevant and only power fluctuations can affect the system. The 532 nm laser serves as a pump for either a Titanium-Sapphire (Ti:Sa) crystal or a dye jet in a continuous wave ring-laser system². A small fraction of the produced light is picked off to stabilize the laser frequency to an external reference cavity. The output of the laser is transferred via an optical fiber to another laser table where the frequency doubling cavity and the ultracold atom apparatus is located. This enables additional flexibility for positioning the experiment and we found it to be more efficient than fiber coupling the frequency doubled light which is strongly affected by nonlinear scattering processes in the fiber. To accommodate the high fundamental power we use a single mode polarization maintaining photonic crystal fiber³ with which we achieve an overall fiber coupling efficiency of 50%. After the fiber, the light is coupled into a commercial cavity containing a nonlinear second-harmonic-generation (SHG) crystal. Depending on the wavelength of the seeding light (912 nm or 572 nm), we use different frequency-doubling cavities with its corresponding tailored SHG crystal.

4.1.1 Generation of the fundamental frequency light

To generate a laser beam with high power either at 456 nm or 286 nm, we start by producing light at half the frequency and then with a SHG cavity we double the frequency. This section concentrates on the laser system part that is designed to generate the fundamental frequency light. Depending on the excitation scheme, we use a Ti:Sa crystal or a dye jet to produce the fundamental light (912 nm or 572 nm respectively). The main components used for creating the fundamental light are shown in figure 4.2, in order to change from one excitation scheme to the other, we only need to change the gain medium and re-arrange a few components inside the ring cavity.

The Sirah system: laser resonator and frequency selection components— In order to amplify further the electromagnetic field generated by the pump laser and the gain medium (Ti:Sa or Dye) a resonator which acts as a feedback loop is required. The length of the resonator determines the electromagnetic wavelength that can be propagated, requiring that the optical length coincides with a multiple of the electromagnetic field wavelength. In practice, the Matisse resonator consists of six mirrors, all of them coated to be highly reflective only within the desired wavelength range, in order to reduce other possible frequencies enhanced by the resonator. Additionally, some opto-mechanical elements are included within the resonator for

²Sirah Lasertechnik Matisse TX/DX

³NKT-photonics LMA-PM-15

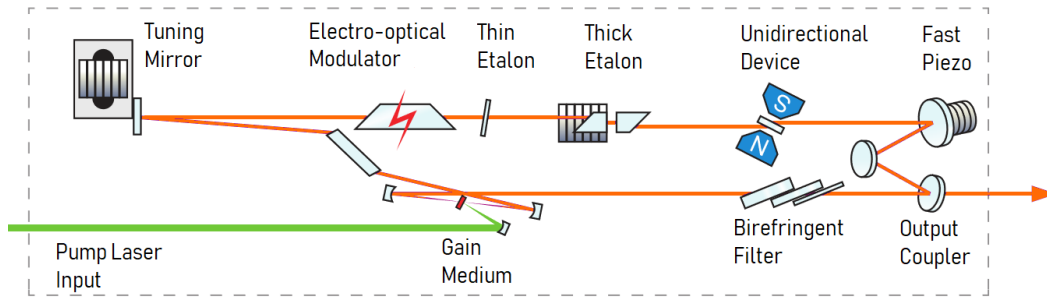


Fig. 4.2.: Schematics of the main laser system used for generating the fundamental frequency light. The pump laser is focused into the gain medium to produce the fundamental light which is enhanced inside a ring cavity. By means of different frequency selective elements (birefringent filter, thin etalon, thick etalon and tuning mirror) the frequency can be narrowed and tuned. Depending on the required fundamental light the medium is changed, i.e. a Ti:Sa crystal is used for 912 nm and a dye jet is required for 572 nm. Figure adapted from Sirah web page: <http://www.sirah.com/laser/cw-ring-lasers/matisse-dx>.

frequency selection, narrowing and stabilization, which will be described below.

In general, an optical resonator has resonant modes at well defined frequencies, with a separation between two adjacent modes of $c/2d$, with c the speed of light and d the resonator length, this is known as the free spectral range (FSR). Furthermore, if the bandwidth of the generated electromagnetic field by the gain medium is much smaller than the FSR of the resonator, it is possible to have single frequency emission by making the center frequency of the medium coincide with one of the modes of the resonator.

In the case where the medium bandwidth is much larger than the FSR of the resonator, a huge number of modes would be involved, enhancing different frequencies from the gain medium. This is the case for our resonator and the gain media used (Ti:Sa and dye), due to the broad band gain it is mandatory to add other components in the resonator to select and narrow the frequency. In this way, one can obtain a single frequency mode laser which is tunable within the gain medium's bandwidth. The different frequency selective components in our system are: a birefringent filter, a thin etalon and a thick etalon, which are explained in the following.

The birefringent filter works as the main broad range tunable element. It narrows down the frequency range of laser modes from a few tens of THz down to several hundreds of GHz. Its general working principle is based on birefringence, which is a property of some crystals such that the refractive index varies depending on the polarization of the incoming electromagnetic field. If a linear polarized component propagates through a birefringent medium, the two polarization components will present different refractive indexes. In this way the total polarization will change while propagating through the medium, since there is a change in the relative phase

between the two components. More specifically, this is used in birefringent filters such that by setting the angle of the crystal a specific bandwidth can be transmitted without losses while the rest will be reflected (lost) at the polarizing surfaces of the filter or at other polarizers placed in the resonator. In order to get a well defined bandwidth, it is usual to include more than one crystal with different widths. This is the case of the birefringent filter used in this resonator, which is made of three crystals where the thinnest is about $300\mu\text{m}$ thick and the ration between the crystals is 1:3:15.

The next frequency selective component is the thin etalon. This is a Fabry Perot etalon, a resonator, that will transmit only a specific wavelength range, depending on the angle of the etalon with respect to the incident light. The allowed wavelengths will correspond to $\lambda_m = 2nd\text{Cos}\theta/m$, with n the refractive index of the etalon, d its thickness, θ the angle related to the incoming field and m an integer mode number. In the Matisse system this is the filter used after the birefringent to further narrow down the frequency spectrum to a few hundreds of MHz. In order to choose the closest mode to the desired wavelength, the angle of the thin etalon is scanned via its mount position which is motor controlled. A photodiode is set to record the reflected intensity such that one can choose the intensity peak closest to the desired wavelength. In order to keep the thin etalon at the correct angle (coinciding with the chosen mode), the intensity reflected from one of the surfaces is monitored and compared to the total laser intensity. Using a control loop the thin etalon is adjusted to keep the ratio between the two intensities constant.

The last element used for frequency selection is called the piezo etalon or thick etalon, which can narrow down the frequency to a few tens of MHz. This is another Fabry-Perot resonator working like the one explained above. In this case the resonator is made out of two prisms separated by an air gap. The corresponding resonator mirrors are the parallel faces of each prism forming the air gap. In order to select the wavelength the gap distance is changed by a piezo actuator which is attached to one of the prisms. Furthermore, to get a stable frequency, the chosen mode is locked by the piezo actuator which is slightly modulated such that the intensity reflected from one of the prisms (modulated) can be used for locking. When the distance modulation is center around the distance that enhances the transmission of the mode, the observed intensity modulation is symmetric, otherwise it is not. Based on this criteria the intensity is monitored and the gap distance is corrected in a feed back loop. This locking scheme is also very useful to keep the right frequency mode when scanning one of the resonator mirrors to get the exact required wavelength.

Frequency stabilization: Reference cavity and ultra-low expansion cavity—By adjusting all frequency selection components one can choose the right transition frequency for Rydberg excitation within a few MHz precision, this is done by a

software that controls the electronics of the different components. However the chosen frequency will quickly drift if the laser system is not stabilized, in our case we use a reference cavity to lock the laser to a precise frequency. The Sirah setup comes with such cavity (sketched in figure 4.3) that can be either locked internally using a photodiode and a electro-optical modulator (EOM) controlled directly by the computer program, or it can be locked by creating an error signal with external electronics and then this signal can be fed into the laser control box. No matter the locking scheme, we require additionally to lock the length of this cavity to another reference, to avoid a long-term frequency drift of about 100 kHz per minute, as shown later in this chapter (see section 4.2.3). To do this, we create an error signal based on a different laser (in our case the 767 nm) and lock the cavity length to it, using the piezo actuator placed between one of the cavity mirrors and the spacer.

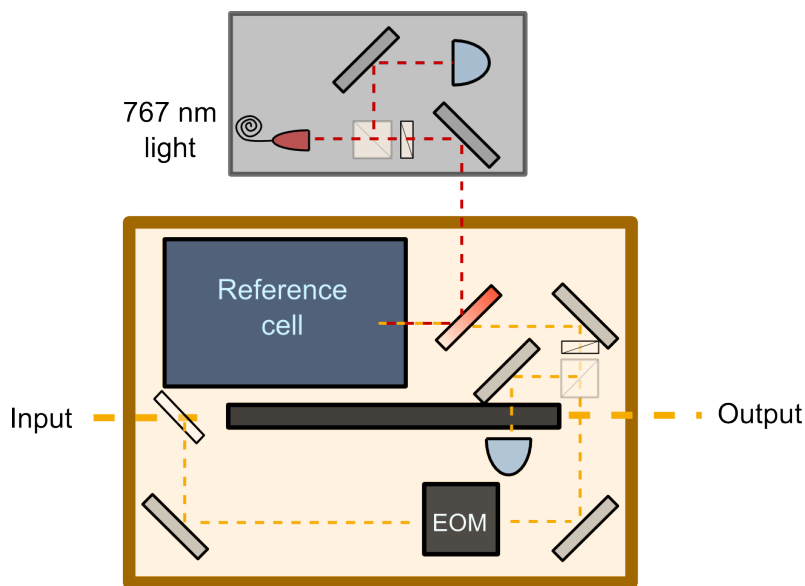


Fig. 4.3.: Scheme of the reference cavity and optical system for frequency stabilization. A small percentage of the input beam is picked off and modulated at 20 MHz by an EOM, creating frequency sidebands. The modulated light goes into the reference cavity and the reflected intensity is measured by a photodiode which, when mixed with the modulation signal, and then filtered, creates the Pound-Drever-Hall error signal used for locking. An extra setup has been designed to lock the cavity length via another stable laser (767 nm).

Since the error signal can be created externally and fed to the laser electronics for the fast piezo to be locked, one can also use a different reference cavity. We also explore this approach by using a ultra-low expansion cavity (ULE)⁴ which is made of two mirrors specially coated for all the different wavelengths we use (912 nm, 767 nm and 572 nm). The cavity mirrors are separated by an ultra-low expansion glass-spacer which is passively stabilized by keeping the cavity system at the temperature which the thermal expansion coefficient is zero. In order to isolate the system from

⁴Stable Laser Systems ATF 6010-4

the environment, the cavity is placed inside a vacuum housing with temperature stabilization. A detailed characterization of the ULE cavity, including the finesse for the different wavelengths, can be found in [189]. We compare both cavities to lock the dye laser system (see section 4.3.1) but concluded that no matter how good the finesse is for the ULE cavity the frequency narrowing is not better, and other factors had probably a stronger influence in the laser frequency noise like the dye temperature.

4.1.2 Frequency doubling: Second harmonic generation

Despite the popularity of solid state lasers, these cannot cover the entire spectrum desired in experiments, from ultra-violet (UV) to infra-red (IR), therefore other types of laser systems are used to cover the frequency spans that are not covered by a typical diode system, specially when high-power is required. In our case we make use of the second harmonic generation technique to double the fundamental frequency in order to obtain the adequate laser light (either 456 nm or 286 nm). This technology is based on a non-linear optic (NLO) crystal which can generate light with double the frequency of the incoming system due to the non-linearity of the crystal [190].

More specifically when monochromatic light propagates through the NLO crystal, the electric field polarizes the medium, creating a wave of polarization density that propagates along the light beam. With high enough intensity light higher order terms in the polarization become relevant, in particular the second order will cause an oscillation in the polarization density with double the electric field frequency. In turn this oscillation will radiate in the form of an electric field with double the frequency of the original incoming field.

In order to achieve efficient frequency conversion the radiated field should oscillate in phase such that at the end face of the crystal constructive interference occur. This can be achieved by using a birefringent crystal such that the propagation velocity of the waves inside the medium can be adjusted to match, typically by adjusting the crystal temperature or the angle between the laser light and the crystal axis. Furthermore the conversion efficiency can be enhanced by placing the NLO crystal inside a resonator which boosts the fundamental laser intensity, generating higher power at double the frequency.

The SHG setup for one- and two-photon excitation—Since the wavelength required for one- or two-photon excitation is very different, we need two separate SHG systems. To generate 456 nm light we use a SHG cavity from Toptica⁵ based on

⁵Toptica SHG pro

a NLO crystal inside a bow-tie resonator, where its length is stabilized with respect to the fundamental laser frequency and phase matching can be adjusted by tuning the crystal temperature. The fundamental light is coupled to the SHG cavity via a photonic crystal fiber⁶ which facilitates the beam mode matching with the resonator.

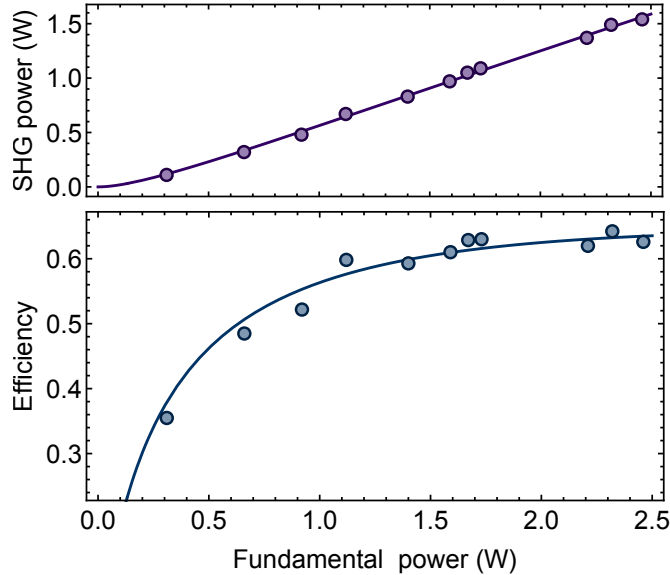


Fig. 4.4.: Performance of the frequency doubling by the second harmonic generation (SHG) for the two-photon excitation. The top panel shows the output power after frequency doubling as a function of the fundamental power at a wavelength of 456 nm (912 nm in the fundamental). The maximum power obtained is 1.5 W for an input power of 2.5 W at 912 nm. The bottom panel shows the doubling efficiency as a function of the fundamental power, showing the non-linearity of the crystal efficiency up to saturation about 60%. The solid lines correspond to a model for the second harmonic generation, see details in the text. Figure adapted from [188].

We have characterized the frequency doubling efficiency of this SHG as a function of the fundamental power (Fig. 4.4). The maximum output power has a quadratic dependence on the fundamental power below approximately 1 W which crosses over to linear scaling at high powers (see top panel in figure 4.4). The crossover coincides with a saturation of the SHG conversion efficiency at around 60% (bottom panel in figure 4.4) resulting in a maximum output power of 1.5 W blue light (for 2.5 W fundamental). In comparable experiments without the photonic crystal fiber we achieved a maximum of 3 W blue light (5 W fundamental), however the fiber coupling efficiency for 456 nm light is much less than 50%, resulting in overall less intensity available. The total output power is substantially more than routinely operated amplified semiconductor diode-based systems [191, 192], which is what we require for Rydberg dressing. We found, we can model the SHG performance by including the power absorbed to generate the second harmonic light as an additional

⁶NKT Photonics LMA-PM-15

loss term in the equations describing the electromagnetic field propagation inside a Fabry-Perot cavity (following Ref. [193]) confirming that we reach close to the optimal operating conditions.

To produce 286 nm light we use a different frequency doubling system: the wave-train⁷ which is based on a BBO (Barium borate) crystal placed inside a triangle-shape ring resonator. The length of the cavity is locked to the incoming fundamental light, including the electronics that allow to automatically re-lock the laser. The crystal is placed on a base that can be rotated manually to adjust the phase matching angle. This crystal is able to generate light over more than 50 nm, making the fundamental light tunability the main restriction for the produced laser frequency.

4.2 Characterization of the two-photon excitation system

In this section we concentrate on the blue laser system (456 nm) used as the second step in the two-photon Rydberg excitation. We characterize the laser tunability, output power, frequency stabilization including frequency noise at short and long time scales, and intensity noise. Additionally we exploit the ultracold atom system to further characterize the stability and tunability of the laser system and Rydberg excitation. Coincidentally, the upper transition (456 nm) in the two-photon excitation scheme corresponds also to the wavelength range used for laser cooling of strontium at 461 nm [194], making this laser useful for applications beyond Rydberg physics, like optical frequency metrology [195, 91] and quantum sensors [196].

4.2.1 Tunability and power

We start by studying the tunability and total output power of the laser system, which is very important for a flexible experimental setup that covers all Rydberg states from $n = 19$ to ionization (between 455 nm and 480 nm). Additionally, the laser power is particularly relevant for Rydberg dressing since the frequency needs to be detuned from resonance to create a weak superposition between the ground and the Rydberg state, and high power has to compensate the small dipole matrix element between the intermediate state and the Rydberg.

We investigate the wavelength tuning range which by varying the Ti:Sa wavelength and adjusting the SHG cavity and the crystal temperature to maximize the output power. Figure 4.5 shows the output power and optimal crystal temperature for phase

⁷Sirah Wavetrain

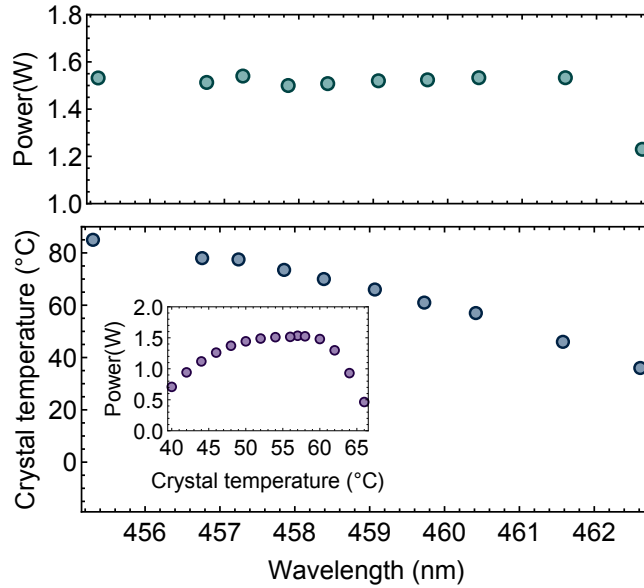


Fig. 4.5.: Wavelength tuning range of the frequency doubled laser spanning from 455 – 463 nm with a nominal output power ≈ 1.5 W (upper panel). For each operating wavelength the optimal crystal temperature for phase matching must be found (lower panel). The inset shows the typical crystal temperature dependence of the output power for a second harmonic wavelength of 460.4 nm. Figure adapted from [188].

matching measured over the wavelength range 455 - 463 nm. A typical measurement of the output power as a function of temperature for a wavelength of 460.4 nm is shown in the inset. The noticeable asymmetry can be explained as a consequence of crystal heating due to extra absorption away from the optimal phase matching condition. As the wavelength is reduced, higher crystal temperatures are required. We measured up to 85 °C (maximum temperature tolerated), which corresponds to a minimum wavelength of 455.2 nm. Additionally, we confirm that an output power of ≈ 1.5 W can be achieved over a big range of wavelengths (Fig. 4.5a), above 463 nm the power starts decreasing. This setup has been used for more than one year with no sign of degradation and only requires minor adjustments from day-to-day when working with a fixed wavelength.

4.2.2 Linewidth and intensity noise

Besides the dephasing caused by the finite lifetime of the Rydberg atoms in the system, the dressing laser can also have a strong influence on the atomic system dephasing. In particular, frequency noise, random fluctuations of the instantaneous frequency, will affect the coherence of the dressing. Additionally, intensity noise has also a strong effect on the dressing since any fluctuation in the laser power changes the Rabi coupling frequency and therefore the Rydberg admixture β . This section focuses on the characterization of both types of noise for the 456 nm laser system.

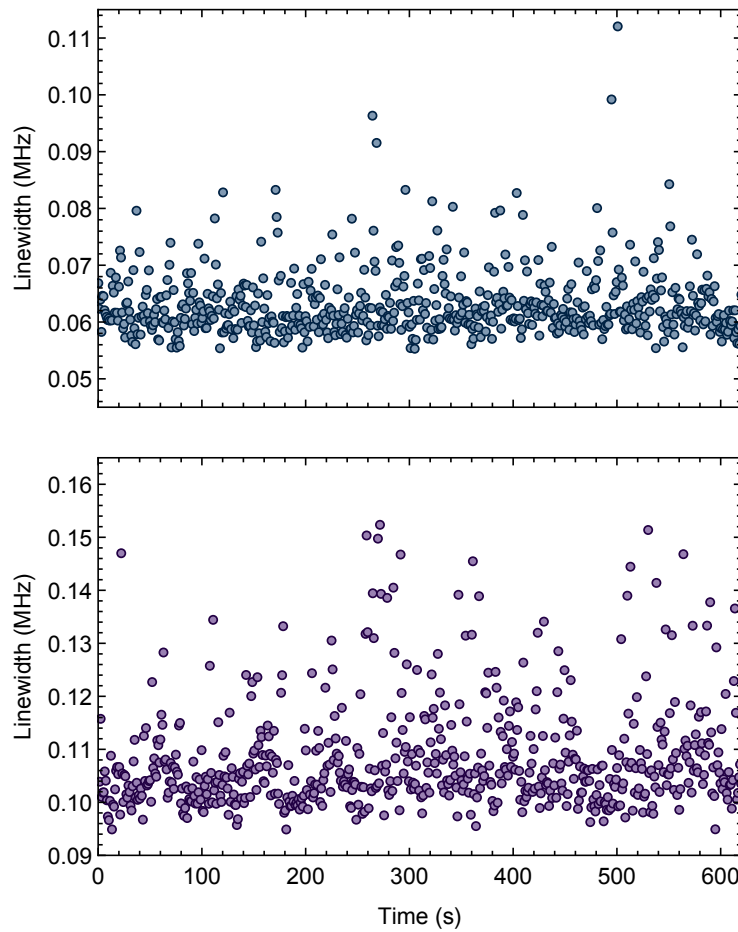


Fig. 4.6.: Linewidth measurement of the fundamental and frequency doubled laser light. The upper panel shows a measurement of the 912 nm laser linewidth as a function of time, with 63 ± 5 kHz linewidth. The bottom panel presents a similar measurement for the frequency doubled light (456 nm), the linewidth: 115 ± 9 kHz.

We start by analyzing the laser frequency short term fluctuations. The 912 nm laser system is locked to the Sirah reference cavity while the frequency doubling cavity is locked to a Pound-Drever Hall signal generated in the cavity with the 912 nm light. For these linewidth measurements we use an optical spectrum analyzer ⁸ which can resolve frequency fluctuations as small as 20 kHz. This analyzer uses a lock-release-measure technique, which converts laser frequency noise into intensity noise by measuring the laser transmission close to the side of a fringe of a Fabry Perot resonance. More precisely the optical cavity of the analyzer record the transmission peaks of the laser light and locks the cavity to one of the sides of a peak, therefore with a release-relock measure a change in the intensity peak can be translated into a fluctuation in frequency.

⁸Sirah Lasertechnik, EagleEye Optical Spectrum Analyzer (OSA)

Figure 4.6 shows a linewidth measurement over time for the fundamental and the frequency doubled laser light. The root-mean-square frequency noise of the blue light is 115 ± 9 kHz, measured within a time window of $7 \mu\text{s}$. The uncertainty is estimated from the root-mean-square deviation of several independent measurements taken over one hour. This is consistent with the Ti:Sa laser noise for which we measure a linewidth of 63 ± 5 kHz (upper panel fig. 4.6). We conclude that the whole laser system may be made spectrally narrower by locking the Ti:Sa to a reference cavity with a higher finesse.

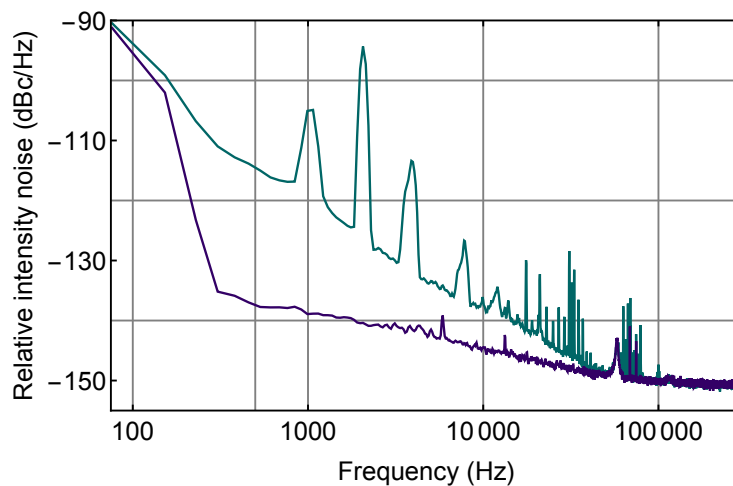


Fig. 4.7.: Relative frequency noise of the 456 nm light within the bandwidth from 75 Hz to 5MHz. The upper curve (green) corresponds to the laser intensity noise while the lower curve (purple) is the intrinsic noise of the photodiode, measured without any incident light. Figure adapted from [188].

In addition to laser frequency noise, it is important to minimize intensity noise which may cause spectral broadening or heating of the atoms due to AC Stark shifts during Rydberg excitation. Using a photo-diode and a spectrum analyzer we measure the relative intensity noise which is shown in Fig. 4.7 (green line). The background noise level is measured without any light incident on the photodiode (purple line). The spectrum exhibits an overall $1/f$ dependence with additional narrow resonances corresponding to different noise sources. For example, we determined that the two main peaks at 1 kHz and 2 kHz originate from the modulation of the fast piezoactuator used to lock the Etalon within the Ti:Sa cavity which could not be further reduced without impacting the frequency stability. Integrating the spectrum over the bandwidth range from 75 Hz to 5 MHz yields a root-mean-square noise level of less than 0.1 percent.

4.2.3 Long-term frequency stability characterization with ultracold ^{39}K

While the reference cavity provides good short term stability, we notice a typical drift of several MHz/hour under typical laboratory conditions. This is largely due to external temperature fluctuations as well as drifts associated with the piezo-controlled mirror used for frequency scanning. To compensate this we chose to actively stabilize the length of the cavity to an absolute frequency reference. For this we use the stable 767 nm laser light with linewidth 120 ± 20 kHz (see section 3), from which we pick off a few milliwatts which is then passed through a double-pass acousto-optical frequency shifter (Brimrose TEF-600-400) and an electro-optical modulator, driven with frequencies of approx 800 MHz and 6 MHz respectively, to generate carrier and sideband components. The radio-frequency signal applied to the frequency shifter is generated by a direct digital synthesizer (DDS) (Analog Devices AD9914) which can be tuned over a wide range. This light is then coupled into the reference cavity to generate an error signal using the Pound-Drever-Hall technique with a feedback bandwidth of approximately 10 Hz. The measured tuning range of the whole system (including the frequency shifter diffraction efficiency) is 700 MHz which is close to the free spectral range of the reference cavity. In a related experiment we have achieved an even wider tuning range and lower power requirements with a different technique using a fiber based EOM⁹.

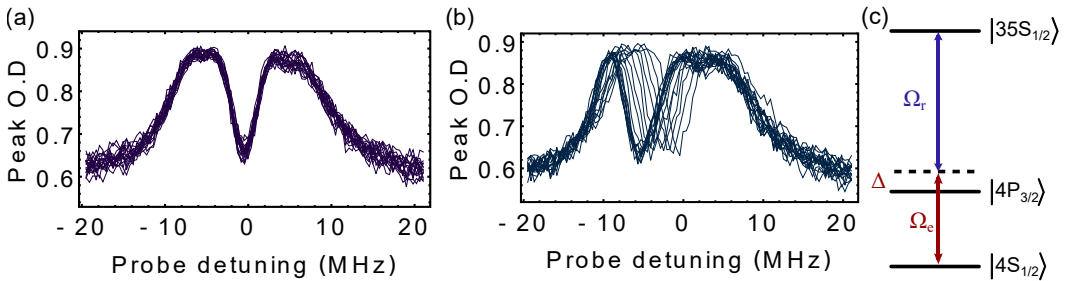


Fig. 4.8.: Frequency drift of the 456 nm laser with and without cavity locking. An electromagnetically induced transparency (EIT) resonance for the $35s_{1/2}$ state of ultracold potassium provides a reference for monitoring the laser frequency stability over 80 minutes. (a) EIT spectra taken with the reference cavity locked to the 767 nm laser. (b) EIT spectra without drift compensation. (c) Level scheme of the two-photon transition under EIT conditions. Figure adapted from [188].

In order to test the long-term frequency stability of the laser we make use of the electromagnetic induced transparency phenomenon explained in chapter 2, section 2.1.3. The ensemble of atoms released from the optical dipole trap are illuminated by two laser fields: the 456 nm laser (coupling field) close to the $4p_{3/2} \rightarrow 35s_{1/2}$ transition and the probe field (767 nm) addressing the $4s_{1/2} \rightarrow 4p_{3/2}$ transition. The coupling field is kept at a fixed frequency while the 767 nm laser is scanned and the

⁹Jenoptik, phase modulator

atoms remaining in the ground state are measured. On two-photon resonance we expect the appearance of a narrow transmission feature which indicates the presence of a long-lived dark state in the system, if the 456 nm drifts in frequency also the narrow transition shifts in frequency.

Figure 4.8a shows a series of scans of the atomic ensemble absorption profile taken over a time period of approximately 80 minutes. The recorded spectra have the characteristic EIT lineshape, exhibiting a clear EIT transmission peak on resonance with a subnatural width (for the probe transition) of approximately 4 MHz (limited by the upper transition Rabi frequency), and with an EIT contrast larger than 80%. This high contrast confirms relatively good coherence of the laser excitation. The high degree of reproducibility of the spectrum over the long measurement time confirms that drifts of the experiment are well controlled. Over 80 minutes the standard deviation of the center position of the EIT feature is $\lesssim 42$ kHz. For comparison we show a second measurement performed with the drift compensation of the reference cavity switched off (Fig. 4.8b). We observe a systematic drift of the position of the EIT resonance as a function of time with a frequency excursion of approximately 6 MHz. The characteristic time scale of the frequency drift is compatible with independent measurements of the temperature fluctuations in the laboratory of the order of 0.5°C.

4.2.4 Two-photon Rydberg spectroscopy

We further explore the laser tunability and addressability of different Rydberg states using the atomic cloud. We start by adjusting the laser to a higher frequency, such that we can excite higher n Rydberg states, close to the 77s transition, which are closer in energy, since $\Delta E \propto n^{-3}$ (see Table 2.1 in section 2). In the experiment we test the wavelength tunability by recording Rydberg excitation spectra in the MOT for a series of principal quantum numbers, by scanning the piezo etalon of the 912 nm laser system without locking it to the reference cavity (i.e. free running mode).

In this case the first excitation step ($4S_{1/2} \rightarrow 4P_{3/2}$ transition) is made by the MOT cooling laser which has a fixed detuning, while the blue laser is focused to a waist of approximately $30 \mu\text{m}$ in the central region of the compressed MOT and has a peak intensity of 100 kW/cm^2 . When the laser is tuned to resonance with a particular Rydberg level we observe a sudden drop in the MOT fluorescence. Therefore, we perform a spectroscopy measurement in which we pulse on the 456 nm laser for a duration of 20 ms before recording the remaining MOT fluorescence level on a CCD camera (exposure time of 2 ms). This sequence is repeated while scanning the frequency of the blue laser. Fig. 4.9 shows the fluorescence as a function of the

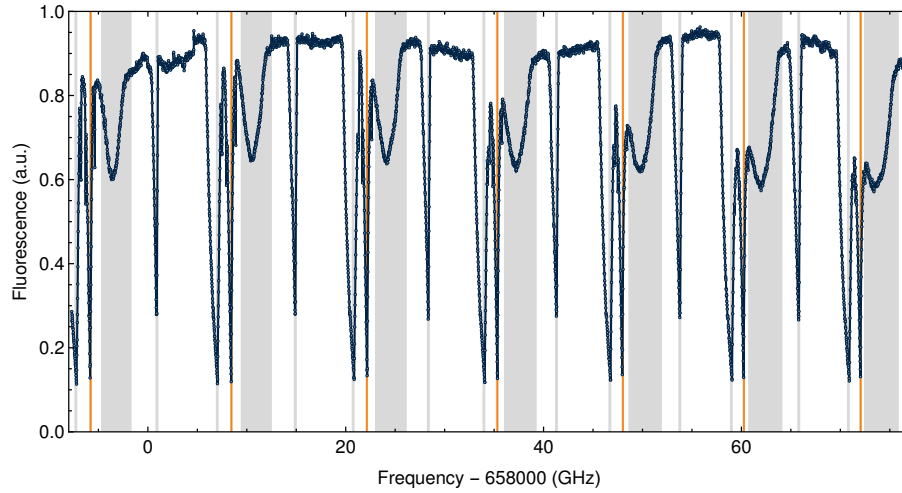


Fig. 4.9.: Rydberg loss spectrum of ultracold ^{39}K atoms in a magneto-optical trap. We identify allowed transitions of ns and nd states (from $n = 77$ to $n = 85$) plus resonances corresponding to np -states and the hydrogenic manifold $l > 2$ which are present due to a residual electric field. The vertical orange and gray lines are the energy position calculated from the quantum defects in ref. [123]. The spectrum is plotted around a frequency that corresponds to a wavelength of 455.6 nm for the second photon in the excitation. Figure adapted from [188].

scanned frequency where every point in the measurement represents a freshly loaded MOT exposed to the excitation laser. The data set consists of 4900 independent frequencies spanning approximately 80 GHz taken over a 3 hour period, which spans the range from the $77d$ to the $85s$ Rydberg states. The full scan exceeds that of the piezo control etalon alone, therefore we record the spectrum in three segments and stitch them together by post-calibrating the frequency axis of the spectrum with the known positions of the ns -states (vertical orange lines) and a precision wavemeter.

We observe a repeated loss spectrum consisting of a series of narrow and broad loss features, some of which correspond to the expected positions of the dipole-allowed ns and nd states (using quantum defects taken from ref. [123]). A zoom-in of the spectrum is shown in Fig. 4.10. Either side of the main resonances we observe narrow features with a minimum spectral width comparable to the size of the steps of ≈ 16 MHz. These sidebands can be explained by the cooler and repumper laser fields which are present in the MOT phase leading to additional resonances with the expected frequency separation of 462 MHz. The spectrum also contains additional broad resonances which coincide closely with the expected positions of np -states and the hydrogenic manifold $l > 2$. We conclude that these otherwise forbidden transitions are visible in our experiment due to a small residual electric field in the vacuum chamber which mixes states with different parity. This is confirmed by a calculation of the Rydberg energy spectrum assuming an electric field of 125 mV/cm (vertical grey bands) which is consistent with the observed width of the resonances

we attribute to the hydrogenic manifolds. However we note that the $l > 2$ feature is systematically shifted from the theoretical expectation, most likely due to the l -dependent mixing of dipole-allowed states.

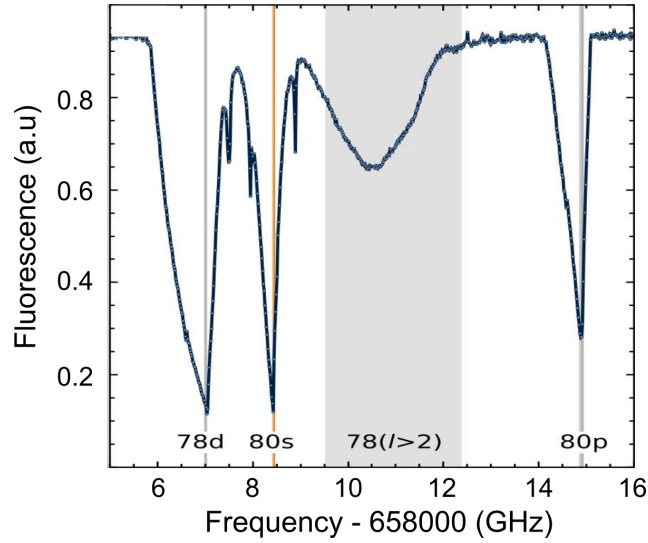


Fig. 4.10.: Zoom in of a group of s -, p -, d - and $l > 2$ -states. The laser system can not only excite the dipole-allowed ns and nd states, but also np and $l > 2$ states due to a small electric field in the experiment. The extra narrow peaks around the broad transitions correspond to the detuned frequencies from the cooler and repumper laser from the MOT. Figure adapted from [188].

The spectral widths of ns , np and nd features are much broader than can be explained by the presence of the small electric field alone and they have a characteristic asymmetric shape (e.g., in fig 4.10 the resonances at 658 007 GHz and 658 015 GHz). We understand this as a consequence of the formation of a positively charged ultracold plasma, after the initial Rydberg excitation, associated with the continuous laser coupling on the millisecond timescale [197, 198]. Furthermore, the asymmetry and different degrees of broadening of the resonances can be explained by the DC polarizabilities of the ns , np and nd states which are all negative, while the polarizability of the nd states is approximately five times larger than for the ns or np states. We point out that the combination of a small electric field and the highly nonlinear loss mechanism provides a novel way to identify and measure Rydberg energy spectra for a wide range of principal quantum numbers and orbital angular momenta with a single laser system.

In this section, we have presented the characterization of a versatile frequency doubled laser system operating at wavelengths around 456 nm. Its key features are very high output power, wide wavelength tuning range, narrow linewidth and low intensity and frequency noise. Using this laser we have demonstrated two photon laser excitation of ultracold potassium atoms under electromagnetically induced transparency and in conditions leading to the formation of an ultracold plasma. Furthermore we have used this laser system to reveal the influence of many-body

correlations in driven-dissipative gases of Rydberg atoms [74] (see chapter 5). With straightforward modifications (e.g., different nonlinear crystals) this laser system can also be applied to different wavelength ranges suitable for a wide variety of atomic species, or other excitation schemes as presented in the next section.

4.3 One-photon excitation system

In this section we explore the different characteristics of the laser system designed to excite Rydberg atoms with a single photon, the wavelength for which is around 286 nm for potassium. For this purpose we have to change the Ti:Sa setup for a dye system, removing the crystal and including a dye jet nozzle plus the realignment of some optical parts (a beam shifter have to be included to adjust the new path inside the ring cavity). Using the same laser ring elements we are able to generate up to 4 W of 572 nm light and by means of the SHG Sirah system (introduced in section 4.1.2) we can get to the desired wavelength (286 nm) with a maximum output power of 300 mW.

Given that the excitation scheme does not involve any intermediate state, frequency and intensity noise are in this case one of the main dephasing mechanisms for Rydberg dressing. We therefore perform a thorough characterization of the mentioned noise and additionally use the atomic system for further studies of the experimental environment and its influence.

4.3.1 Frequency lock approaches and noise measurements

Since frequency stability can be one of the major noise sources in the one-photon excitation scheme, we concentrate a lot of effort on the locking scheme applied to the fundamental laser light (572 nm). In particular lasers based on dyes are not very stable since the fluid requires a constant pressure and temperature to reduce fluctuations in the medium that can generate noise. In general we lock the fundamental laser light to a reference cavity while the SHG cavity is locked separately creating an error signal based on the input light and its own cavity. As explained before, we can either use the reference cavity that belongs to the Sirah system or lock the fundamental light directly to an ultra-low expansion (ULE) cavity.

The first approach we pursue is to lock the fundamental laser light to the external ULE cavity (see section 4.1.1). We pick off a small percentage of the fundamental light into a fiber-EOM¹⁰ whose output goes into the ultra-stable cavity. The fiber-

¹⁰Jenoptik, phase modulator PM594

EOM is used to create and control the error signal, via its modulation with two different frequencies. The first one (20 MHz) is fixed and used to create a Pound-Drever Hall signal to lock the light to the cavity. The second frequency modulation (from a DDS board) is performed in a range between 100-700 MHz to tune the laser frequency by slightly changing the sideband frequency where the laser is locked to. We make use of homebuilt electronics to create the error signal and feed it to the laser control electronics. Figure 4.11 shows the typical error signal and the linewidth measurements over 3.5 minutes, using the same spectrum analyzer and technique presented in section 4.2.2. The observed decrement of the linewidth is due to laser power drift during the measurement. Nevertheless we can measure a mean linewidth of 160 kHz.

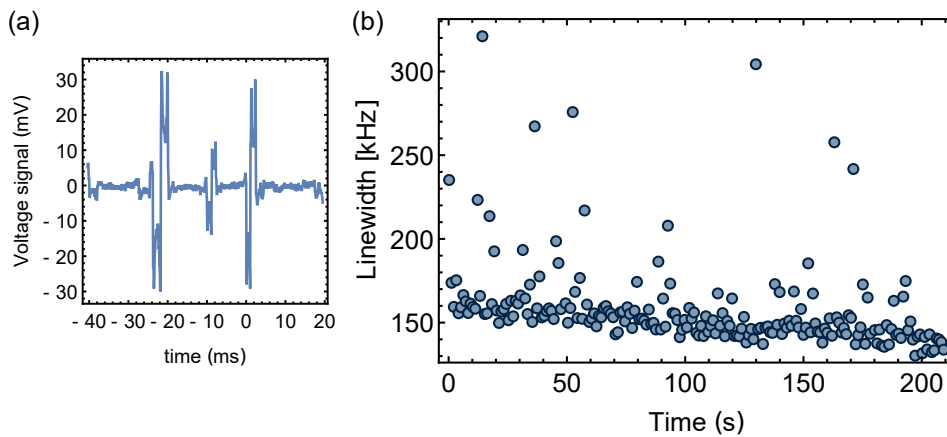


Fig. 4.11.: Linewidth measurement of the 572 nm laser. (a)Error signal used to lock the laser.(b)The fundamental light is locked to the ULE cavity. Using a spectrum analyzer we measure a laser linewidth of 160 kHz over 210 measurements and a time span of 3.5 minutes.

The second locking approach is the same used for the 912 nm laser system, i.e. using the reference cavity of the Sirah system. We lock the laser to the cavity, while the cavity length is locked to the 767 nm laser which is narrowed by the ULE cavity. To lock and tune the frequency we make use again of a fiber EOM modulated with two frequencies to create sidebands in the 767 nm laser light similar to the previous locking scheme. By slightly changing the broadband modulation frequency, the cavity length changes and the fundamental laser follows by also changing its frequency. The measured linewidth with this locking approach is similar to the other technique ~ 180 kHz.

4.3.2 Intensity noise

Continuous wave dye lasers require a high speed flux of the gain medium such that the organic molecules of the dye move away from the pump laser after having

fluoresced. Our laser system has a large reservoir from where the dye is pumped through a nozzle at high speed, which requires constant pumping pressure. Any fluctuation in the pump changes the dye flux and therefore the fluorescence efficiency, causing power fluctuations. Additionally the viscosity of the gain medium can also play an important role in the intensity noise, since the laser efficiency depends upon the amount of molecules that are excited and immediately fluoresce. This is why the temperature of the dye needs to be kept constant at relatively low temperature ($\sim 16^\circ\text{C}$) controlled by the cooling system in the dye reservoir. In this section we study the intensity fluctuations.

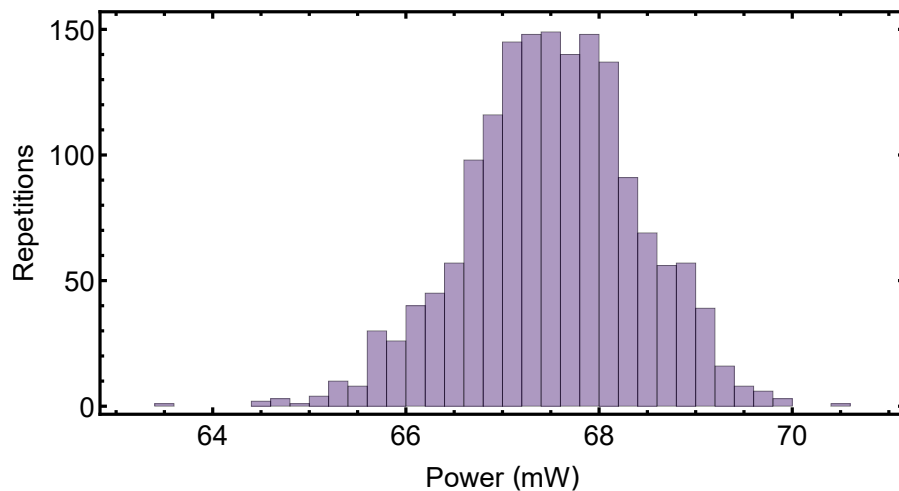


Fig. 4.12.: Laser power histogram of the 286 nm laser system. We read out the laser power with a photodiode over two hours while performing experiments on the cold atoms. The mean measured power is 67.5 mW, with a standard deviation of 0.9 mW.

Figure 4.12 shows a histogram of the laser power taken over 2 hours. A photodiode was installed at the end of the beam path to log the UV power, previously calibrating the photodiode readout voltage with the measured UV power. Using an ADC channel from the logic box we can log the data through our experimental control. We measure a mean power of 67.5 mW with a standard deviation of 0.9 mW. A possible way to reduce the power variation and reduction with time, is by using a feedback loop. One could set a target power lower than the maximum and with a photodiode feed the data to the experimental control which adjusts the power through the corresponding AOM. For short term fluctuations an analog feedback version is required.

4.3.3 Laser and experimental setup characterization with the atomic sample

All the results presented up until here correspond to the one-photon excitation laser characteristics without interacting with the atomic ensemble, we further characterize the laser system by directly measuring the atomic response. It is crucial to perform such studies in order to properly identify the main constraints in the whole system, regarding, for example decoherence. In the next section some spectroscopy characterization is done in the optical dipole trap, to extract the broadening of the transition. There are however other methodologies to characterize a Rydberg enhanced ensemble as shown in chapter 6, where a Rydberg-dressed interferometer proves to be an ideal tool to understand the behavior and mechanisms that cause dephasing and population decay.

Spectroscopy—This part focuses on the first results studying the atom-light interaction between the one-photon excitation laser and the atomic ensemble of potassium atoms. By tuning the laser frequency we can drive the transition $|4S_{1/2}, F = 1, m_f = 0\rangle \rightarrow |39P_{3/2}\rangle$, where we have previously prepared the atomic sample in a spin polarized ground state (see section 3). After preparing the sample in the ODT the excitation laser is turned on for $20 \mu\text{s}$ and an absorption image is taken directly after. Figure 4.13 shows the peak optical density of the absorption image as a function of the laser detuning around the transition resonance. When the atoms are excited to the Rydberg state, they can decay to other states or ionized and lost, therefore they are not measured by the imaging system, translated into a reduction of the peak OD.

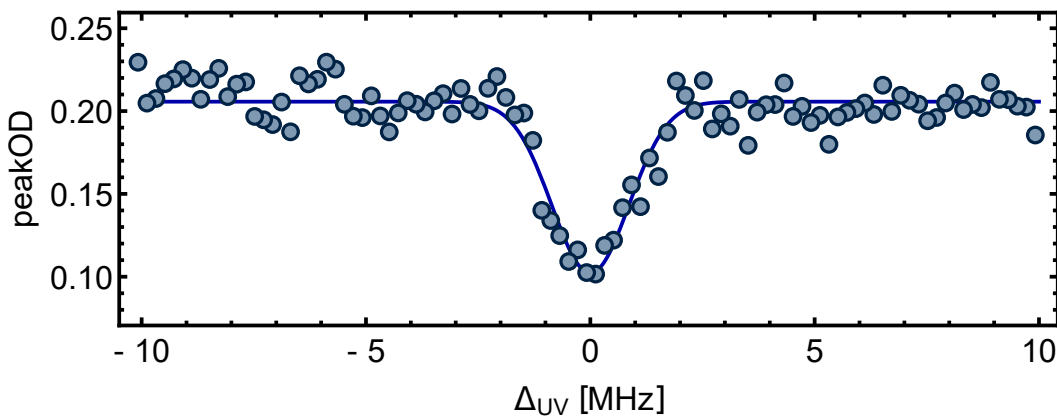


Fig. 4.13.: **One-photon Rydberg spectroscopy.** Atom loss as a function of UV laser detuning. We measure a broadening of 1.7 MHz and a maximum loss rate of 50 kHz on resonance.

Based on the spectrum we measure a spectral linewidth of 1.7 MHz and infer also a maximum loss rate of 50 kHz on resonance. The linewidth measurements presented

before show that the main broadening observe in the spectrum does not come from the laser frequency noise. Possible sources are the atomic thermal distribution, Doppler broadening, the optical dipole trap light shifts and the laser noise, however it is difficult to figure out which effect is dominant in our system. In chapter 6 a detail study on the coherent properties is performed, based on a Rydberg-dressed interferometer, which helps to find out the main decoherence source.

Electric field nulling with Rydberg atoms—Given that Rydberg atoms are very sensitive to small electric fields (see section 2), we exploit this characteristic to analyze the residual electric field close to the atomic cloud. As we have observed in the spectroscopy of high- n Rydberg states (see section 4.2.4), the presence of a small electric field can strongly affect the excitation, mixing states with different parities that allow to excite transitions otherwise forbidden.

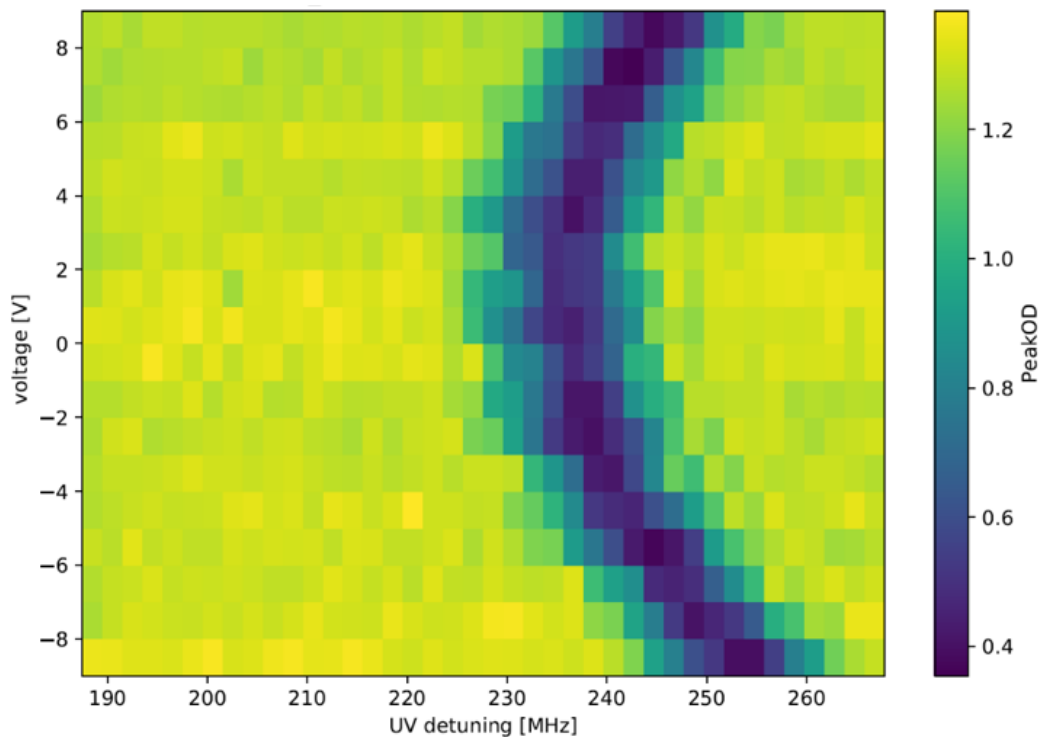


Fig. 4.14.: Spectroscopy of a Rydberg atom in an electric field. Population loss due to the Rydberg state $39P_{3/2}$ is measured as a function of the detuning and an applied external electric field in the horizontal y direction. A minimum in the resonance frequency is measured at 235 MHz for a voltage on the electrodes of 1.5 V.

We perform a spectroscopic measurement of the $39P_{3/2}$ Rydberg state, observing the atomic loss in the ground state as a function of an applied external electric field. We make use of the electrodes in the Rydberg detector (see section 3) to control the electric field near the atomic cloud. The results presented in figure 4.14 show a minimum in the transition frequency, corresponding to the zero of the electric field

in that direction. We perform similar measurements for the other two directions and set the electrode voltages such that the field is canceled in all directions.

This method proves very useful for nulling the stray DC electric field present in the vicinity of the atoms. In chapter 6, we show how a Rydberg-dressed interferometer can be used to measure very precisely small static electric fields, which further proves the utility of the Rydberg platform.

4.3.4 Perspectives for the Rydberg excitation system

In this chapter, we have set up a laser system, adaptable for either one or two-photon Rydberg excitation schemes, making it possible to access a wide variety of different Rydberg states, which can be used to tune the Rydberg interaction strength and anisotropy. The laser system applied to two-photon excitation (456 nm) was characterized in detail, with main characteristics: (i) maximum output power of 1.5 W, (ii) frequency noise of 115(9) kHz and (iii) long term frequency stability better than 42 kHz per hour. We additionally benchmark the laser with atom loss measurements in a MOT to characterize the laser tunability and measure the quantum defects of Rydberg states in potassium with $n > 77$. In the final section we demonstrate the possibility to excite Rydberg atoms via single photon transitions, where the most remarkable characteristic is the relatively high power at 286 nm, up to 300 mW, which is suitable for Rydberg dressing experiments.

Now we have a highly controllable ultracold potassium experiment, shown in chapter 3, that we can combine with the versatile Rydberg excitation laser characterized in this chapter. This experimental platform will allow us to study non-equilibrium phenomena based on the driven-dissipative behavior of the Rydberg system and also to create a technique for characterizing coherence effects in strongly interacting many-body systems.

Exploring non-equilibrium quantum matter with Rydberg atoms

Quantum matter close to thermal equilibrium can be studied and classified using statistical physics. For example experimental and theoretical research on phase transitions have shown that close to the transition point fluctuations with diverging correlations dominate, which is reflected in the scaling of microscopic observables [199]. On the contrary, little is known about systems out-of-equilibrium, their corresponding phase transitions, whether they also show diverging correlations and what to expect from the dynamics in general [200]. Rydberg atoms have proven to be a versatile platform, given their inherent finite lifetime, the system can not be treated as a perfectly isolated ensemble but a dissipative one. This particular characteristic has been used for studying dissipative systems in a variety of experiments [66, 67, 68, 69, 70, 71, 72, 73, 74]. As a first application for the experimental Rydberg platform built within this thesis, we study the non-equilibrium characteristics of our system and its long-term dynamics.

This chapter presents an overview of the non-equilibrium phase structure studies of a Rydberg system and the observation of self-organized criticality in an unstable regime. The discussion presented here is based on two publications: "Uncovering the nonequilibrium phase structure of an open quantum spin system"[74] and "Observation of Self-Organised Criticality in an Ultracold Atomic Gas" [201], discussed in detail in the doctoral thesis [202]. In the first part of this chapter we present the studies on the non-equilibrium phase structure, including a brief theoretical discussion on how to model the Rydberg system, rate loss measurements that present a scaling behavior which can be used to identify the different regimes that depend on the interplay between the driving, decay and interaction. In the second part of the chapter, we further investigate in detail a particular regime where there is a strong competition between driving and dissipation. By looking at the long-term dynamical response of the system, we discover a striking behavior where the system evolves to the same quasi-steady state no matter the initial conditions and also which shows scale invariance.

5.1 Non-equilibrium phase structure

This section presents the main results on the experimental and theoretical investigation of the non-equilibrium characteristics of a well-controlled driven-dissipative quantum Rydberg system governed by the interplay of coherent driving, spontaneous decay and long-range spin-spin interactions due to the Rydberg atoms. For the experiments shown in this section we have made use of the two-photon excitation laser system (see chapter 4) which enables to probe and tune the Rydberg ensemble in different regimes such that driving, dissipation or interactions dominates.

5.1.1 Model for a driven-dissipative Rydberg system

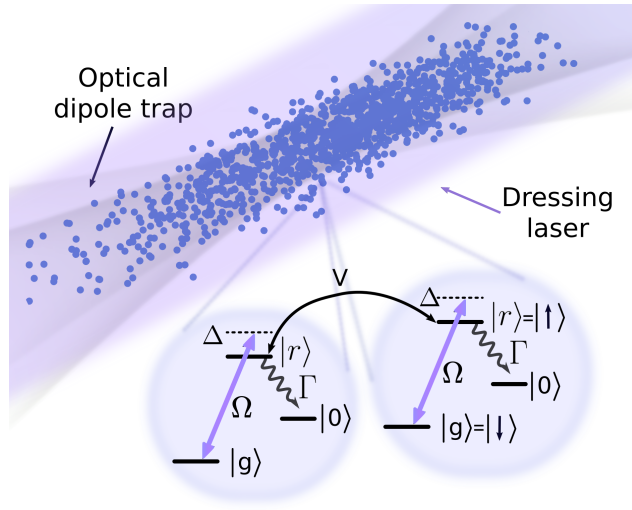


Fig. 5.1: Mapping of the experimental system in a pseudo-spin 1/2 model. The atomic ensemble can be modeled as a spin system, where the ground state $|g\rangle$ correspond to the spin-down $|\downarrow\rangle$ and is coupled to the Rydberg state $|r\rangle$ (via a laser field with Rabi frequency Ω and detuning Δ) which is mapped to the spin up $|\uparrow\rangle$. An additional state $|s\rangle$ represent all the uncoupled states that are populated from the Rydberg decay (with rate Γ) and which no longer take place in the dynamics of the ensemble.

Our system consists of a gas of ultracold atoms driven by laser fields to create a small fraction of short-lived Rydberg excitations. Mapping our system to a pseudo-spin 1/2 system where the ground state is the spin down and the Rydberg state is the spin up (shown in figure 5.1), we can express the Hamiltonian, using the rotating wave approximation, as:

$$\mathcal{H} = \frac{\Omega}{2} \sum_j \sigma_x^j - \frac{\Delta}{2} \sum_j \sigma_z^j + \frac{1}{2} \sum_{j,k \neq j} V_{jk} n^j n^k, \quad (5.1)$$

where σ_x^j, σ_z^j are Pauli spin matrices, $n^j = (\sigma_z^j + 1)/2$ and the indices j, k refer to each spin in the ensemble. In our experiment antiferromagnetic spin-spin interactions

originate from the repulsive van der Waals interactions (V_{jk}) between Rydberg excitations (see chapter 2). The atom-light coupling strength Ω and the detuning from the atomic transition Δ correspond to transverse and longitudinal fields respectively, which can be tuned over a wide range via the probe excitation laser (767 nm in the two-photon Rydberg scheme). The three-level system that corresponds to the two-photon excitation scheme (see fig. 2.1 (a)) used in these experiments can be reduced to an effective two-level system (with driving parameters Ω , Δ , as in fig. 5.1) in the limit that the population in $|e\rangle$ is negligibly small, e.g. $|\Delta_e| \approx |\Delta_r| \gg \Omega_r \gg \Omega_e$. On two-photon resonance, we can describe the coupling from the ground and the Rydberg states by an effective two-photon Rabi frequency $\Omega \approx \frac{\Omega_r}{2|\Delta_r|} \Omega_e$, and an effective detuning $\Delta = \Delta_e + \Delta_r$, where any additional detuning, for example due to the dipole trap, can also be included.

The model up until now resembles the quantum Ising system in transverse and longitudinal fields which has been explored theoretically and experimentally in [156, 203, 204]. However, our system requires to include the spontaneous decay of the Rydberg state which affects the detailed balance condition of equilibrium, having additional effects on the phase structure. That is why, we use a quantum master equation in Lindblad form for the many-body density matrix ρ (in units where $\hbar = 1$), introduced in equation 2.8. The quantum jump operators describing spontaneous decay to a set of states $|0\rangle$ that are not coupled to the laser field anymore, are $L_j = \sqrt{\Gamma} \sigma_-^j$, with the spontaneous decay rate Γ and σ_-^j the lowering operator. We also need to include single spin dephasing, to account for laser phase noise, via additional jump operators of the form $L_j^{\text{de}} = \sqrt{\gamma_{\text{de}}} n^j$, with γ_{de} the dephasing rate. The effective excited state decay rate $\Gamma/2\pi \approx (\Gamma_r + \varepsilon^2 \Gamma_e)/2\pi$ is a combination of the bare Rydberg state decay Γ_r and the residual intermediate state admixture which spontaneously decays with rate Γ_e . Additional loss processes for ns -Rydberg states, e.g., photoionization or penning ionization are estimated to be at least two orders of magnitude smaller [205] and therefore neglected.

The main parameters that compete and define the response of the system are the laser detuning Δ , the coupling Ω , the overall decay Γ and the Rydberg-Rydberg interaction V . Depending on the values of these parameters and which dominates we expect different behavior of the system. For example in the case of large detunings such that $|\Delta| \gg \Omega, \Gamma$ the system can be considered in a weak dressing regime where the atoms acquire a small admixture of the Rydberg component such that $|\psi\rangle \approx |\downarrow\rangle + \frac{\Omega}{2\Delta} |\uparrow\rangle$. In the opposite case when the system is excited on resonance two different regimes are expected. The first one is when dissipation dominates over the driving, i.e. $\Gamma \gg \Omega$. In this case the system once excited decays quickly to the down state, yielding to a classical spin configuration with small fluctuations of spin-up particles, with steady state fraction Ω^2/Γ^2 . In a second situation where the driving and interactions dominate over the decay a high density of interacting

spins associated with a critical regime from the quantum critical point of the Ising model [206, 157] is expected.

5.1.2 Loss rates measurements: key observable

We aim to experimentally explore the non-equilibrium phase structure of our Rydberg platform by analyzing the loss rate of the system in the different parameter regimes. The atoms (about 7.5×10^4) are initially prepared in the $|\downarrow\rangle = |4s_{1/2}, F=2, m_F=2\rangle$ state confined in the optical dipole trap, with peak atomic density $\rho_0 = 5 \times 10^{11} \text{ cm}^{-3}$ and temperature $T = 19.4 \mu\text{K}$. All atoms in the sample are then driven from $|\downarrow\rangle$ to $|\uparrow\rangle = |66s\rangle$ by the two-photon laser excitation system, which has a large detuning ($\sim 80 \text{ MHz}$) from the intermediate state. We can express the laser parameters in terms of the effective two-photon Rabi frequency $\Omega/2\pi$, which we vary from 3 kHz to 100 kHz, by adjusting the 767 nm beam intensity, and the detuning $\Delta/2\pi$ which is also controlled by the same laser and scanned over a range of $\pm 20 \text{ MHz}$. We can additionally control the atom-light interaction time τ by pulsing an AOM for the 767 nm laser while the 456 nm laser is kept on continuously. The strength of the van der Waals interactions of Rydberg pair states $C_6\rho_0^2/2\pi = 65.4 \text{ GHz}$, greatly exceeding all other energy scales such as those associated to single particle driving and decoherence, leading to strong blockade effects (see section 2.2.2). The total effective decay rate of the spin-up states is estimated $\Gamma/2\pi \approx 100 \text{ kHz}$ and primarily attributed to spontaneous emission from the short lived intermediate state, compared to the bare Rydberg state decay rate of $\lesssim 2 \text{ kHz}$. The decay brings the atom either back to the original ground state $|\downarrow\rangle$ or to other states external to the spin-1/2 description that no longer participate in the dynamics, making our system intrinsically out-of-equilibrium.

Loss rate as a probe for an open system—We take advantage of the slow loss of population out of the spin-1/2 subspace to study the behavior of our open Rydberg spin system. Starting with all atoms prepared in the ground state, we suddenly switch on the driving field with fixed values of Ω and Δ and tuned the values for every new experiment in order to map the different regions of the non-equilibrium phase diagram. Following the quench, the system evolves towards states with some Rydberg admixture on a timescale set by the inverse decay rate Γ^{-1} . We probe the (quasi) steady-state established after this short transient period, by letting the system evolve for a time τ that is orders of magnitude longer: between 1.4 ms and 146.5 ms (adapted to Ω). After this time τ we measure the remaining fraction of ground state atoms $P(\tau)/P(0)$, using absorption imaging, and convert the population measurement into a rate by assuming exponential decay $R = -\tau^{-1} \ln[P(\tau)/P(0)]$, extracting the loss rate from only two population measurements. Figure 5.2(a) corroborates that this is a good assumption in the time windows we use, when the

maximum lost fraction is $P(\tau)/P(0) \gtrsim 0.5$. The time resolved data of the population loss for $\Omega/2\pi = 22$ kHz and four different detunings spans all the parameter regimes and shows that the data in the region $t < \tau$ is very well described by exponential decay curves, confirming that the extrapolation of R is a good estimator for the loss rate. For times longer than τ we note some deviations from the pure exponential decay, but this does not affect the results presented in here.

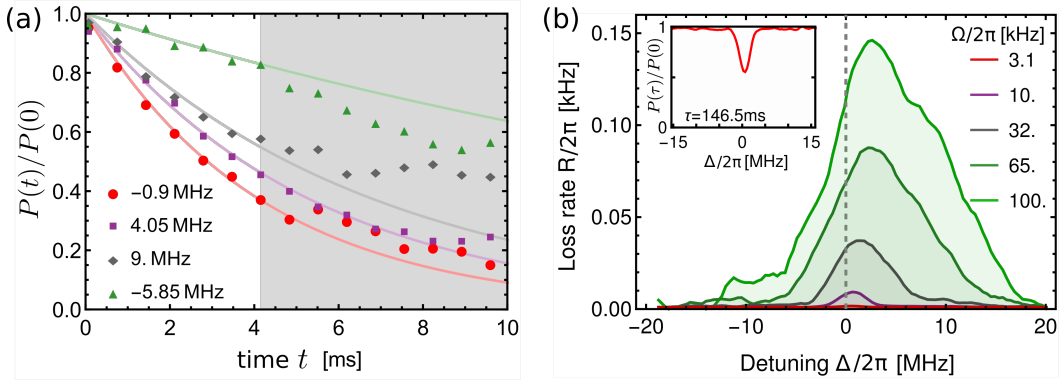


Fig. 5.2.: Studies on loss rate measurements for different Δ and Ω . (a) Time resolved measurements of the atomic fraction remaining in the ground state after an excitation pulse of varying duration t . The Rabi frequency is fixed to $\Omega/2\pi = 22$ kHz, while four different detunings are used for these measurements. The boundary between the white and grey backgrounds marks the waiting time τ used in all experiments for this value of Ω . (b) Measured loss rates as a function of detuning Δ for various driving field strengths Ω . As Ω is increased the spectra become asymmetric and broaden due to strong and repulsive Rydberg-Rydberg interactions. Inset: Fraction of atoms $P(\tau)/P(0)$ remaining in $|\downarrow\rangle$ for the smallest driving field strength $\Omega/2\pi = 3.1$ kHz. Figure adapted from [74].

Furthermore, we verify that the loss rate is indeed sensitive to the many-body state of the system, by measuring its dependence on the driving strength and detuning (Fig. 5.2). For the smallest driving Ω (3.1 kHz) we observe an approximately symmetric Gaussian lineshape with a full width half maximum of 3 MHz [Fig. 5.2b.(inset)]. This symmetry is expected due to the small driving amplitudes, which only allows a small density of Rydberg excitations making the atomic system effectively non-interacting. We observe an increasing asymmetry as Ω is increased, which is a clear indication that the strong repulsive van der Waals interactions between Rydberg n_s states dominate the dynamics, which has been observed in previous experiments with short excitation dynamics [161, 71].

5.1.3 Observation of scaling laws and phase diagram of the non-equilibrium system

We further investigate the quasi-steady state of the system by studying the loss rate as a function of the driving Ω for different detuning regimes (resonant, intermediate detuned and far off-resonant). With such a measurement we expect to see some evidence of the competition between the driving, dissipation and interaction. Figure 5.3 shows the results where we plot the loss rate vs the driving on a log-log scale and observe striking linear behaviors with relatively clear transitions. We show that the data can be empirically described by multiple power-laws $R \propto \Omega^\alpha$, each spanning one or more orders of magnitude in R and Ω (shaded lines).

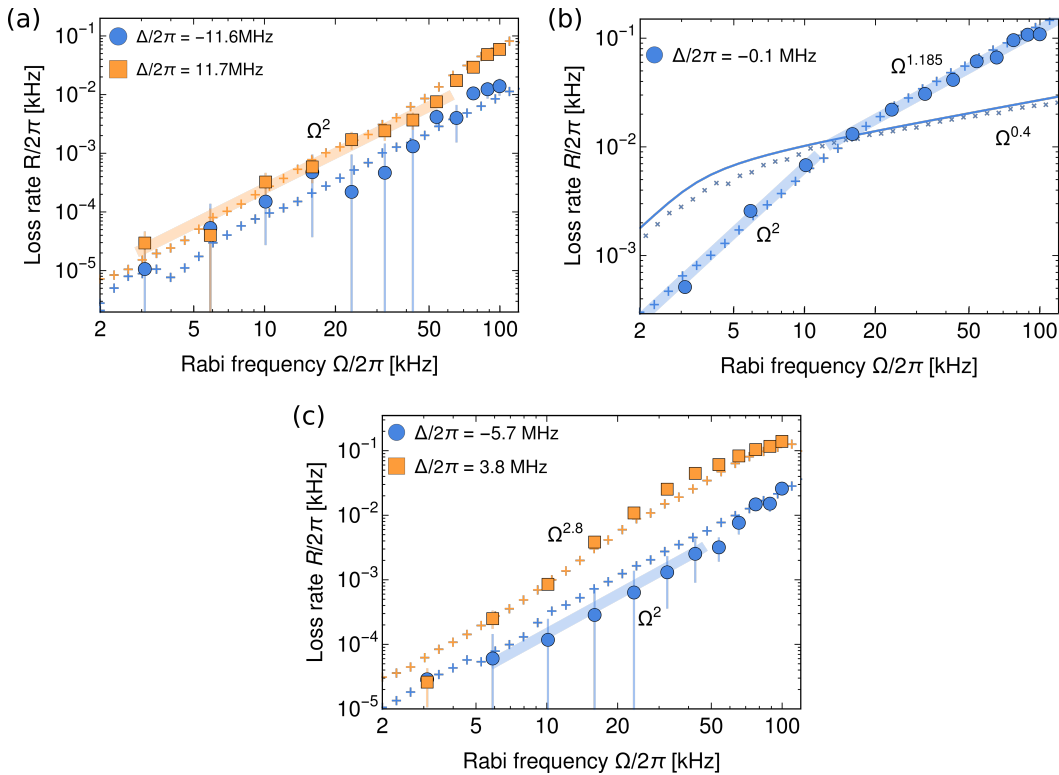


Fig. 5.3.: Power law scaling of the loss rate R as a function of driving strength with different exponents that depend on the different regimes of the driven system. The thick shaded lines show the power-law scaling with exponents used to distinguish the different regimes discussed in the text. Rate equation simulation results are shown with + symbols. (a) Far from resonance the loss rate exhibits paramagnetic scaling with $\alpha = 2$. (b) Close to resonance the loss rate exhibits two different scaling regimes with $\alpha = 2$ (dissipation-dominated) and $\alpha = 1.185$ (critical). We additionally show homogeneous results for the rate equation simulations (crosses) and for mean-field theory (solid line). (c) For intermediate detunings we observe $\alpha > 2$ attributed to facilitated excitation that tends to drive the system into the critical regime $\alpha < 2$ for large Ω . Standard errors of the mean determined over 10 repetitions of the experiment are shown as vertical bars (sometimes hidden by the plot markers). Figure adapted from [74].

In the far-detuned regime, figure 5.3(a) shows how the loss rate scales with $\alpha \approx 2$ as a function of Ω . This is consistent with the expected weak-dressed Rydberg fraction scaling $\beta^2 \propto \Omega^2/\Delta$, with additionally rate equation simulations plotted as crosses, which confirm the scaling behavior as the measured data.

Exploring the opposite regime, $\Delta \approx 0$, we measure a scaling of $\alpha \approx 2$ for small Ω (strong dissipation). When increasing the driving Ω we observe a transition to another scaling exponent with $\alpha = 1.185 \pm 0.025$, which can be related to the crossover from the dissipation dominated to the critical regime of the underlying Ising model. We further investigate this region by performing mean-field simulations of the master equation with Lindblad terms, the results are shown as a solid line in figure 5.3(b), where we clearly observe a different scaling and transition point. We use the rate equation simulations to capture better the behavior observed experimentally. We analyze two different cases: homogeneous atom distribution in a central region of the trap or include the inhomogeneity of the dipole trap (see section 2.3.2). The homogeneous case shows similar results to the mean field simulations while including the inhomogeneous light shifts can explain the loss rate behavior observed in the experiment. It may be surprising that the rate equation model, which neglects quantum coherences, can reproduce this scaling behavior. We attribute this to the fact that we concentrate on a relatively simple observable (the Rydberg excitation fraction) in the long time limit after which any observable effects of coherent dynamics are effectively washed out. From this we conclude that the observed change in scaling is indeed a transition between the dissipative-dominated and the critical regime associated to the Ising-like model.

Finally we study the intermediate detuned regime and measure that the loss rate obeys a power law in Ω with α larger than 2 for positive detunings. Figure 5.3(c) shows the results for two exemplary cases above and below resonance. The measured exponents in this regime are $\alpha = 2.8 \pm 0.4$ over a wide range of positive but also negative detunings, i.e. $\Delta/2\pi \approx 7 \pm 3$ MHz and $\Delta/2\pi \approx -3.5 \pm 1.5$ MHz. The strong scaling suggests the effect of an instability driven by fluctuations (in the sense of a continuous phase transition) as opposed to the bistable phase predicted by mean-field theory (see 2.3.1). A microscopic mechanism that can explain the stronger scaling above resonance is facilitated excitation (see section 2.2.2), which has been studied theoretically and experimentally in [141, 161, 71, 207, 142, 162, 208]. Our data shows this enhanced scaling in a very pronounced manner above resonance, but we have also observed it below resonance for a smaller parameter range. We attribute these observations below resonance to the inhomogeneous light shifts of the optical dipole trap or slight anisotropies of the interaction potential at short interatomic distances. Furthermore, our observation of power law scaling is likely evidence of an absorbing state phase transition pointed out in experiments on quasi-one-dimensional systems [208].

The RE model also qualitatively reproduces the stronger scaling ($\alpha > 2$) of the loss rate found above resonance as a consequence of the instability (further enhanced by atomic motion, see Fig. 5.3(c)). Based on this agreement between mean-field theory and the RE simulations as well as between the RE simulations and the experiment, we confirm that the change in scaling occurring around Ω_{th} is a consequence of the transition from dissipative to critical behavior linked to the equilibrium critical point of the Ising-like model. We will explore this regime in further detail in the second part of this chapter (see section 5.2).

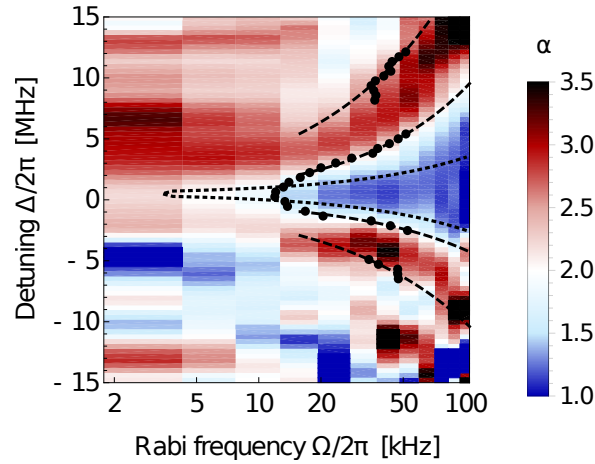


Fig. 5.4.: Experimentally measured non-equilibrium phase diagram. The locally determined scaling exponent α shows clearly distinguished regimes. The critical regime is identified as the blue region ($\alpha \approx 1.2$), while the unstable regime is red ($\alpha > 2$). The black points and dashed lines show the estimated boundary positions, the dotted line indicates the boundary to the critical regime predicted from mean-field theory corresponding to the highest density region of the cloud (trap center). Figure adapted from [74].

Non-equilibrium phase diagram—To conclude the investigation of this driven-dissipative system, we map out the non-equilibrium phase diagram by plotting the measured scaling exponents as a function of the main tuning parameters Ω and Δ . Figure 5.4 shows the phase diagram, where the scaling exponents are obtained from the slopes of linear fits to $R(\Omega)$ in a moving window on a log-log scale. We additionally locate the boundaries between the regimes by fitting connected piecewise linear functions to the log-log-scaled loss rates for each detuning. The scaling exponents show distinct regions corresponding to the critical (blue) and unstable (red) scaling regimes, while the dissipation dominated regime appears as a mostly color light region. Looking at larger positive-to-negative detunings we note a slight trend from red-to-blue is apparent, which might be evidence of a weak interaction effect on that regime. All these results allow us to conclude that the scaling laws found in the rate of population decay make it possible to uncover the non-equilibrium regimes of an Ising-like open quantum spin system governed by the competition between driving, dissipation and interactions, which can be studied in our experiment.

5.2 Observation of self-organized criticality in a driven-dissipative Rydberg gas

We aim to explore in detail the long-term dynamics of the intermediate detuning regime observed via the power-law scaling of the loss rate in the first part of this chapter. There a particularly strong scaling measured in those experiments can be attributed to facilitated Rydberg excitation. The dynamics of a driven-dissipative Rydberg gas presented in this section show that the system evolves to a self-organized critical state, when the ensemble density is over a critical density. We analyze in detail the non-linear dynamics showing that the population decay is one of the key ingredients to drive the system to a quasi-stationary state no matter the initial conditions. These results together show a first characterization of the universal properties of this system, its scale invariance and response to perturbations.

5.2.1 Model for the dynamics

Each atom in the experiment can be represented by a three level system comprising: the ground state $|g\rangle = |4s_{1/2}, F = 1\rangle$, an excited Rydberg state $|r\rangle = |39p_{3/2}\rangle$, and a set of states, referred as $|0\rangle$ which are not coupled to the system (Fig. 5.1). The laser field employed in these experiments is the single-photon excitation laser, which continuously drives the $|g\rangle \rightarrow |r\rangle$ transition with a fixed detuning Δ and Rabi frequency Ω , as depicted in figure 5.1. In the experiments performed here, we set $\Delta \gg \Omega$ such that spontaneous single-atom excitation processes are strongly suppressed but facilitated excitation is possible (see 2.2.2). Additionally, Rydberg atoms can spontaneously decay and be lost from the system, for example to another hyperfine ground state that is not coupled by the lasers.

We start describing the system dynamics via the quantum master equation of the many-body density matrix $\hat{\rho}$, including the decay and decoherence of the Rydberg state given by the Lindblad superoperator $\mathcal{L}_l(\hat{\rho})$ (eq. 2.8). The atom-light interaction Hamiltonian \hat{H} , which describes the coherent part of the system is given by

$$\hat{H} = \sum_l \left[\left(\sum_{l'} \frac{1}{2} \frac{C_6}{|\mathbf{r}_{ll'}|^6} \hat{\sigma}_{l'}^{rr} - \Delta \right) \hat{\sigma}_l^{rr} + \frac{\Omega}{2} (\hat{\sigma}_l^{gr} + \hat{\sigma}_l^{rg}) \right],$$

where $\hat{\sigma}_l^{\alpha\beta} \equiv |\alpha\rangle\langle\beta|_l$ and l, l' are indices for each atom and interactions between Rydberg states are parameterized by the van der Waals coefficient C_6 coefficient. The non-coherent part of the dynamics is included by

$$\mathcal{L}_l(\hat{\rho}) = \Gamma \hat{\sigma}_l^{0r} \hat{\rho} \hat{\sigma}_l^{r0} + \gamma_{\text{de}} \hat{\sigma}_l^{rr} \hat{\rho} \hat{\sigma}_l^{rr} - \frac{\gamma_{\text{de}} + \Gamma}{2} (\hat{\sigma}_l^{rr} \hat{\rho} + \hat{\rho} \hat{\sigma}_l^{rr}),$$

where dissipation is described by $\mathcal{L}_l(\hat{\rho})$, which includes spontaneous loss (with total rate Γ) and irreversible dephasing (rate γ_{de}) attributed primarily to laser frequency noise and Doppler broadening.

Solving the quantum master equation for the number of particles involved in our experiments presents a computational challenge, since the complexity increases with the number of components. Our approach is to derive from this equation an effective coarse-grained description for the collective dynamics. We start by averaging over the characteristic length scale corresponding to the Rydberg facilitated excitation (see 2.2.2) and project onto the density degree of freedom by adiabatically eliminating the rapidly decaying atomic coherences [159, 163]. The final result, after approximating the atomic medium as quasi homogeneous, is a Langevin equation for the density of atoms in the $|r\rangle$ state $\rho_t = \rho(t, \mathbf{r})$ (defined as the active component) and the total remaining density $n_t = n(t, \mathbf{r})$, which is the sum of the populations in the $|g\rangle$ and $|r\rangle$ states (excluding removed states $|0\rangle$):

$$\begin{aligned} \partial_t \rho_t &= (D \nabla^2 - \Gamma + \kappa n_t) \rho_t - 2\kappa \rho_t^2 + \tau(n_t - 2\rho_t) + \xi_t, \\ n_t &= n_0 - b\Gamma \int_0^t dt' \rho_{t'} + D_T \int_0^t dt' \nabla^2 n_{t'}. \end{aligned} \quad (5.2)$$

In this equation D, D_T are the diffusion constants for the active and total densities respectively, κ is the facilitation rate, τ is the spontaneous excitation rate, n_0 is the initial density and b is a dimensionless parameter that accounts for how fast decay depletes the total population. The stochastic part of the evolution is governed by the uncorrelated multiplicative noise term $\xi_t = \xi(t, \mathbf{r})$ with variance $\text{var}(\xi_t) = \Gamma \rho_t$.

Forest fire model and self-organized criticality— Remarkably, the derived Langevin equation (5.2) coincides with the model for the spreading of forest fires [209, 210], which presents self-organized criticality (SOC) dynamics. The basic model is defined in a grid in which each site can be occupied either by a healthy tree, a burning one or be just empty. The system follows four rules simultaneously: a burning tree turns into an empty space, a tree can burn if at least one neighbor is burning, there is a finite probability for a healthy tree to burn spontaneously, and there is a finite probability that an empty space can grow a healthy tree.

As an analog to our system the burning trees are mapped on to the Rydberg atoms, while the healthy trees correspond to the ground state atoms. The only difference between this model and ours is a slow regrowth term (new trees grow up) for the total density, which can bring the system from an inactive (sub critical) state, where no fire is maintained, to the critical state. In our experiment all atoms that decay

out of the two-level system are not longer involved in the dynamics, but since this regrowth is typically the slowest scale in the model and asymptotically vanishes towards self-organized criticality, we can nevertheless experimentally investigate the key features of SOC.

Self-organized criticality was first introduced by Bak, Tang and Wiesenfeld in 1987 as a way to explain scale-invariant systems found in nature [76]. These systems present a critical point which acts as an attractor and presents scale invariance, like a critical point in a phase transition, but without the need of tuning the involved parameters to their critical values, thus referring to "self-organization". SOC can be defined according to three key criteria [211, 212], all of which must be present for its unambiguous observation:

- i. Self-organization to a stationary state (self-tuning of observables to a value independent of initial conditions)
- ii. Scale invariance of bulk observables or spatio-temporal correlation functions
- iii. Critical response to small perturbations (e.g., avalanches) over an extended regime of microscopic parameters (unlike at a critical point, where a critical response only ensues for a fine-tuned parameter set)

The common ingredient of these emergent properties is that the typical "gap" of a phase transition (i.e. the distance in parameter space from the critical state) is replaced by a "dynamical gap" which self-tunes to zero by means of an intrinsic feedback mechanism.

It is particularly difficult to fully solve the dynamics (analytically and numerically) of the many-body problem described by eq. 5.2, specially for large systems like ours or for ensembles interacting in more than one dimension [213, 214]. We can nevertheless analyze two limiting cases which gives us some intuition for the upcoming results. For $b = \tau = 0$ (no decay out of the system and no spontaneous Rydberg excitation), a non-equilibrium phase transition occurs from an absorbing phase (where any excited component quickly dies out), to an active phase in which excitations spread throughout the system from arbitrarily small seed excitations. This has been observed experimentally in [208]. In the opposite case for $b, \tau \neq 0$, spontaneous excitation and decay to uncoupled states occur. Here the single atom excitation can trigger a facilitated excitation process and the particle loss characterized by b introduces in the long term dynamics a coupling between n_t and ρ_t . When $\kappa n_0 \sim \Gamma \gg b\Gamma \gg \tau$, i.e. the loss is slow compared to the internal dynamics but faster than the spontaneous excitation rate, the active density will develop growing spatio-temporal correlations until the dynamics stop just below the

critical point. Although these limits offer a good insight of the qualitative features for SOC, we expect the experiment to show quantitative differences to the simplified cases, that could only be solved by the full Langevin equation. In the next part of this chapter we experimentally characterize our system regarding the three criteria (i-iii) for SOC, uncovering the universal properties of the system and measuring for the first time one of the critical exponents of this model.

5.2.2 Signatures of SOC in the Rydberg ensemble

Self-organization measurements.— We start our experiments by investigating the first criterion for SOC, where the system is expected to evolve to the same stationary state regardless of the initial conditions. In order to corroborate this statement experimentally we study the full time evolution of the total remaining density for different initial states with peak atomic densities (n_0) that vary between $0.056(5) \mu\text{m}^{-3}$ and $0.172(2) \mu\text{m}^{-3}$. We start with all atoms in the ground state $|g\rangle$ and turn on the single-photon excitation laser (with Rabi frequency $\Omega/2\pi = 190$ kHz and detuning $\Delta/2\pi = 30$ MHz fixed) for a variable time t and measure the remaining population directly afterwards.

Figure 5.5 shows the density evolution for different initial states where a remarkable non-linearity is observed if the initial density n_0 is above a critical density ($n_c > 0.075 \mu\text{m}^{-3}$). In this particular case, we observe a short plateau, that accounts for the time needed before a first excitation occurs (this can be a relatively long time depending on the detuning) and trigger the facilitated process, followed by a rapid decay of the population that stops at a fixed density ($n_f = 0.075 \mu\text{m}^{-3}$), no matter the initial density condition (self-organization). In the opposite case for states with n_0 below the critical density, the system remains in the absorbing phase where the low density does not allow for facilitated excitation dynamics. We additionally perform measurements on a much longer time scale (see inset figure 5.5), where we observe a very slow overall decay of the population ($\tau/2\pi = 1.12(2)$ Hz) which can be attributed to single atoms that are excited and then decay out of the system. All these measurements together are a direct confirmation that the underlying mechanism for the system evolution is self-organization, therefore confirming the first criterion of SOC.

As a second step we want to corroborate that our experiment can be well described by the Langevin equation introduced in 5.2. For this we compare our data with a homogeneous mean field approximation to the Langevin equation ($D = 0$ and $\xi_t = 0$). Fig. 5.5 shows the mean field solutions (solid lines) which describe the data very well, except for a minor deviation observed around $t \approx 2$ ms. We perform a simultaneous fit to all the data, using a single set of parameters, in

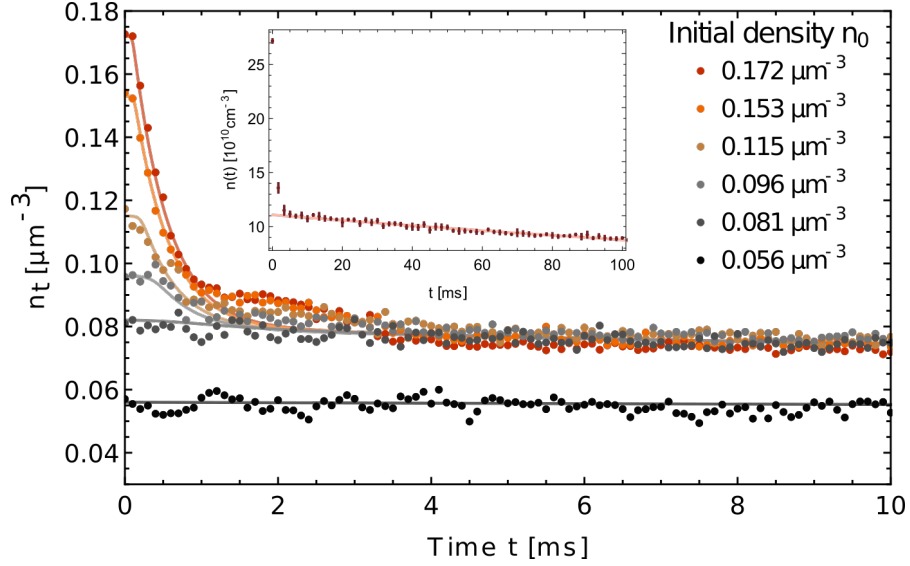


Fig. 5.5.: Time evolution of a self-organized Rydberg ensemble. Observation of self-organization: Above a threshold value, the remaining total atom density n_t is attracted to the same stationary state density independent of the initial conditions. For densities $n_0 \gtrsim 0.08 \mu\text{m}^{-3}$ the time dependence consists of a short initial plateau followed by fast exponential decay to a unique stationary state with a fixed density $n_f = 0.075 \mu\text{m}^{-3}$. For initial densities below n_f the dynamics is frozen (black points). The solid lines correspond to mean field solutions to the effective Langevin equation (see text). The inset show the density behavior for longer times, where the dynamics is dominated by single particle decay. Figure adapted from [201].

order to determine the microscopic variables of the Langevin equation. We find $\Gamma/2\pi = 11.7(9)$ kHz, $\kappa/2\pi = 144(10)$ kHz μm^3 and $b = 0.059(5)$, with statistical errors estimated using bootstrap resampling. We additionally extract the relation between κ , Ω and Δ from time traces like the ones in fig. 5.5, varying the detuning, which results in $\kappa \propto \Omega^2/\Delta^{2.06(1)}$. The fitted parameters confirm the separation of scales: $\kappa n_0 \sim \Gamma \gg b\Gamma \gg \tau$ is satisfied by an order of magnitude or more, validating that our experiments are within the regime for SOC.

Proof of scale invariance— In this section we concentrate on the second criterion (ii) for SOC, regarding the scale invariance of the macroscopic observables. The key parameter in this case is κ , since it determines the critical point of the absorbing state phase transition and its scaling behavior. In the experiment κ corresponds to the Rydberg excitation rate, which can be manipulated via the driving intensity Ω^2 of the single-photon excitation laser, in a range from 0 to 24×10^3 kHz².

In Fig. 5.6a. we examine the dependence of the quasi-stationary density n_f (reached after $t = 10$ ms of evolution) on the driving intensity Ω . For different initial densities n_0 , we observe a clear transition from an absorbing phase to an active self-organizing phase at a critical driving intensity Ω_c^2 which gets larger for smaller initial densities. We notice that the density in the active phase follows the same curve independent

of the initial density (dotted blue line in Fig. 5.6a), which is an indication of an underlying power-law. Based on the parameters extracted from the data in figure 5.5, we used mean field theory to calculate the final density dependence on the laser intensity. The results are shown as solid lines in figure 5.3(a), where we recognize the qualitative behavior of the data but also a clear quantitative difference, specially for higher densities where the critical driving intensity cannot be reproduced.

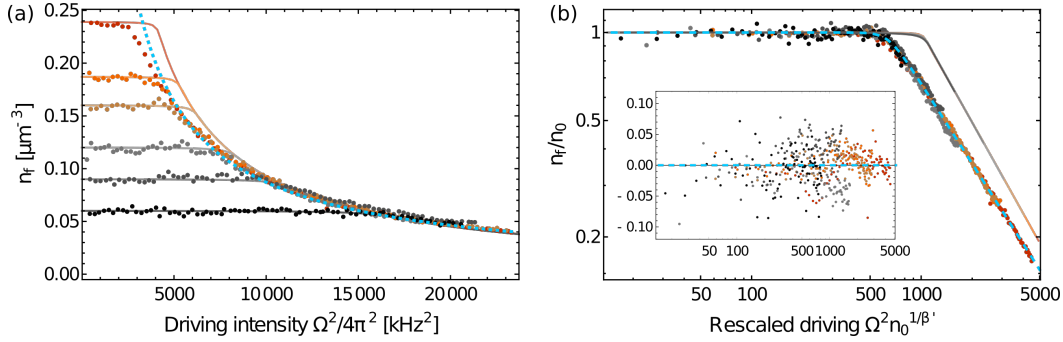


Fig. 5.6.: Scale invariance of the self-organised stationary state as a function of the driving intensity Ω^2 . (a) Stationary state density n_f measured at $t = 10$ ms (when the dynamics has stopped) as a function of Ω^2 and for different initial densities n_0 using the same parameters as for Fig. 5.5 except $\Delta/2\pi = 18$ MHz (to obtain a longer dynamical range). For large Ω^2 and n_0 all points collapse onto one single powerlaw curve $n_f \propto \Omega^{-2\beta}$ (dotted blue line). (b) The same data with rescaled axes to achieve full data collapse, revealing the universal scaling function (with fit shown by the dashed blue line) for the stationary density n_f . The inset shows the normalised residuals between the rescaled data and the fitted scaling function. Each datapoint is the mean of approximately 6 measurements. The solid lines in (a) and (b) correspond to mean field solutions of the effective Langevin equation. Figure adapted from [201].

In order to quantify the scale-invariant properties of the data, we apply the scaling ansatz $n_f = n_0 F(\Omega^2 n_0^{1/\beta'})$ [166]. Figure 5.6(b) shows how all the data collapses onto a single curve when plotting n_f/n_0 as a function of $\Omega^2 n_0^{1/\beta'}$. We make use of the heuristic function $F(x) = x_c^\beta (x^{v\beta} + x_c^{v\beta})^{-1/v}$ to describe the data behavior (see dashed blue line in fig. 5.6(b)), where x_c is related to the position and v to the sharpness of the transition region between absorbing and active phases. From this we extract the best scaling exponent for the data collapse to be $\beta' = 0.869(6)$. We additionally observe that the density deep into the active phase ($x \gg x_c$) follows the power-law $n_f \sim \Omega^{-2\beta} n_0^{1-\beta/\beta'}$, with β the scaling exponent that characterizes the stationary density and $1 - \beta/\beta'$ the parameter that quantifies how (in)sensitive it is to the initial density. We extract the parameters of the function $F(x)$ by fitting the rescaled data on a log-log scale where power-law functions are straight lines. The results are $\beta = 0.910(4)$, $v = 10.6(8)$ and $x_c = 641(3) \text{ kHz}^2 \mu\text{m}^{-3/\beta'}$ with the statistical errors shown in parenthesis. Figure 5.6(b) shows how well $F(x)$ describe the data (blue dashed line) using those parameters, further corroborated by plotting the normalized residuals which are small and scattered evenly around zero (see inset). Furthermore we compare these remarkable results with mean field theory

which predicts a scaling exponent of $\beta'_{MF} = \beta_{MF} = 1$ and clearly shows that it can not reproduce our results, which implies they are beyond mean field theory. These results together prove that the quasi-stationary state can be characterized by a single function which is scale invariant over the entire parameter regime of the experiment, confirming criterion (ii).

Response to perturbations— As a final step to prove that our system shows self-organized criticality, we explore criterion (iii) by analyzing the response of the system to small perturbations. The underlying idea in SOC is that the critical state acts as an attractor for the dynamics such that small perturbations will trigger avalanche processes that drives the system back to a new critical state. In our specific case the best way to induce such perturbations is via the driving intensity Ω^2 which thus changes accordingly the facilitation rate κ .

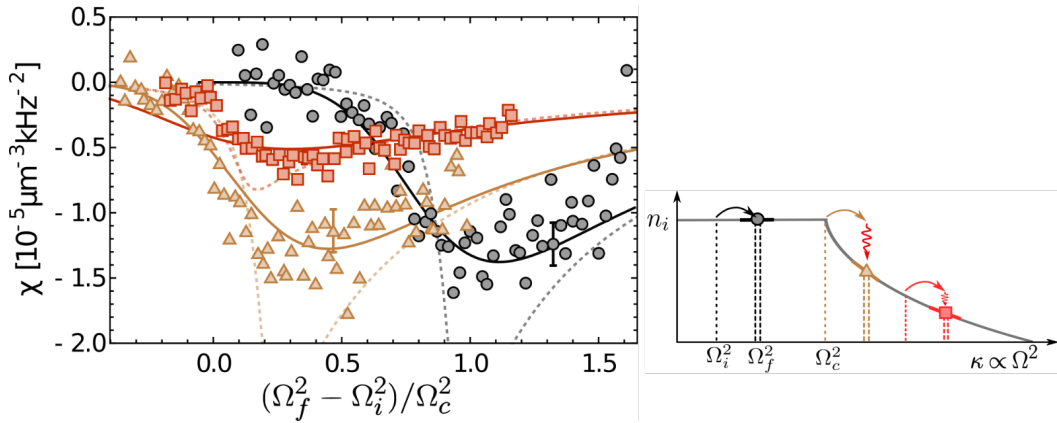


Fig. 5.7.: Response of the self-organised critical state to external perturbations. The solid lines correspond to predictions based on the experimentally determined scaling function and dotted lines correspond to mean field predictions. For reference we show two representative error bars corresponding to the standard error of the mean. (right sub figure) Sketch of the experimental procedure used to measure the susceptibility $\chi = dn_f/d(\Omega_f^2)$ by quenching the spreading parameter $\kappa \propto \Omega^2$ across the absorbing state phase transition. It shows a representation of the three different initial conditions corresponding to the absorbing phase (black circles), critical (yellow triangles) and active phase (red squares). Figure adapted from [201].

By suddenly changing the driving intensity, we can explore the system response to perturbations in different regimes. If the ensemble is deep in the absorbing phase a small perturbation will not affect the system, only changes above the critical driving value can generate avalanches, this is known as the dynamical gap. In the opposite case where the system is already in the active phase any small perturbation should trigger an avalanche process that would bring the system to a new critical state, with lower density. Experimentally we analyze three different regimes (depicted in the sub-figure 5.7): the deep absorbing phase (black circles), the critical region (yellow triangles) and the active phase (red squares). To measure

the response we start from the stationary state reached after $t = 10$ ms in the different regimes depending on Ω_i^2 . We then induced the perturbation by switching the driving intensity to Ω_{f1}^2 and wait 10 ms more such that the system can reach the new quasi-stationary state, and measure the remaining atoms. Then we perform a second measurement like the first one but changing the final driving intensity to Ω_{f2}^2 . With these results we can estimate the susceptibility of the ensemble as $\chi = dn_f/d(\Omega_f^2) = [n_f(\Omega_{f1}^2) - n_f(\Omega_{f2}^2)]/(\Omega_{f1}^2 - \Omega_{f2}^2)$ with $\Omega_f = (\Omega_{f1} + \Omega_{f2})/2$. The susceptibility quantifies the response of the system (its final density) to a perturbation ($\Omega_{f1}^2 - \Omega_{f2}^2$).

The results are shown in figure 5.7, where the susceptibility χ is plotted as a function of the normalized change in driving intensity $\delta = (\Omega_f^2 - \Omega_i^2)/\Omega_c^2$, in the three different absorbing, critical and active regimes. In all three cases we observe a minimum in the susceptibility which relates to the strongest response of the system, which deep into the absorbing phase (black circles) is measured for a δ close to 1 which relates to the dynamical gap. On the other hand, when the system is in the critical regime or deep into the active phase (yellow triangles and red squares respectively) such a minimum is observed close to 0 (small perturbation in the driving field). We further analyze the data based on the susceptibility that can be extracted from a derivative of the scaling function $F(x)$ (determined experimentally with $\beta = 0.910$). Figure 5.7 shows that the results (solid lines) are in good agreement with the actual data, in contrast to the mean field predictions (dotted lines), which can not capture either the strength of the response in the susceptibility nor the width.

Having proved all three criteria that describes SOC, we can conclude that our system presents clear signatures of self-organized criticality. Therefore those results establish Rydberg systems as a versatile and well controlled platform that can be exploit for investigating self-organized phenomena and non-equilibrium universality.

5.2.3 Towards studies of the role of quantum coherence in non-equilibrium systems

In this chapter we have shown one of the main applications for a Rydberg platform where the typical problem of decay is used in a positive way to study driven-dissipative systems. We explored the non-equilibrium phase diagram of the Rydberg platform and discover that the scaling laws related to the loss rate measurements are appropriate to determine the different regimes of the non-equilibrium system. Additionally we have explored the dynamics of the regime where driving and dissipation strongly compete, and shown that the system presents self-organized criticality.

The first experiments presented in this chapter showed that scaling laws found in the rate of population decay are a powerful tool to uncover the non-equilibrium phases of an Ising-like open quantum spin system. The measured phase structure is extremely rich, exhibiting features related to the equilibrium quantum Ising model, but also genuinely new non-equilibrium aspects, such as the collectively enhanced crossover from dissipation-dominated to the critical regime. In a second experiment we concentrate on the particular regime where the scaling is clearly larger than the typical quadratic one, which is attributed to facilitated Rydberg excitation. We studied in detail the dynamical response of the system and discovered a self-organized critical behavior, that is reflected in the nonlinear evolution towards the same quasi-stationary state independent of the initial conditions, in the scale invariance, and in the response to perturbations. Still many properties of this system are debated, such as whether the system self-organizes towards a truly critical state, and whether it fulfills the universal scaling relations expected for SOC [215, 210].

These results pave the way for new studies of non-equilibrium systems that combined with single-atom imaging tools will allow us to investigate the correlations built in such systems. Future experiments aiming to learn more about the microscopic origins of these observations could reveal the build up of spatial correlations (using high resolution imaging techniques for Rydberg atoms [216, 217]), look for possible self similar dynamics in the transient evolution [218], or explore the precise relation between SOC and other non-equilibrium universality classes by measuring other observables such as avalanches and their statistics.

Furthermore, the theoretical models studied here neglect the effects of coherence due to the time scales we investigate in our experiments. Additionally measurements could explore the interface between driven-dissipative and isolated quantum systems governed by competing classical and quantum dynamical rules [77, 78, 219], ultimately leading to a comprehensive and quantitative understanding of non-equilibrium universality. Therefore it is of great interest to enhance the coherence in the system such that in the long term dynamics the coherences can not be neglected. In order to do that we need to characterize the coherence properties of the ensemble and find out the main noise sources that can be improved to reduce decoherence effects. In the next chapter we show an innovative technique to identify the decoherence mechanisms present in the Rydberg system.

A Rydberg dressed interferometer

Atomic clocks have proven to be a remarkable platform for highly precise measurements based on their extreme isolation from the environment and the weak interaction between the involved particles. While the high level of control and reduced influence from external factors have allowed for amazing precision studies [195, 91], measurements of strongly interacting matter are actually restricted. Within this thesis we take a different approach: based on a clock transition made up of two magnetically insensitive hyperfine ground states, we couple continuously one of the clock states to a Rydberg state by an off-resonant laser field. Using the Rydberg-dressing approach provides the means to combine the outstanding coherence properties of atomic clocks with greatly enhanced sensitivity to external fields and controllable interparticle interactions mediated by the Rydberg state admixture. The main results presented in this chapter are based on the publication "Realization of a Rydberg-dressed Ramsey interferometer and electrometer" [220].

In the first part of this chapter a theoretical model of the dressed clock transition is presented, including a detailed description of Ramsey interferometry and the expected signal from the Rydberg-dressed interferometer. The chapter continues by showing Ramsey interferometry measurements of the bare and the dressed atomic transition. As a first application we use the interferometer to precisely measure the Rydberg-atom light coupling strength and to independently determine the effective population decay and dephasing rates of the dressed-state, further identifying the dominant decoherence processes. From these results we assess the suitability of Rydberg-dressed interferometers for metrological applications (showing its use as a precision electrometer) and for inducing and characterizing long-range interactions in many-body quantum systems.

6.1 Theoretical model of a Rydberg-dressed interferometer

6.1.1 Ramsey interferometry

An intuitive representation of the two-level system interacting with an electromagnetic field (see section 2.1.3) is the Bloch sphere [221, 222]. This representation allows, as we will see in the following, to understand the time evolution of such a system in an easier way. We start with \vec{S} as the vector describing the system in terms of the density matrix elements, such that:

$$\begin{aligned} S_x &= \rho_{10} + \rho_{01} \\ S_y &= \text{Im}[\rho_{10} - \rho_{01}] \\ S_z &= \rho_{00} - \rho_{11} \end{aligned} \quad (6.1)$$

with ρ_{ij} an element of the density matrix $\hat{\rho}$ that represents the two-level system. The master equation without any decay or dephasing (Equation 2.8, with $\mathcal{L} = 0$) can be written as $\partial\vec{S}/\partial t = \vec{\Omega} \times \vec{S}$, with $\vec{\Omega} = (-\Omega, 0, \Delta)^T$. This corresponds exactly to the coupled differential equations of a two-level system presented in ??, which can be re-written as:

$$\begin{aligned} \frac{\partial S_x}{\partial t} &= -\Delta S_y \\ \frac{\partial S_y}{\partial t} &= \Delta S_x + \Omega S_z \\ \frac{\partial S_z}{\partial t} &= -\Omega S_y \end{aligned} \quad (6.2)$$

Under this description, the time evolution of the density matrix that describes the system can be seen as a rotation of \vec{S} in the Bloch sphere.

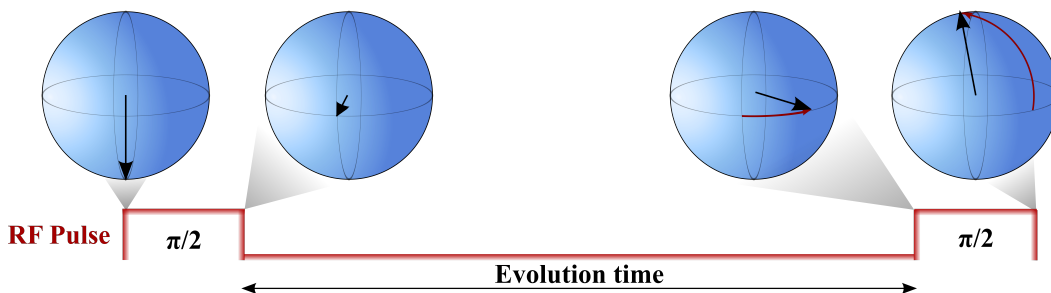


Fig. 6.1.: Schematic representation in the Bloch sphere of a Ramsey sequence. The two-level system starts in the down state (black arrow), here referred as $|0\rangle$. First a $\pi/2$ pulse is applied, creating a superposition between the two states $|0\rangle$ and $|1\rangle$. Then the system is left to evolve in the absence of the laser field (i.e. $\Omega = 0$) during some evolution time (T). Finally a second $\pi/2$ pulse is applied to measure the population in one of the states.

Ramsey interferometry is a method used to measure the effect of an external field in an atomic system. The system is first aligned in the z-axis of the Bloch sphere (i.e. is either in the $|0\rangle$ or $|1\rangle$ state). A $\pi/2$ pulse is applied with the coupling field in order to bring the system into a superposition of $|0\rangle$ and $|1\rangle$. After that the system is allowed to evolve for some time T in the absence of the coupling light field, the master equation during this period of free evolution is:

$$\frac{\partial S_x}{\partial t} = -\Delta S_y, \quad \frac{\partial S_y}{\partial t} = \Delta S_x, \quad \frac{\partial S_z}{\partial t} = 0. \quad (6.3)$$

This implies that the system only evolves in the x-y plane only with the relevant parameter being Δ . In the simplest case where only the light field influence the system, the Bloch vector will evolve with a phase ΔT . The Ramsey method works in the limit where the $\pi/2$ pulse does not cause any population loss or dephasing, i.e. $\pi/2\Omega \ll 1/\gamma$ the pulse length is much shorter than the lifetime of the atom decay. Additionally the coupling Rabi frequency must be much larger than Δ .

Furthermore in the presence of other fields that can vary the detuning Δ , the Ramsey method is a powerful technique to precisely measure those extra fields, for example shifts due to magnetic fields, atom collisions or other light fields coupling the involved atomic states.

After the evolution time a second pulse is applied ($\pi/2$) which rotates the vector again, around the same axis as in the first pulse. After this rotation, population can be measured either in state $|0\rangle$ or $|1\rangle$. Due to the rotation in the X-Y plane during the free evolution, the projection into one of the states will reflect the phase change and therefore by varying the time T one can measure the phase evolution in time and extract from it the detuning Δ .

Spin echo technique.— In the many body picture each vector would represent an atom (a two-level system) which will freely evolve according to the Δ field affecting it. Therefore if the local conditions are not equal everywhere each vector will rotate at different velocities, causing a distribution of vectors resulting in a blurring when the projection measurement is done, this is what we call dephasing.

In order to compensate the dephasing of the many body system, caused by single particles, we can use another method similar to Ramsey interferometry, the spin echo. The simplest way to understand this technique is as two Ramsey sequences together. Figure 6.2 shows the spin echo method which starts with a $\pi/2$ pulse, followed by the free evolution time T . Next, instead of a second $\pi/2$ pulse like in Ramsey interferometry, a π pulse is applied rotating each single particle vector such that the x and y components become $S_{x/y} = -S_{x/y}$. In the next free evolution time T the single particle accumulated phase will cancel out with the first one and if no

other field is changed or interaction between the particles occur the last $\pi/2$ pulse brings all the particles back to the initial state $|0\rangle$.

The advantage of this technique is that in principle the dephasing caused by single particles is not measured anymore, therefore other effects can be studied such as particle interactions or the effect of a field that changes between the two evolution times.

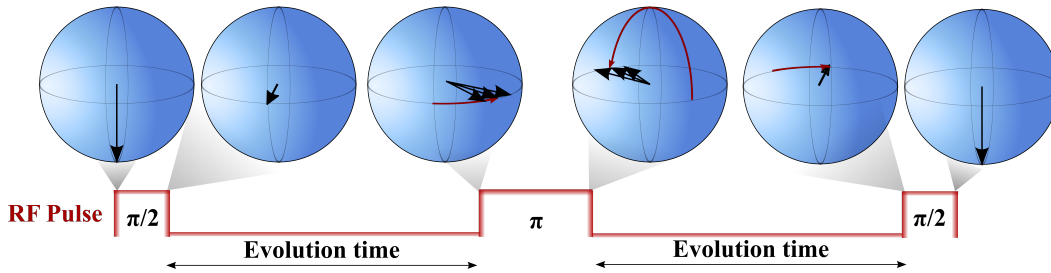


Fig. 6.2.: Schematic representation in the Bloch sphere of a spin echo sequence. The two-level system starts in the down state (black arrow), here referred as $|0\rangle$. First a $\pi/2$ pulse is applied, creating a superposition between the two states $|0\rangle$ and $|1\rangle$. Then the system is left to evolve in the absence of the laser field during some evolution time (T), where in the case of dephasing each two-level particle would acquire a different phase. A π -pulse is applied followed by a second free evolution time, where the single dephasing of the particles is canceled out. Finally a second $\pi/2$ pulse is applied to measure the population in one of the states.

6.1.2 Rydberg dressed Ramsey signal

Having understood the principle of Ramsey interferometry in a two-level system, we proceed to model the effect of an additional laser field that couples only one of the clock states to a highly excited Rydberg state. To interpret the effects of Rydberg dressing during the free evolution time in the Ramsey sequence, we derive a simple analytical formula for the Ramsey signal that includes the influence of noise from the dressing laser and neglects interaction effects, which is justified by the low densities used for these experiments.

We start by considering an ensemble of identical four-level atoms, comprised of the clock states $|0\rangle, |1\rangle$, the Rydberg state $|r\rangle$, and an auxiliary shelving state $|s\rangle$ which collectively describes all states into which the Rydberg atoms can decay and that no longer participate in the dynamics, as depicted in figure 6.3. The system evolution, during which the dressing laser is turned on, is well described by a quantum master equation for the density matrix ρ in Lindblad form: $\dot{\rho} = -i[\hat{H}, \rho] + \mathcal{L}(\rho)$ (see equation 2.8). \hat{H} accounts for the coherent dynamics and \mathcal{L} is a superoperator describing irreversible dissipative processes. For the moment we assume that the only dissipative process is decay from $|r\rangle$ to $|s\rangle$ state with rate Γ and processes that bring population back out of the $|s\rangle$ state can be neglected. Accordingly, the

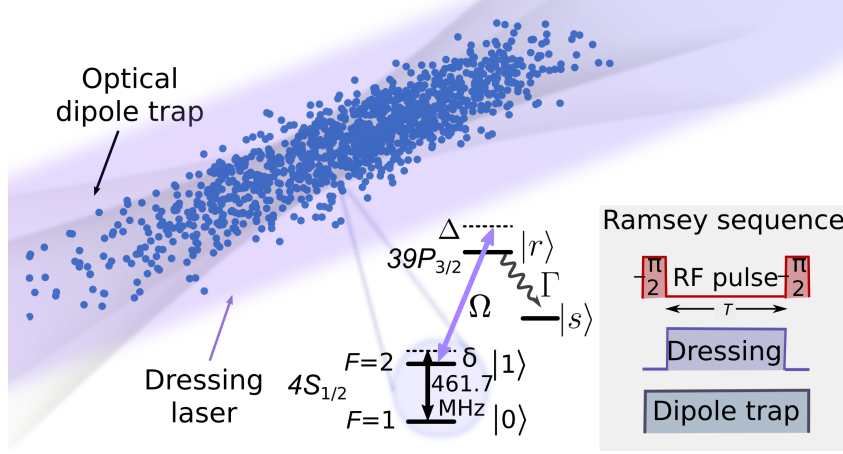


Fig. 6.3.: Experimental realization of a Rydberg-dressed Ramsey interferometer. A cloud of ^{39}K atoms is prepared in an optical dipole trap and uniformly illuminated by the Rydberg dressing laser. Each atom can be represented by a four level system involving the clock states $|0\rangle$ and $|1\rangle$, the $|r = 39P_{3/2}\rangle$ Rydberg state and an auxiliary shelving $|s\rangle$. The $|1\rangle \rightarrow |r\rangle$ transition is coupled via the dressing laser with Rabi frequency Ω and detuning Δ during the Ramsey free evolution time T . Figure adapted from [220].

quantum master equation can be reduced to a Schrödinger equation governed by the non-Hermitian Hamiltonian:

$$\hat{H}_{\text{NH}} = \frac{\Omega}{2} (|1\rangle\langle r| + |r\rangle\langle 1|) - \left(\Delta + \frac{i\Gamma}{2} \right) |r\rangle\langle r| - \delta|0\rangle\langle 0|, \quad (6.4)$$

where Ω, Δ are the amplitude and detuning of the Rydberg laser coupling and δ is the detuning of the rf field from the clock transition. Rydberg state decay appears as an additional imaginary detuning $i\Gamma/2$ which describes overall population loss from the Rydberg state out of the system with rate Γ .

In the weak dressing limit $|\Delta| \gg \Omega, \Gamma$, the $|r\rangle$ state can be adiabatically eliminated yielding an effective Hamiltonian for the slowly evolving clock states,

$$\hat{H}_{\text{eff}} = f_r \left(\Delta - \frac{i\Gamma}{2} \right) |1\rangle\langle 1| - \delta|0\rangle\langle 0|, \quad (6.5)$$

where $f_r = \Omega^2/(\Gamma^2 + 4\Delta^2)$ can be recognized as the steady state Rydberg fraction of the dressed $|1\rangle$ state.

As a second step we include the intensity and frequency noise of the dressing laser by treating the light shift as a fluctuating quantity that is influenced by the noise such that $E_{\text{LS}} \rightarrow E_{\text{LS}} + \sqrt{X}\xi(t)$, where $\xi(t)$ is assumed to be a zero mean white noise process with $\langle \xi(t)\xi(t') \rangle = \delta(t - t')$. We define the noise variance,

$$X \approx \left(\epsilon_I^2 + \epsilon_\Delta^2 \right) \frac{\Omega^4}{16\Delta^2}, \quad (6.6)$$

as a sum of the spectral densities of the relative intensity and detuning noise [ϵ_I^2 and ϵ_Δ^2 respectively, with units (frequency) $^{-1}$]. The additional factor $\frac{\Omega^4}{16\Delta^2}$ accounts for the dressing admixture because the noise influence will depend on the coupling between $|1\rangle$ and $|r\rangle$.

Following [223] we write the stochastic time-dependent von Neumann equation for the density matrix ρ_{eff} as,

$$\dot{\rho}_{\text{eff}} = -i[H_{\text{eff}}, \rho_{\text{eff}}] - i\sqrt{X}\xi(t)[|1\rangle\langle 1|, \rho_{\text{eff}}], \quad (6.7)$$

where we include the noise only for the clock state couple to the dressing laser ($|1\rangle$). By performing the Markov approximation and using the identity for multiplicative linear white noise in [223], we arrive at

$$\dot{\rho}_{\text{eff}} = \left(\mathcal{L}_0 + \frac{1}{2}X\mathcal{L}_1^2 \right) \rho_{\text{eff}}(t), \quad (6.8)$$

where $\mathcal{L}_0\rho_{\text{eff}} = -i[H_{\text{eff}}, \rho_{\text{eff}}]$ and $\mathcal{L}_1\rho_{\text{eff}} = -i[|1\rangle\langle 1|, \rho_{\text{eff}}]$.

Considering the Ramsey sequence in figure 6.3 and applying Eq. (6.8) during the free evolution time, the population in the $|1\rangle$ state after the second $\pi/2$ pulse can be calculated as:

$$P_1 = \frac{1}{4} \left(1 + e^{-f_r\Gamma t} + 2e^{-\frac{1}{2}(f_r\Gamma+X)t} \cos[(\delta + f_r\Delta)t + \phi] \right), \quad (6.9)$$

where we have included the possibility of a small phase shift ϕ caused by the detuning during the two $\pi/2$ pulses. From this equation we can clearly identify the effects of Rydberg dressing in the Ramsey signal, as a light shift of the $|1\rangle$ state which changes the clock transition frequency by an amount $E_{\text{LS}} = f_r\Delta$, an overall population decay with rate $\Gamma_{\text{eff}} = f_r\Gamma$ and pure dephasing rate X .

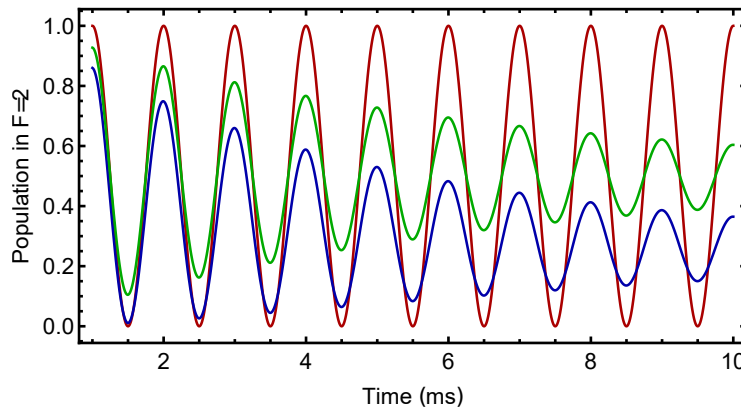


Fig. 6.4.: Example of the expected Ramsey fringes. Calculation of equation 6.9 for three different cases: (red) $\Gamma_{\text{eff}} = 0\text{kHz}$ and $X = 0\text{kHz}$, (green) $\Gamma_{\text{eff}} = 0\text{kHz}$ and $X = 0.05\text{kHz}$, and (blue) $\Gamma_{\text{eff}} = 0.05\text{kHz}$ and $X = 0\text{kHz}$,

Figure 6.4 shows an example of the expected Ramsey signal for three different cases. When no decay or dephasing is present the signal is a simple Cos with no damping (shown in red). When only dephasing is present (green curve) the contrast is reduced but the mean population remains the same. Finally in the case $\Gamma_{\text{eff}} \neq 0$ we observe decay of contrast and also population.

6.2 Ramsey interferometry of a Rydberg-dressed sample

6.2.1 Analysis of the Ramsey interferometry signals

We now apply the Ramsey method to our system in order to identify the influence of the Rydberg state in the clock transition. Figure 6.5a shows the measured Ramsey fringe pattern taken without the dressing field for free evolution times up to 15 ms. During this time the signal is very well described by a sinusoidal oscillation with essentially no visible loss of contrast. We further measure the Ramsey interferometry signal for longer times and extract a population decay rate of 1.9 Hz and a dephasing rate of 32.2 Hz.

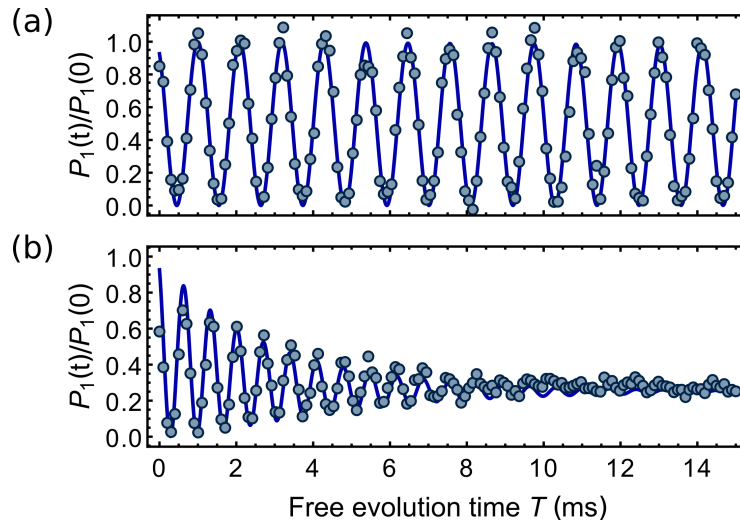


Fig. 6.5.: Measurement of Ramsey fringes. (a) Ramsey fringes measured in the absence of the dressing laser showing very good coherence and (b) Ramsey fringes with the Rydberg excitation laser on with $\Delta/2\pi = -12.0$ MHz, showing a modified oscillation frequency and asymmetric decay of the interference contrast. The blue solid lines correspond to fits to the model described in the text.

We additionally determine the clock transition frequency by precisely extracting the Ramsey detuning for different δ and extrapolate the frequency for the $|0\rangle \rightarrow |1\rangle$ transition. By fitting the oscillation frequency we extract the Ramsey detuning of $\delta/2\pi =$

914.0(6) Hz. This corresponds to an absolute frequency of 461.719 748 0(6) MHz (statistical uncertainty in the fractional frequency of $\Delta f/f = 1.3 \times 10^{-9}$) which is within 30 Hz of previous measurements of the ^{39}K hyperfine splitting [224, 187]. The small discrepancy can be accounted for by the expected quadratic Zeeman shift of 31(11) Hz given that we apply a relatively large bias field of 60(10) mG and additional smaller corrections due to the differential AC Stark shift from the optical dipole trap and cold collisions.

After precisely characterizing the RF detuning, we now proceed to dress the atomic clock by applying a laser field during the free evolution time which is detuned by from the $|1\rangle \rightarrow |r = 39P_{3/2}\rangle$ transition. The laser excitation system to perform the dressing in these experiments is the 286 nm laser (used for one-photon excitation). We use 65 mW of the laser which is weakly focus into the atoms such that the intensity is approximatively uniform over the cloud. The excitation creates, in the dressed-state picture [225], an admixture of a small Rydberg state component into the clock state i.e. $|\tilde{1}\rangle \approx |1\rangle + \sqrt{f_r}|r\rangle$, where f_r is the relative population of the Rydberg state and $f_r \ll 1$.

Fig. 6.3b shows an example of a Ramsey signal of the Rydberg-dressed interferometer for a detuning of $\Delta/2\pi = -12.0$ MHz. In comparison to the case of the bare atomic clock (fig. 6.3a), we observe an asymmetric decay of interference contrast and a visible shift of the clock transition frequency. We use the formula for the population behavior in the Ramsey sequence (eq. 6.9) to fit the data. From this we extract the induced light shift $E_{LS} = 1.44(\pm 0.001)$ kHz, the effective population decay $\Gamma_{eff} = 6.3(\pm 0.1) \times 10^{-3}$ kHz and the dephasing $X = 5.6(\pm 0.2) \times 10^{-2}$ kHz. This result clearly shows the strong influence of the dressing laser in the clock transition.

6.3 Characterization of a Rydberg dressed ensemble

In this section we aim to analyze in detail the performance of the Rydberg-dressed interferometer for different detunings of the dressing laser (Δ). In order to do that, we measure Ramsey signals for the Rydberg dressed clock transition and fit the results to Eq. (6.9) including an experimentally determined phaseshift $\phi = 0.55$. As exemplified by the solid lines in Fig. 6.5 the model reproduces the data extremely well. From these fits we can extract parameters E_{LS} , Γ_{eff} , and X as a function of the detuning and investigate thoroughly the influence of the dressing in the atomic clock transition.

6.3.1 Atom-light coupling strength

We first analyze the induced light shift (E_{LS}) as a function of the dressing laser detuning (Δ). Figure 6.6 shows the interferometer frequency which corresponds to $\delta + E_{LS}$, for different detunings of the Rydberg dressing laser in the range ± 40 MHz. The Rydberg induced light shift E_{LS} can be extracted by measuring δ in the case where no dressing laser is coupled to the system (black dashed line). We additionally show a density plot in the background of the figure, which corresponds to the Fourier transform of each respective Ramsey signal. This gives additional information about the spectral width of the Ramsey signal.

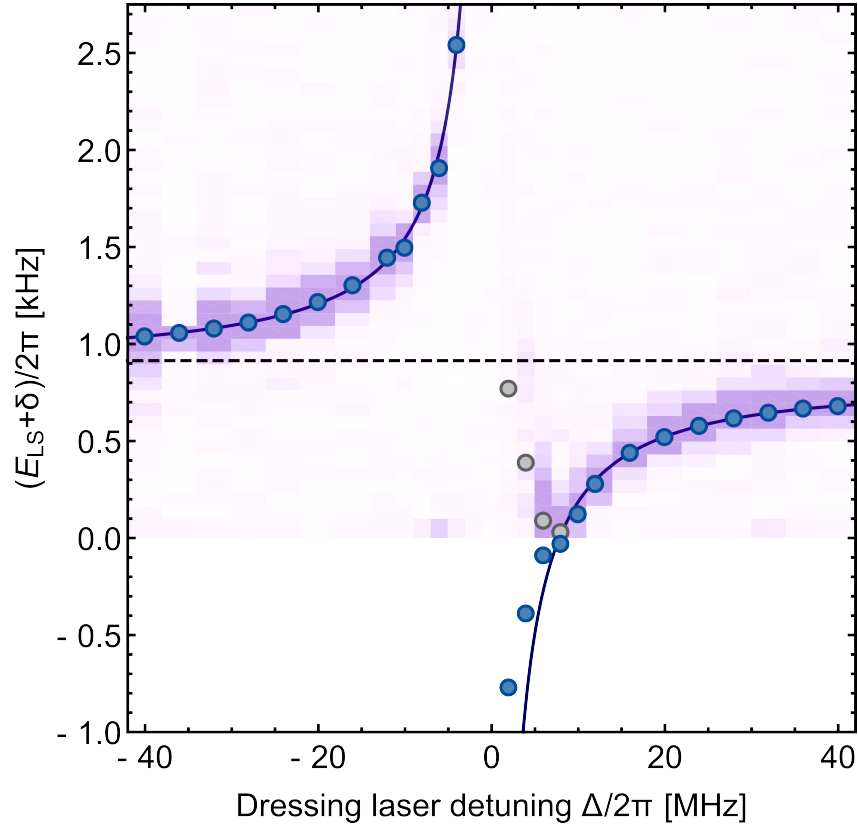


Fig. 6.6.: Analysis of the Rydberg induced light shift and laser coupling as a function of the Rydberg dressing laser detuning Δ . Interferometer frequency $E_{LS} + \delta$ (blue circles) in the presence of the dressing laser is measured for different detunings Δ . Gray circles correspond to positive oscillation frequencies before mapping the data (see text). The statistical errors for each measurement are typically well within the size of the data points ($\lesssim 50$ Hz). The solid line is a fit to the theoretical model for the dressed-state energy from which we determine the atom-light coupling strength Ω . The dashed line corresponds to the Ramsey detuning δ . The shaded background shows the Fourier transform of each Ramsey measurement. Figure adapted from [220].

In order to fit the light shift dependence on the detuning, we need to account for the cases close to resonance where the clock transition frequency $E_{LS} + \delta$ goes through

zero, i.e. E_{LS} compensates the RF detuning δ , and should become negative. We map the sign of the data points in that region such that the frequency shift is monotonic as a function of Δ (these data points before mapping are displayed in gray in Fig. 6.6). Although the measured light shifts are relatively small, $\lesssim 1$ kHz over most of the range, they are clearly resolved with an average statistical uncertainty of $\sim 2 \times 10^{-3}$ for $|\Delta|/2\pi > 10$ MHz. Within this accuracy we observe small deviations from the simple two-level weak-dressing prediction of $E_{LS} = \Delta\Omega^2/(\Gamma^2 + 4\Delta^2)$. Therefore, we need to include the additional light shift caused by the nearby transition $|0\rangle \rightarrow |39P_{1/2}\rangle$ which is resonant for $\Delta/2\pi = 76$ MHz. The fit including this extra state is shown as a solid line in Fig. 6.6, where the quality of the fit reflects a good quantitative understanding of the dominant effects influencing the frequency of the Rydberg-dressed interferometer. This relatively simple fit also confirms that interaction effects such as the Rydberg blockade do not play an important role for the experiments performed here.

From the fit shown in figure 6.6 we obtain a precise determination of the Rabi frequency $\Omega/2\pi = 163(1)$ kHz. The value of Ω is more than a factor of two smaller than an independent estimate based on the power and waist of the laser beam and the expected transition dipole matrix element. This highlights the importance of direct experimental measurement of the atom-light interaction parameters over indirect estimates. The range of resolved light shifts corresponds to Rydberg fractions from approximately 4×10^{-4} to a minimum value of 4×10^{-6} , corresponding to less than one Rydberg excitation shared amongst the entire cloud. This confirms that in the current experiments Rydberg interaction effects are negligible, but also emphasizes the sensitivity of the atomic clock transition to very small perturbations.

6.3.2 Ramsey contrast: Dephasing and population decay

Furthermore we study the macroscopic behavior of the population and coherence decay, which are also extracted from the Ramsey measurements, the results are shown in figure 6.7. The decaying contrast of the Ramsey fringes gives further information on the Rydberg-dressed states, specifically their degree of coherence which is influenced by fluctuations of the dressed state energy and population decay, as shown in equation 6.9. While fluctuations like laser intensity or frequency affects the result in a symmetric loss of contrast with respect to the mean (dephasing), population loss causes an overall reduction of the mean value, besides affecting the dephasing. As such, these contributions can be separately extracted from the fits to Eq. (6.9) and are shown in Fig. 6.7 on a logarithmic scale. Close to resonance we find that the contributions are approximately equal with a rate around 1 kHz. This is comparable to the bare Rydberg state decay rate estimated as $\Gamma/2\pi = 5.6$ kHz which includes photoionization from the optical dipole trap, blackbody

redistribution and spontaneous decay. Interestingly, the maximum dephasing rate is two orders of magnitude smaller than the independently measured laser linewidth (see section 4.3.1) showing that the correspondence between laser phase noise and the loss of coherence can be subtle. For large detunings $|\Delta|/2\pi > 5$ MHz the effective loss and dephasing rates drop off rapidly, reaching values that are orders of magnitude lower than the bare Rydberg state decay rate. Here we find that pure dephasing is the dominant effect governing the loss of coherence rather than intrinsic atom loss from the Rydberg state.

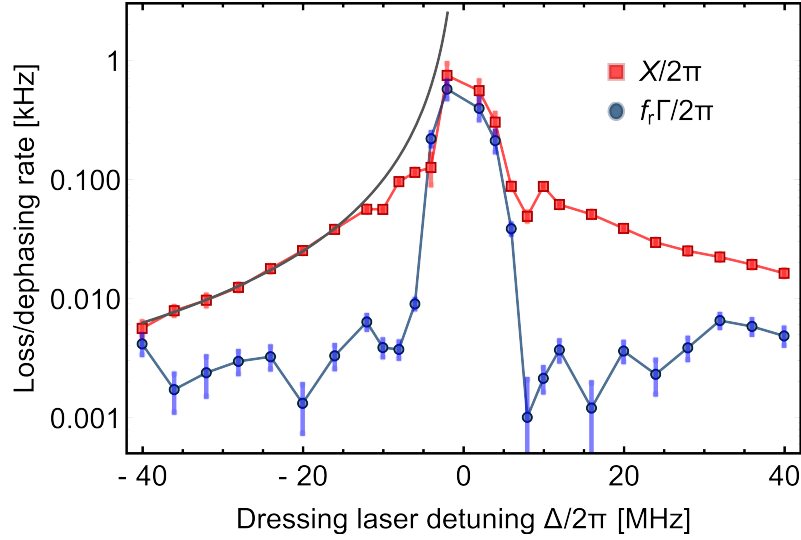


Fig. 6.7.: Analysis of the dressed Ramsey interferometer regarding the Rydberg-dressed population and coherence decay. Dressed-state dephasing rate \bar{X} (red squares) and population decay rate $f_r\Gamma$ (blue circles) as a function of Δ . The black curve shows the power law Δ^{-2} which is the expected dependence for intensity-noise dominated dephasing. Figure adapted from [220].

Looking closer at the detuning dependent dephasing rate we find that it is well described by a power-law which, below resonance, scales with $\Delta^{-1.98(4)}$. This is close to the expected scaling for intensity noise, which according to Eq. (6.6) should scale as $X \propto |\Delta|^{-2}$, as opposed to laser frequency noise which should scale with $|\Delta|^{-4}$ since the relative frequency noise ϵ_Δ^2 scales as $|\Delta|^{-2}$. From the power-law fit we extract the normalized intensity spectral density: $2\pi\epsilon_I^2 = 0.2 \text{ kHz}^{-1}$ which is compatible with residual intensity noise from the resonant cavity frequency doubler. Based on these measurements we can focus on reducing any laser intensity fluctuations, using for example a feedback loop based on a photodiode and an AOM that controls the intensity. These results emphasize the importance of the Rydberg-dressed interferometer for characterization of decoherence properties and possible noise sources. Nevertheless, the dephasing rate remains small compared to the light shift over most of the measurement range. This can be quantified by the strong-coupling parameter $C = E_{LS}/(\Gamma_{\text{eff}} + X)$ that varies in the range $7 \leq C \leq 18$ as Δ is varied over the range ± 40 MHz.

6.4 Realization of a sensitive Rydberg dressed electrometer

Having characterized the performance of the Rydberg-dressed interferometer, we now assess its potential applications beyond characterization. As an example we consider the sensitivity of the Rydberg-dressed interferometer to static electric fields due to the second order Stark effect of the Rydberg state, where the polarizability of the bare clock states can be totally neglected. Maximizing the derivative of Eq. 6.7 with respect to small perturbations and assuming shot noise limited state readout we find a minimum single shot sensitivity (standard quantum limit) $\sigma = e(X + f_r\Gamma)/(f_r F \alpha \sqrt{N})$, where e is Euler's number, F refers to the bias electric field strength, N is the number of atoms used in the measurement and α is the electric polarizability of the Rydberg state (which scales with principal quantum number as n^7). In the fundamental limit when the noise is very small ($X \rightarrow 0$), the electrometer sensitivity is independent of the Rydberg state fraction. This shows that the Rydberg dressing approach allows for extremely small densities of the strongly interacting particles, while at the same time large overall atom numbers (N) can be used to minimize the atomic shot noise. Furthermore we estimate the ideal single shot sensitivity for the Rydberg state used in our experiment (having $\Gamma/2\pi = 5.6$ kHz and $\alpha_{39P}/2\pi = 10.25$ MHz cm²/V²) with $N = 10^5$ particles and applying a bias field $F = 1$ V/cm. We find the electrometer sensitivity to be $\sigma = 4.7$ μ V/cm which indicates that such Rydberg-dressed interferometer would rival the state-of-the-art electrometers [226, 227, 126, 228].

As a proof of principle, we now proceed to measure the sensitivity of the Rydberg dressed interferometer to electric fields. For these measurements we use the spin echo technique introduced at the beginning of this chapter (section 6.1.1). We use this particular approach instead of Ramsey interferometry to be less sensitive to dephasing of single atoms. In the experiment we use a spin echo RF pulse sequence consisting of two $\pi/2$ -pulses separated by two free evolution times of equal duration $T_{\text{echo}} = 5$ ms, with a π -pulse in between (see figure 6.2), while the UV dressing laser is applied continuously during both of the free evolution times. As a read out, we measure the population in the $|1\rangle$ state as a function of the final $\pi/2$ -pulse phase, which is varied from 0 to 4π using the RF DDS board (see section 3.2.2). The goal is to observe a differential phase accumulation due to any change between the first and the second evolution time. In the case the system remains the same during the two free evolution periods, no phase accumulation is observed, and the population oscillates with minima at 0, 2π and 4π .

In the case that the electric field is modified during the second part of the spin echo

pulse, one should expect a change in the phase since the π pulse cannot reverse completely the dephasing due to the presence of a different field. Experimentally, we use the deflection ring electrodes of the Rydberg detector (shown in figure 3.1), to change the electric field during the second free evolution part from $F_1 = 2.2 \text{ V/cm}$ to $F_2 = F_1 + \epsilon$. These electrodes are shielded by other 8 electrodes and thus the electric field magnitude we can apply is rather small. We compensate this by applying a bias electric field along the same direction of the ring electrodes field (F_1) which helps to improve the sensitivity of the Rydberg-dressed interferometer. We have previously calibrated the electric field generated by deflection ring electrodes, as it is shown in section 4.3.3.

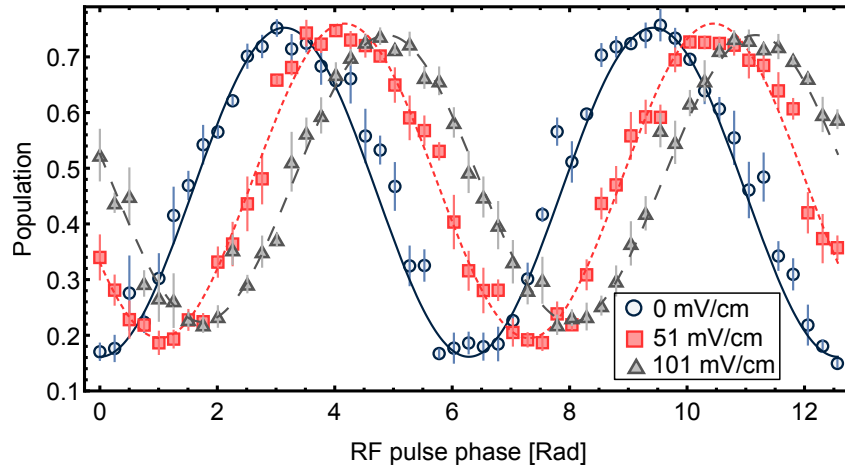


Fig. 6.8.: Electric field measurement with a Rydberg-dressed interferometer. Population in $|1\rangle$ is measured after a spin echo sequence as a function of the applied phase to the final $\pi/2$ RF pulse. We observe a clear phase shift when changing the electric field from $F_1 = 2.2 \text{ V/cm}$ to $F_2 = F_1 + 51 \text{ mV/cm}$ or $F_2 = F_1 + 101 \text{ mV/cm}$

Figure 6.8 shows the population as a function of the phase of the last RF pulse in the spin echo sequence, for three different electric field perturbations. The blue circles represent the simplest case where no electric field has been changed ($\epsilon = 0$), we observe a clear oscillation while varying the phase, which is centered around 2π . As soon as we apply a different electric field in the second pulse the population oscillation shifts with the phase (triangles and squares in figure 6.8). These demonstrates a clear dependence of the phase on the applied electric field, which corresponds to $0.022(1) \text{ rad/(mV/cm)}$.

We further study the sensitivity of our Rydberg-dressed electrometer to distinguish between two different electric fields (single shot sensitivity). In order to do that we set the phase to a constant value $\theta = 5.25 \text{ rad}$. We repeat the measurement of the population for 0 mV/cm and 51 mV/cm 200 times for each electric field. Based on these measurements we can extract a histogram of the occurrences of a population range, as shown in figure 6.9. The histogram clearly shows the two different electric field measurements well separated by three standard deviations. Furthermore, we

analyze the probability of being able to distinguish two of these measurements in a single shot with 66% chance, and extract the electrometer sensitivity in a single shot measurement as 17(1) mV/cm.

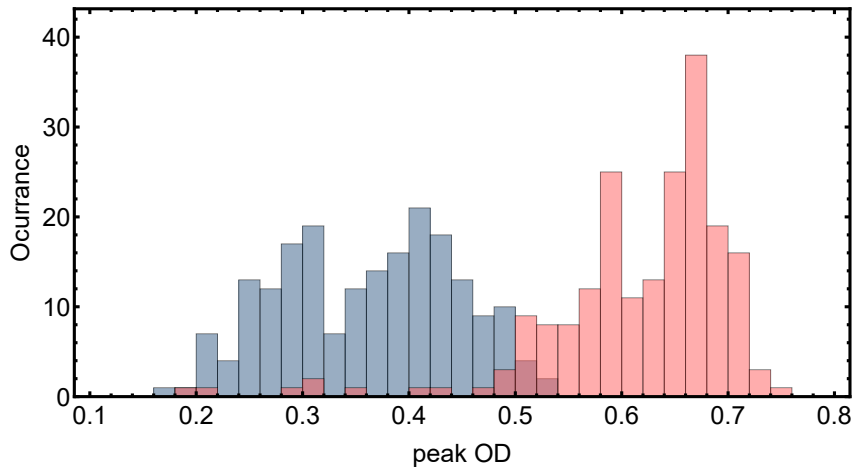


Fig. 6.9.: Determination for the Rydberg-dressed electrometer sensitivity. Histogram of two electrometry measurements ($\epsilon = 0$ mV/cm and 51 mV/cm) for 200 repetitions at fixed phase $\theta = 5.25$ rad. See text for further details.

6.5 Perspectives for the Rydberg-dressed interferometer

In conclusion we have realized and characterized the performance of an interferometer enhanced by Rydberg dressing. Based on Ramsey interferometry we could precisely determine the atom-light coupling, Rydberg state admixture and coherence properties of the dressed states. Furthermore, we show a direct application of the system to be used as a highly sensitive electrometer. The basic essence of our scheme – the controllable coupling of a highly-coherent two-level system to a third state with greatly enhanced sensitivity – can be applied to numerous quantum systems, even beyond the Rydberg atom platform. Thus this approach has the potential to greatly expand the number of atomic and molecular systems suitable for metrological applications and many-body physics.

While the present experiments were performed in an effectively non-interacting situation, Ramsey interferometry can serve as a powerful method to characterize atomic interactions [82, 81, 83, 85, 80]. Rydberg dressing provides a way to induce and control these interactions, thereby introducing a tunable nonlinear evolution between the clock states. This would provide another route to generating squeezed or entangled many-body states without relying on low-energy collisions between the atoms [229, 230, 231, 103], or the implementation of nonlinear quantum metrology protocols [232, 233] for surpassing the standard quantum limit. Alternatively, the

Rydberg-dressed interferometer could provide a way to optimize Rydberg-dressing protocols [65, 53, 80, 79], even in the limit of extremely weak interactions, enabling the realization of robust quantum logic gates and quantum spin systems [146, 234, 44, 235], or novel long-range interacting quantum fluids [236, 237] and lattice gases with beyond nearest neighbor interactions [238, 239, 240].

Conclusion

In the course of this thesis, we have built a new experimental setup based on ultracold potassium atoms and studied their excitation to strongly interacting Rydberg states. More specifically this work has focused on the complex non-equilibrium dynamics and coherence properties of optically trapped gases under continuous laser excitation. These have been shown to give rise to a rich non-equilibrium phase structure, and novel self-organizing dynamics. While these first experiments concern effectively classical dynamics (due to strong dephasing), in parallel I have also developed a tool based on interferometry combined with off-resonantly Rydberg excitation, which can be used to characterize coherence effects in strongly interacting many-body systems and to extend our experimental studies to the quantum regime.

In the first part of this thesis, I have shown the main characteristics of our ultracold potassium experiment that allows us to manipulate the atoms in terms of their ground state, spatial confinement and temperature. The ultracold setup includes an adaptable laser system for cooling and trapping, which can be easily adjusted for either ^{39}K or ^{40}K . We implemented the technique of gray molasses cooling and with it achieved temperatures down to $20\mu\text{K}$ (far below the Doppler temperature), making it possible to directly load an optical trap, where all the experiments for this thesis took place. Additionally we have implemented a set of techniques (e.g. magnetic field nulling, radio-frequency state transfer and optical pumping) to be able to prepare the atomic sample in a specific ground state with very high purity. All together the experimental setup is quite complex, therefore, to control the experimental machine and to read out and analyze the data, I have implemented a Labview control program. This covers all the current experimental requirements, enabling precise timing of dozens of analog and digital devices, reproducible experiments and large scale automatic data taking, but it is also easily extendable to include new devices for future updates. The combination of a highly controllable ultracold potassium experiment with a versatile Rydberg excitation laser, have allowed us to create a platform for studying non-equilibrium phenomena based on the driven-dissipative behavior of the Rydberg system.

Having prepared the ultracold atomic samples, we then needed to excite the atoms to high lying Rydberg states. For this, I have set up a laser system, adaptable for either one or two-photon Rydberg excitation schemes, making it possible to

access a wide variety of different Rydberg states. I characterized in great detail the laser system used for two-photon excitation, i.e. the frequency doubled laser with a titanium sapphire gain element operating at a wavelength of 456 nm used in conjunction with our existing semiconductor lasers at 767 nm. Its key characteristics are a maximum output power of 1.5 W, a frequency noise of 115(9) kHz and long term frequency stability better than 42 kHz drift per hour. To benchmark the laser, I performed measurements of atom loss in a magneto-optical trap to characterize the laser tunability and measure the quantum defects of potassium Rydberg states with $n > 77$. Later in my thesis work, I changed the laser gain medium to a dye jet (rhodamine 6G) and installed a new frequency doubling cavity. With this we could also demonstrate the new capability to excite Rydberg atoms via single photon transitions, thereby eliminating complications associated to the short lived intermediate 4P state. The most remarkable characteristic is the relatively high power at 286 nm, up to 300 mW, which is suitable for Rydberg dressing experiments.

Having built the Rydberg platform, we performed a detailed characterization of the driven Rydberg system, where, depending on the influence of the laser driving, dissipation and long-range interactions, the system was anticipated to exhibit different types of behavior, such as magnetically ordered states (where the ground and Rydberg states form a pseudo-spin-1/2 system). We were able to investigate all these regimes over a wide range of laser parameters, i.e. intensity (related to the Rabi frequency Ω) and detuning from resonance Δ . In these experiments we established a simple yet powerful way to characterize the system by the rate of population loss. Surprisingly, we found that the loss rate exhibited apparent power-law scaling with different exponents over a wide range of parameters. Furthermore, the different exponents obtained reflected different regimes of the non-equilibrium phase structure of the many-body system, which included dissipation dominated, paramagnetic, critical and unstable regimes.

One particularly striking feature was found above resonance, where we have discovered power law scaling with a larger exponent than expected for single particle excitation, which was not captured by the corresponding mean-field phase diagram. This scaling is now understood to be a consequence of Rydberg facilitation processes, where a single seed excitation tunes neighboring atoms into resonance leading to the formation of large excitation clusters. To improve our understanding of the off-resonantly driven Rydberg gas, we have performed in this regime additional experiments to study the long term dynamical evolution. We discovered a particularly striking nonlinear dependence of the atomic density behavior: regardless of the initial state and when above a critical density, the system always evolves towards the same quasi-stationary state. Furthermore we found that the quasi-steady state density, as a function of the driving amplitude Ω , exhibits scale invariance over a wide range of initial densities and driving strengths, with a scaling exponent of

$\beta = 0.910(4)$. This led us to the conclusion that the system exhibits signatures of self-organized criticality. To test this hypothesis, we performed additional experiments to investigate the system's response to perturbations by suddenly changing the driving and measuring the new quasi-steady state density, which shows a critical response whenever the system is prepared above a characteristic density, but is independent of the precise value of the density. These experimental results were then supported by a non-equilibrium field theory which qualitatively describes the data, confirming self-organized criticality (SOC) as the mechanism governing the dynamics of our driven open many-body system.

To a surprisingly large extent, our results on the non-equilibrium phase structure and self-organizing dynamics of the driven Rydberg system could be described by effectively classical dynamics (i.e. mean field, rate equation and Langevin equation models). One possible reason for this is the relatively large dephasing rate in our experiment which we attributed to laser frequency fluctuations, combined with the long timescales accessed in our experiment. To study this in more detail, I have implemented a methodology to quantify the coherence properties of Rydberg-dressed states, with the goal to identify the dominant decoherence processes and to enhance coherence times. This technique, a Rydberg-dressed interferometer, combines the high level control of the ground state atoms with the effective detuned excitation to a Rydberg state by dressing one state of a clock transition. This combination results in a high precision interferometer with enhanced sensitivity to atom-light coupling, Rydberg interactions and external fields. In a first application, I demonstrated that the interferometer can be used to characterize the main properties of the Rydberg dressed system, including a direct measurement of the key parameter, the coupling strength $\Omega/2\pi = 163(1)$ kHz. By modeling the expected interferometry signal with a quantum master equation that included dissipation and dephasing terms through laser intensity and frequency noise, we could extract from the interference pattern the population decay and the pure dephasing rate. The maximum dephasing rate on resonance was 1 kHz, which fell off as a function of detuning with Δ^{-2} . Based on this, we could identify the principal source of decoherence as the laser intensity fluctuations (rather than frequency noise), which is something that can be readily improved for future experiments. As an unexpected outcome, we discovered that the Rydberg-dressed interferometer could function as a sensitive electrometer for detecting weak static electric fields. Taking advantage of the high sensitivity of Rydberg atoms to those fields, we used our Rydberg-dressed system to precisely measure an applied electric field, where a change in the field can be observed in the interference signal. We have repeated these measurements two hundred times and determine the single shot sensitivity to be 17 mV/cm, with a fundamental sensitivity limit of $1\mu\text{V}/\text{cm}$, which makes the Rydberg-dressed electrometer competitive with the best existing electric field sensors.

These experimental results have opened new questions, and highlighted new opportunities for further studies. For example, our platform allowed us to determine the scaling exponent related to the SOC behavior observed in our system, however so far we have been unable to relate the measured exponent to any known universality class. Therefore it is relevant for future experiments to measure other observables in the system and extract their critical exponents, which could aid in extracting the underlying non equilibrium universality class. A crucial observable in the SOC dynamics is avalanches, in the sense of a perturbation of the critical state which triggers an avalanche-like process. Studying this observable and its corresponding scaling with avalanche sizes, would serve to make more concrete connections to known SOC models. This can possibly help to identify the corresponding universality class and whether it is related to other paradigmatic non-equilibrium universality classes, such as directed percolation [166].

Another direction for future experiments, concerns the coherence properties measured with our Rydberg-dressed interferometer, and the conclusion that intensity noise of the dressing laser is the main contribution to the system's dephasing. These experiments were performed at rather low densities, and it is not clear if this conclusion still holds at higher densities, or when other effects (e.g. atomic motion and disorder) can also affect the system's coherence and at which scale. In terms of coherence times, we are still several orders of magnitude away from the fundamental limit, set by the spontaneous decay of the Rydberg states. But assuming we can approach this limit, there are many new research opportunities, for example, concerning how the non-equilibrium phase structure and dynamics is modified in the presence of quantum fluctuations. Relatively little is understood in this limit, however recent theoretical work has suggested that the second order absorbing state phase transition studied in chapter 5 could change to a first order one [78], making it possible to study other aspects of non-equilibrium phase transitions at the interface of classical and quantum regimes.

As a first step towards addressing these challenges and open questions, we have recently updated our experiment to allow for a better control over the spatial confinement, the atomic motion and the spatially resolved detection of the atoms. We are currently able to cool down atoms to a few tens of nK, and trap them in geometries such as tubes, ring structures and 2D lattices. Figure 7.1, shows two exemplary images of the ground state atoms in different trap geometries. Combining these techniques will allow us to disentangle the roles of atomic motion, disorder, and decoherence from the excitation dynamics responsible for complex non-equilibrium behavior, and to perform experiments in different dimensionalities. Furthermore, using these traps we have designed a high resolution imaging system [168] which we could employ to study other key characteristics of the system associated to non-equilibrium phase transitions and self-organized criticality, such as spatio-temporal

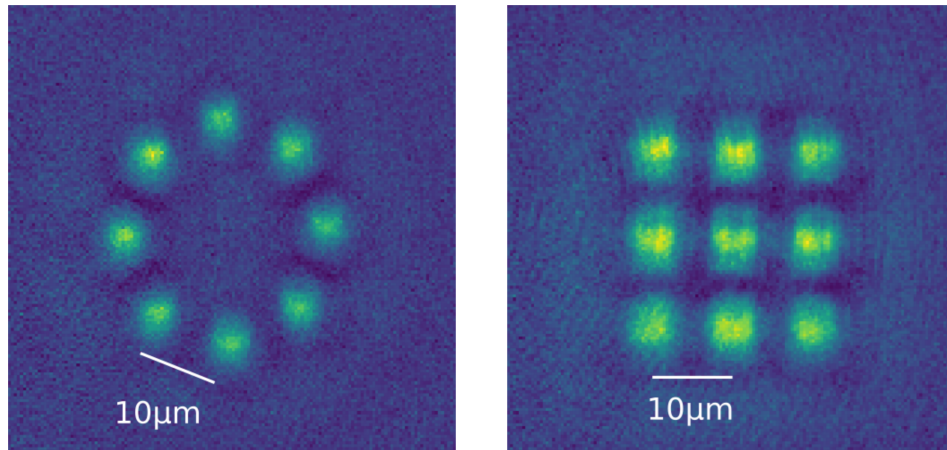


Fig. 7.1.: First results on the geometry and motional control of the atoms. Absorption images of potassium atoms trapped in different geometries.

correlations. In a similar way we could study the dynamical behavior that results in a self-organized critical system, for example by deterministically exciting the Rydberg atom seed, which enables the facilitation, and detecting how the excitation spreads, which could aid to measure avalanches in the system. Such studies would help to elucidate the connection between the microscopic dynamics and the macroscopic observables of the complex many-body system.

In conclusion, the results I presented in this thesis, together with the recently added capabilities in our setup, open new prospects. Our experiment offers a general framework for understanding non-equilibrium matter, spanning both classical and quantum regimes, as well as new technologies which can exploit the strong interactions between Rydberg atoms to realize quantum enhanced sensors.

Appendices

An adaptable program for experimental control and analysis

This appendix is dedicated to Tobias, I wish you all the best with Labview :)

Here we explore in more detail the characteristics of our experimental control, which is designed based in four criteria:

- An independent structural program such that new devices can be easily implemented, this is crucial since our experiment is growing and needs new capabilities with time.
- Flexibility to adjust the experimental sequence including all relevant parameters and also devices, which should be able to be deactivated, activated or used in different parts of the sequence.
- Automation of processes should be possible, for example repeat continuously a sequence or scan a parameter with a different value in each sequence.
- The acquired data from the measurement should be properly saved and also all the devices characteristics and parameters of the sequence such that the exact configuration can be recovered anytime.

In our case we base our program in a well-known programming language for experimental physics, Labview. This has the advantage of a higher level programming structure, i.e. it does not required to program the low-level hardware commands. Especially since most of the hardware use in ultracold atom experiments come with labview programs to interface the device, such a hardware programming is not necessary. Additionally Labview offers a widely expandable user interface making it easy to operate the program without relying on knowing every detail of the code. Furthermore, this programming language allows for parallel control of the hardware, which is very handfull for example to control the imaging beam while taking a picture at the same time with the camera. The first version of this experimental control program was developed in the group of prof. Matthias Weidemüller, within a master thesis project. Further programming like the inclusion of new camera devices and utilities, new logic box hardware and data saving facilities, have been done within

this thesis.

A.1 Labview program modular structure

Labview is an user oriented program based on a visual programming language. It implements user interfaces directly into the developing code and is based mainly on virtual instruments (VIs) which are subroutines with adjustable inputs and outputs. Labview additionally offers all the facilities for object oriented programming via the *Actor Framework*. Its general principle is that the whole program can be structured in independent parts (referred as actors) that work separately and can communicate with each other through messaging queues. This is very convenient for our purposes since we can use an actor for each type of device or task (what we call module), and utilize a couple of actors to manage those modules.

Another important feature offered by Labview in the *Actor Framework* is that actors can inherit from another actor, i.e. when creating a new actor this can have the same functions (VIs) as the actor it is inheriting from. We use this property for all the modules such as there is a base module with all the minimum VIs required for a module to work, and every module in the experiment will inherit those VIs and adapt them to the specific requirements of the module.

The main VIs that each module should inherit from the base module are: the *Actorecore.vi* which corresponds to the user interface for the specific module, the *init.vi* which is the subroutine to initialize the module, such as the hardware connection. The *prepare.vi* is the function to set the necessary parameter values before the sequence is run. The *save.vi* has the function to save all the attributes of the module in a file which is used for recovering the module when needed. Finally, the *run.vi* is the main function carried out by the module that need to be executed when the command "run" is received. Given these VIs, each module can adjust any of them according to its functionality, for example a camera module should take images in the *run.vi* while the image analysis module should fit a 2D Gaussian function to the atom cloud image.

To control all the modules (specific devices and tasks) another actor is used: the *module manager*. This actor is meant to create, delete, activate, deactivate and handle the messages between the modules. This allows for more flexibility, such that we do not required all modules to be active all the time to run the experiment. For example during adjusting phases it is not necessary to save absorption images into the hard disk, the module can be turned off during this period, saving space in the hard disk. This module independence is further developed via the communication

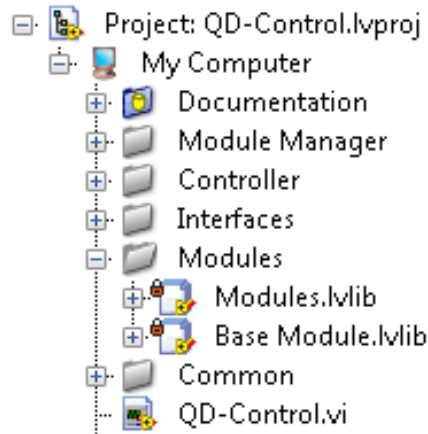


Fig. A.1.: General structure of the experimental control program. The module manager controls all the modules (devices and tasks in the experiment). The controller includes a variable controller to determine the values of all variables in the experiment and a run controller to organize the order in which the modules are prepared and run. The interfaces contains the designed user interface. The modules folder includes all the main VIs to run a module. finally, the QD-Control.vi is the main program, required to run to create all the different instances in the experimental program.

between modules. The module manager receives and sends the messages from the modules such that there is not direct communication between specific modules, in this way if a module is not activated the communication does not get interrupted.

The structure of the program is revealed in figure A.1. The different folders show the main components of the program: the already mentioned *Module manager*, the *controller* (explained in detail bellow), the *interfaces* which contains all the VIs regarding the elements that can be adapted by the user to create its own interface, i.e. the location of each module interface in the main program interface. The *modules* which corresponds to all the modules already programmed including the *Base Module* from where all other modules inherit.

Besides the *module manager* other two actor objects have been created: the controllers, shown in figure A.1. The first one is the *run controller* which takes care of the order in which the modules are prepared and run, since not all the modules should run in parallel. For example the image analysis module should run after the images are acquired, i.e. after the camera module is run. The second actor object is the *variable controller*, which manages the values of all variables use in the experiment. This is particularly useful to scan a parameter in the experiment such as a laser frequency or a beam power. The variable value can be changed every run either in a linear fashion, a logarithmic one or a double ramp where the variable is scanned from the initial to the final value and then backwards. Figure A.2 shows

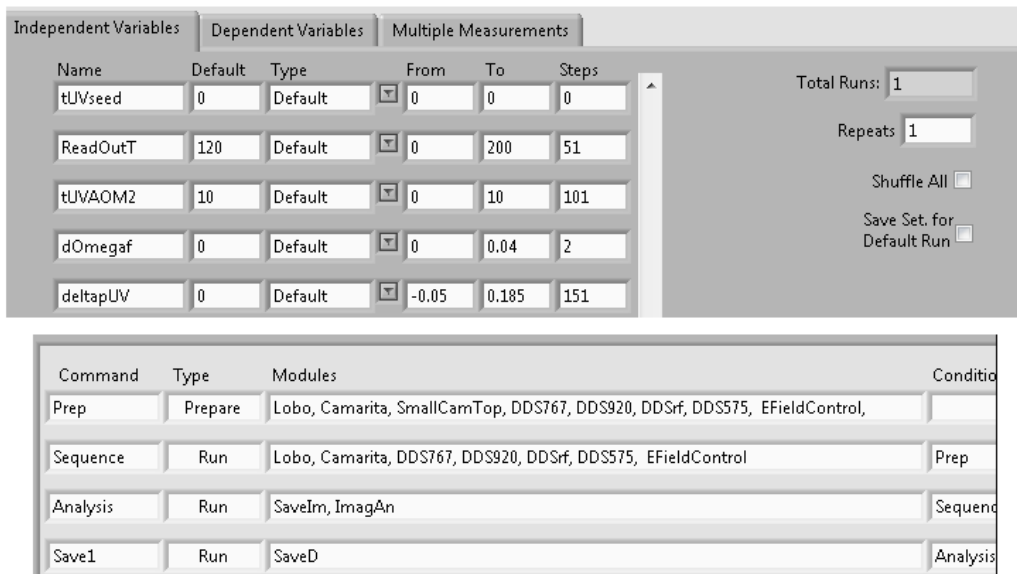


Fig. A.2.: The variable controller and run controller. The upper panel shows the interface of the *variable controller*, where a list of all variables are shown. Depending of the type of attribute (third column) the variable can have always the same value (Default) during a scan or it can change every run. The lower panel shows the *run controller* interface. It is mainly a list with the order in which the modules have to be prepare and run.

an example of both controllers interfaces. The variable controller has an additional functionality: multiple measurements, where many scans of different variables can be set to run.

Besides the internal structure of modules, module manager and controllers, the program has an extra dynamical component. This consists on an active loading of the modules every time the program is launched. This has the advantage that depending on the instruments and tasks required for the experiment, it is possible to choose to load only certain modules. For example while testing an specific device, it is not required to have all the devices connected or in the case that a new setup is used where less modules are required this would avoid the time consuming task of installing drivers for devices that are not used. The way the program is dynamically loaded is by reading a simple text file with a list of the modules that are to be used in the experiment.

The main VI that loads and connects all the necessary elements for running the experimental control program is the "QD-Control.vi", the corresponding user interface is depicted in figure A.3. It includes the commands to start or stop a run, to load a specific configuration (including all the parameters of the modules) and to save the current sequence. Additionally below the start run button a list of all types of run can be displayed to choose the run mode. This includes: a default run mode

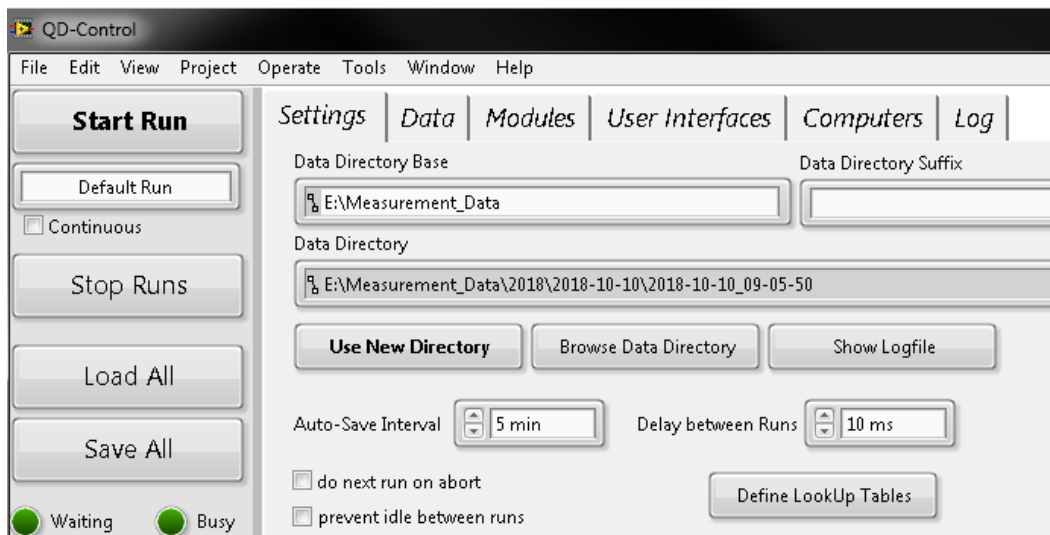


Fig. A.3.: Main window of the experimental control program. The left column shows a set of buttons to start, stop, load and save the experimental sequence. The right panel contains the basic settings to determine the folder where the data has to be saved.

where all variables are fixed to its default value, a controlled run mode where all the variables selected as "linear", "logarithmic" or "tomo" are scanned within the given range values (see variable controller in figure A.2), and a multiple run mode, to do many scans of different variables one after the other.

The right panel in the main interface shown in figure A.3 has a set of different tabs that control or show all the relevant attributes in the program. The settings tab include all the parameters to create and use the directory where the data has to be saved. The data tab shows the data (name and type) that is controlled and distributed by the module manager, showing values like the fitted parameters from the image analysis. The modules tab is mainly the interface of the module manager. This includes a list of all the created modules, their respective type, location within the user interface and whether it is activated or not. Within this tab is possible to create new modules or delete the existing ones. The user interfaces tab is used to create a new interface based on one of the existing interface templates. The computers tab is a module to log and control other computers with the same experimental program, one being the master computer and the rest the slaves. This can be used to trigger a parallel program that can be focused only in one device or task, e.g. image analysis or oscilloscope read out. The last tab log shows all the logging details of the specific computer.

A.2 Modules: the principal devices and tasks in the experimental control program

In this section we present other modules, besides the logic box, which are constantly used in our experiment and were implemented or further developed within this thesis.

Absorption and fluorescence imaging: camera module. As stated in the introduction of this chapter, one of the most important requirements for an ultracold system is the precise detection of particles. Imaging is one of the most common used techniques to study ultracold gases, in our case we implement two types of imaging: absorption and fluorescence.

Absorption imaging is based on a resonant beam that is sent to the atom cloud, such that the atoms will absorb the light, creating a shadow that is detected by a camera. This technique requires a perfect timing between the imaging pulse and the camera trigger set to record the image. The precise timing can be achieved by using the logic box to send a trigger to the AOM that controls the imaging beam and another trigger to the camera. After having taken the image, we proceed to the analysis of the atom sample, as shown in the next section.

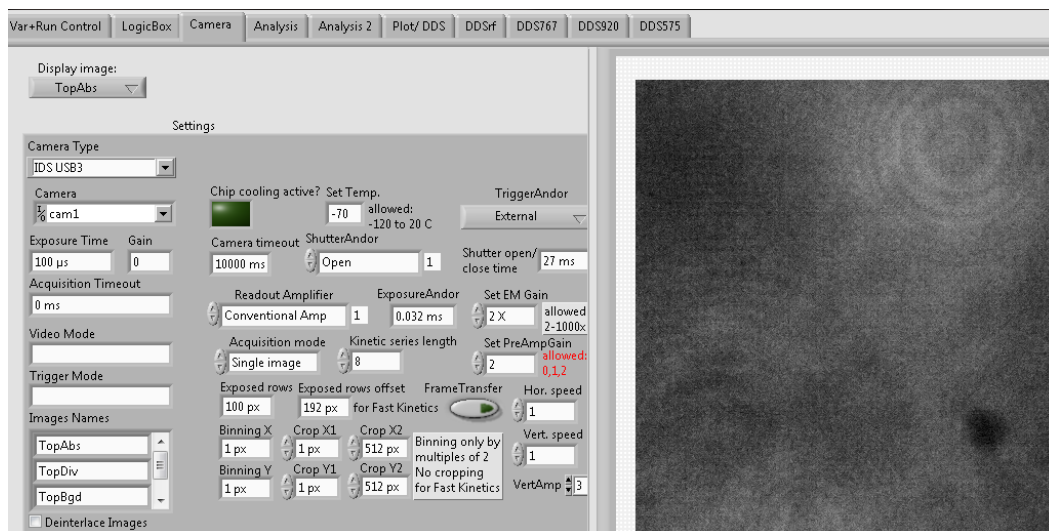


Fig. A.4.: Module designed to control all the cameras in the experiment. The camera type can be chosen in the menu on the left, depending on the camera only some parameters in the menu are used. The list of image names indicates the amount of images the camera should take, this is the number of trigger signals the camera waits for.

The second imaging technique, fluorescence, is performed by collecting the scattered photons from the atom cloud, while shining into the atoms a beam close in frequency

to a transition. In order to collect a considerable amount of photons the imaging can only be done by a detuned cycling transition. In our case we use both cooling and repumping beams for this purpose, where we require again the adequate triggering to set the camera and the beams at the correct time.

Depending on the imaging requirements we make use of different cameras. In the case of simple diagnostics of the atomic cloud either in the MOT or in the ODT, we use the IDS camera¹, which is a compact camera based on a CMOS (complementary metal-oxide semiconductor) sensor. For a more specialized case such single atom imaging (see section Figure 3.1.3) we make use of the Andor camera², which has an EMCCD (electron multiplying charge-coupled device) detector with a quantum efficiency of $\sim 85\%$ at the desired wavelength (770 nm).

The software used for both cameras naturally differ. Within this thesis the camera module has been upgraded to be able to use these two extra types of cameras. Since each camera device have a different set of parameters that can be tuned and the hardware in general needs to be initialized and run differently, we included in the interface the possibility of choosing the type of camera. This acts as an attribute in the program that can be consulted anytime the module executes one of the VIs. Depending on the value of the attribute the program would perform the task accordingly. This facility can be further used in case a new type of camera should be included, it just have to add in each subroutine and extra case for the new camera device.

More specifically a common user interface (shown in figure A.4) was created with the typical parameters that can be set in a camera, such as the exposure time, and other specific parameters for the more complex camera (Andor), like the temperature. The user can create as many copies of the module as needed and select the camera to be used, depending on the experiment. The cameras can be used also at the same time just keeping in mind that each one requires a unique trigger signal, generated by the LB and connected physically to the specific camera.

Analysis module for the imaging. Using the images taken by the cameras, one can inferred different properties of the atoms such, the atom number, density or cloud size. In order to obtain information about the cloud from the absorption image we take two additional images: one with the imaging beam only (no atoms present) and another one with out any light or atoms(called dark image). Using these extra images one can subtract the background noise inherent to the camera and compare the image with the atoms and without them. The final image to be analyzed is calculate as:

¹IDS, Imaging Development Systems. UI-3240ML-NIR-GL

²Andor iXon Ultra 897 UCS-Exf

$$Im = \frac{I_{abs} - I_{dark}}{I_{light} - I_{dark}} \quad (\text{A.1})$$

This resulting image can be used to extract all the atom cloud parameters as explain in the following. We start by assuming a two-level system (representing an atom) interacting with the imaging beam which intensity is below the saturation intensity. The atom number density ($n(x, y)$) can be related to the absorbed intensity via the Lambert-Beer's law:

$$I(x, y, z) = I_0(x, y) \exp(-OD(x, y)), \quad (\text{A.2})$$

where the beam is assumed to propagate in the z-direction, I_0 is the original intensity of the beam and $OD(x, y) = \sigma_{abs,0} \int_{-\infty}^{\infty} n(x, y, z') dz'$ the optical density, with $\sigma_{abs,0}$ the absorption cross section of the transition. From equation A.2 we can relate the OD to the actual images we take in the experiment, since I_0 corresponds to $I_{light} - I_{dark}$ and $I = I_{abs} - I_{dark}$, therefore the optical density can be extracted as:

$$OD(x, y) = -\ln \left[\frac{I}{I_0} \right] = -\ln [Im] \quad (\text{A.3})$$

For a non-interacting atomic cloud (relatively low densities) the atoms distribute thermally in the trap, leading to a Gaussian distribution of the atoms and therefore the optical density, such that:

$$OD(x, y) = OD_0 \exp \left(-\frac{x^2}{2\sigma_x^2} - \frac{y^2}{2\sigma_y^2} \right), \quad (\text{A.4})$$

with σ_i the cloud size in the i th direction. By fitting a 2D Gaussian function to the image, we can extract the cloud size parameters, the peak optical density (OD_0) and the atom number.

An additional module was created to manipulate the images and extract from the final image (Im) all the relevant atom cloud parameters. We include in the 2D Gaussian fit an feature that can be adjusted if one wants to include an offset in the image or a rotation of the fit plane (in case the cloud is tilted). Figure A.5 shows the absorption imaging module with a typical image all ready processed and the obtained atom cloud values from the fit, which is performed within the experimental sequence, allowing for live analysis. The fits however do not work properly from

time to time, and therefore are only reliable to quickly check the response of the atoms given the experiment. For further analysis we save the row images to do post processing analysis, as explained in the next section.

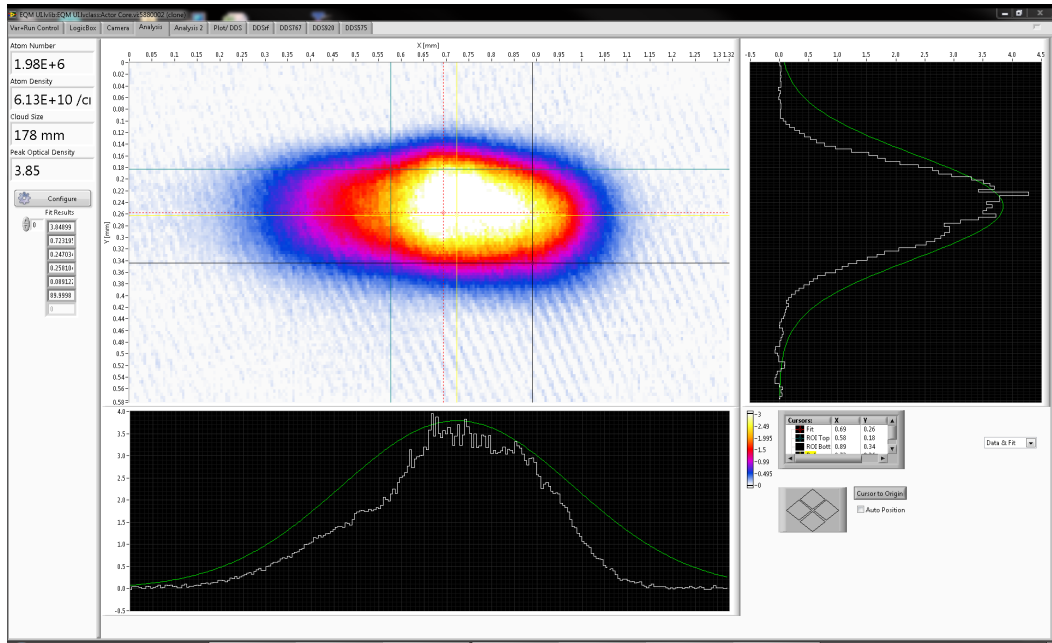


Fig. A.5.: Absorption image module. Live image analysis is performed using this module, where most of the atomic cloud parameters can be extracted from a 2D Gaussian fit (further explanation in the text).

Data saving: results and high resolution images. The module for imaging analysis it is used as a diagnostics platform to perform a fast checking of the results. In order to further manipulate and analyze the data we have created to new modules for data saving. The first module (called *SaveData*) saves after each run the all the variable values, the ADC read data and the fit parameters from the live image analysis. all this is combined and saved in a csv file within the folder define by the user in the main program window (see figure A.3). This module does not required a user interface since the file name is set as a constant and the file path is an attribute of the module. The saved data has a simple format to be read by a plotting program, useful in case of scans in order to plot the fit values against the scan variable.

The second module has been developed to save the row images taken by the camera to analyze the images after the measurement is finished. It can be that the live imaging analysis does not fit properly from time to time, making the results noisier than they actually are. Within the post-processing one can filter the images, remove fringes or crop the image to select and better fit only a part of the image. All the row images are saved every run under the name given to the image in the camera module (see fig. A.4) and the run number, in this way every set of images per run is related to the variable values which are also saved per run.

Bibliography

- [1] Pyotr Kapitza. Viscosity of liquid helium below the λ -point. Nature, 141(3558):74, 1938.
- [2] John F Allen and AD Misener. Flow of liquid helium ii. Nature, 141(3558):75, 1938.
- [3] Philippe Nozières and David Pines. The theory of quantum liquids, vol. ii. Superfluid Bose Liquids, 1990.
- [4] H Kamerlingh Onnes. Further experiments with liquid helium. In Proceedings of the KNAW, volume 13, pages 1910–1911, 1911.
- [5] H Kamerlingh Onnes. Further experiments with liquid helium g. on the electrical resistance of pure metals etc. vi. on the sudden change in the rate at which the resistance of mercury disappears. Koninklijke Nederlandse Akademie van Wetenschappen Proceedings Series B Physical Sciences, 14:1911–1912, 1911.
- [6] Fritz London and Heinz London. The electromagnetic equations of the superconductor. Proc. R. Soc. Lond. A, 149(866):71–88, 1935.
- [7] J. Bardeen, L. N. Cooper, and J. R. Schrieffer. Theory of superconductivity. Phys. Rev., 108:1175–1204, Dec 1957.
- [8] Richard P Feynman. Simulating physics with computers. International journal of theoretical physics, 21(6-7):467–488, 1982.
- [9] Seth Lloyd. Universal quantum simulators. Science, 273(5278):1073–1078, 1996.
- [10] J. I. Cirac and P. Zoller. Quantum computations with cold trapped ions. Phys. Rev. Lett., 74:4091–4094, May 1995.

- [11] Rainer Blatt and David Wineland. Entangled states of trapped atomic ions. Nature, 453(7198):1008, 2008.
- [12] H. Häffner, C.F. Roos, and R. Blatt. Quantum computing with trapped ions. Physics Reports, 469(4):155 – 203, 2008.
- [13] Emanuel Knill, Raymond Laflamme, and Gerald J Milburn. A scheme for efficient quantum computation with linear optics. nature, 409(6816):46, 2001.
- [14] Benjamin P Lanyon, James D Whitfield, Geoff G Gillett, Michael E Goggin, Marcelo P Almeida, Ivan Kassal, Jacob D Biamonte, Masoud Mohseni, Ben J Powell, Marco Barbieri, et al. Towards quantum chemistry on a quantum computer. Nature chemistry, 2(2):106, 2010.
- [15] M. A. Broome, A. Fedrizzi, B. P. Lanyon, I. Kassal, A. Aspuru-Guzik, and A. G. White. Discrete single-photon quantum walks with tunable decoherence. Phys. Rev. Lett., 104:153602, Apr 2010.
- [16] Immanuel Bloch, Jean Dalibard, and Sylvain Nascimbene. Quantum simulations with ultracold quantum gases. Nature Physics, 8(4):267, 2012.
- [17] Andrea Micheli, GK Brennen, and Peter Zoller. A toolbox for lattice-spin models with polar molecules. Nature Physics, 2(5):341, 2006.
- [18] Yuriy Makhlin, Gerd Schön, and Alexander Shnirman. Quantum-state engineering with josephson-junction devices. Rev. Mod. Phys., 73:357–400, May 2001.
- [19] Michel H. devoret and John M. Martinis. Implementing qubits with superconducting integrated circuits. Quantum Information Processing, 3(1):163–203, Oct 2004.
- [20] John Clarke and Frank K Wilhelm. Superconducting quantum bits. Nature, 453(7198):1031, 2008.
- [21] I. M. Georgescu, S. Ashhab, and Franco Nori. Quantum simulation. Rev. Mod. Phys., 86:153–185, Mar 2014.
- [22] William D Phillips. Nobel lecture: Laser cooling and trapping of neutral atoms. Reviews of Modern Physics, 70(3):721, 1998.

- [23] Christian Gross and Immanuel Bloch. Quantum simulations with ultracold atoms in optical lattices. *Science*, 357(6355):995–1001, 2017.
- [24] D. Jaksch, C. Bruder, J. I. Cirac, C. W. Gardiner, and P. Zoller. Cold bosonic atoms in optical lattices. *Phys. Rev. Lett.*, 81:3108–3111, Oct 1998.
- [25] Markus Greiner, Olaf Mandel, Tilman Esslinger, Theodor W Hänsch, and Immanuel Bloch. Quantum phase transition from a superfluid to a mott insulator in a gas of ultracold atoms. *nature*, 415(6867):39, 2002.
- [26] Michael Köhl, Henning Moritz, Thilo Stöferle, Kenneth Günter, and Tilman Esslinger. Fermionic atoms in a three dimensional optical lattice: Observing fermi surfaces, dynamics, and interactions. *Phys. Rev. Lett.*, 94:080403, Mar 2005.
- [27] Belén Paredes, Artur Widera, Valentin Murg, Olaf Mandel, Simon Fölling, Ignacio Cirac, Gora V Shlyapnikov, Theodor W Hänsch, and Immanuel Bloch. Tonks–girardeau gas of ultracold atoms in an optical lattice. *Nature*, 429(6989):277, 2004.
- [28] Toshiya Kinoshita, Trevor Wenger, and David S. Weiss. Observation of a one-dimensional tonks-girardeau gas. *Science*, 305(5687):1125–1128, 2004.
- [29] Zoran Hadzibabic, Peter Krüger, Marc Cheneau, Baptiste Battelier, and Jean Dalibard. Berezinskii-Kosterlitz-Thouless crossover in a trapped atomic gas. *Nature*, 441:1118–1121, 2006.
- [30] Richard J. Fletcher, Martin Robert-de Saint-Vincent, Jay Man, Nir Navon, Robert P. Smith, Konrad G. H. Viebahn, and Zoran Hadzibabic. Connecting berezinskii-kosterlitz-thouless and bec phase transitions by tuning interactions in a trapped gas. *Phys. Rev. Lett.*, 114:255302, Jun 2015.
- [31] P. A. Murthy, I. Boettcher, L. Bayha, M. Holzmann, D. Kedar, M. Neidig, M. G. Ries, A. N. Wenz, G. Zürn, and S. Jochim. Observation of the Berezinskii-Kosterlitz-Thouless phase transition in an ultracold Fermi gas. *Phys. Rev. Lett.*, 115:010401, Jun 2015.
- [32] C. A. Regal, M. Greiner, and D. S. Jin. Observation of Resonance Condensation of Fermionic Atom Pairs. *Phys. Rev. Lett.*, 92(4):040403, 2004.
- [33] M. W. Zwierlein, C. A. Stan, C. H. Schunck, S. M. F. Raupach, A. J. Kerman,

and W. Ketterle. Condensation of Pairs of Fermionic Atoms near a Feshbach Resonance. Phys. Rev. Lett., 92(12):120403, 2004.

- [34] J. Kinast, S. L. Hemmer, M. E. Gehm, A. Turlapov, and J. E. Thomas. Evidence for Superfluidity in a Resonantly Interacting Fermi Gas. Phys. Rev. Lett., 92(15):150402, 2004.
- [35] T. Bourdel, L. Khaykovich, J. Cubizolles, J. Zhang, F. Chevy, M. Teichmann, L. Tarruell, S. J. J. M. F. Kokkelmans, and C. Salomon. Experimental Study of the BEC-BCS Crossover Region in Lithium 6. Phys. Rev. Lett., 93(5):050401, 2004.
- [36] C Chin, M Bartenstein, A Altmeyer, S Riedl, S Jochim, J Hecker Denschlag, and R Grimm. Observation of the pairing gap in a strongly interacting Fermi gas. Science, 305(5687):1128–1130, 2004.
- [37] D. Jaksch, J. I. Cirac, P. Zoller, S. L. Rolston, R. Côté, and M. D. Lukin. Fast quantum gates for neutral atoms. Phys. Rev. Lett., 85:2208–2211, Sep 2000.
- [38] M D Lukin, M Fleischhauer, R Cote, L M Duan, D Jaksch, J I Cirac, and P Zoller. Dipole blockade and quantum information processing in mesoscopic atomic ensembles. Phys. Rev. Lett., 87:037901, 2001.
- [39] E Urban, Todd A Johnson, T Henage, L Isenhower, DD Yavuz, TG Walker, and M Saffman. Observation of rydberg blockade between two atoms. Nature Physics, 5(2):110, 2009.
- [40] Alpha Gaëtan, Yevhen Miroshnychenko, Tatjana Wilk, Amodsen Chotia, Matthieu Viteau, Daniel Comparat, Pierre Pillet, Antoine Browaeys, and Philippe Grangier. Observation of collective excitation of two individual atoms in the rydberg blockade regime. Nature Physics, 5(2):115, 2009.
- [41] R. M. W. van Bijnen and T. Pohl. Quantum magnetism and topological ordering via Rydberg dressing near förster resonances. Phys. Rev. Lett., 114:243002, Jun 2015.
- [42] Alexander W Glaetzle, Marcello Dalmonte, Rejish Nath, Christian Gross, Immanuel Bloch, and Peter Zoller. Designing frustrated quantum magnets with laser-dressed Rydberg atoms. Phys. Rev. Lett., 114(17):173002, 2015.
- [43] H. Labuhn, D. Barredo, S. Ravets, S. De Léséleuc, T. Macrì, T. Lahaye, and

- A. Browaeys. Tunable two-dimensional arrays of single rydberg atoms for realizing quantum ising models. Nature, 534(7609):667, 2016.
- [44] J. Zeiher, J. Choi, A. Rubio-Abadal, T. Pohl, R. van Bijnen, I. Bloch, and C. Gross. Coherent many-body spin dynamics in a long-range interacting Ising chain. Phys. Rev. X, 7:041063, Dec 2017.
- [45] M. Saffman and K. Mølmer. Efficient multiparticle entanglement via asymmetric rydberg blockade. Phys. Rev. Lett., 102:240502, Jun 2009.
- [46] Thomas Amthor, Christian Giese, Christoph S. Hofmann, and Matthias Weidemüller. Evidence of antiblockade in an ultracold Rydberg gas. Physical Review Letters, 104(1):13001, 2010.
- [47] Mark Saffman, Thad G Walker, and Klaus Mølmer. Quantum information with rydberg atoms. Reviews of Modern Physics, 82(3):2313, 2010.
- [48] N. Henkel, R. Nath, and T. Pohl. Three-Dimensional Roton Excitations and Supersolid Formation in Rydberg-Excited Bose-Einstein Condensates. Phys. Rev. Lett., 104, (2010).
- [49] G. Pupillo, A. Micheli, M. Boninsegni, I. Lesanovsky, and P. Zoller. Strongly correlated gases of Rydberg-dressed atoms: Quantum and classical dynamics. Phys. Rev. Lett., 104, (2010).
- [50] F. Cinti, P. Jain, M. Boninsegni, A. Micheli, P. Zoller, and G. Pupillo. Supersolid droplet crystal in a dipole-blockaded gas. Phys. Rev. Lett., 105, (2010).
- [51] J. Honer, H. Weimer, T. Pfau, and H. P. Büchler. Collective Many-Body Interaction in Rydberg Dressed Atoms. Phys. Rev. Lett., 105(October), (2010).
- [52] C. Gaul, B. J. DeSalvo, J. A. Aman, F. B. Dunning, T. C. Killian, and T. Pohl. Resonant Rydberg-dressing of alkaline-earth atoms via electromagnetically induced transparency. arXiv:1511.06424, (2015).
- [53] Y.-Y. Jau, A. M. Hankin, T. Keating, I. H. Deutsch, and G. W. Biedermann. Entangling atomic spins with a Rydberg-dressed spin-flip blockade. Nat. Phys., 12:71–74, (2015).
- [54] J. Zeiher, R. van Bijnen, P. Schausz, S. Hild, J. Choi, T. Pohl, I. Bloch, and C. Gross. Many-body interferometry of a Rydberg-dressed spin lattice. Nat. Phys., 12:1095–1099, (2016).

- [55] Marcin Płodzień, Graham Lothead, Julius de Hond, N. J. van Druten, and Servaas Kokkelmans. Rydberg dressing of a one-dimensional bose-einstein condensate. *Phys. Rev. A*, 95:043606, Apr 2017.
- [56] Axel Griesmaier, Jörg Werner, Sven Hensler, Jürgen Stuhler, and Tilman Pfau. Bose-einstein condensation of chromium. *Phys. Rev. Lett.*, 94:160401, Apr 2005.
- [57] Mingwu Lu, Nathaniel Q. Burdick, Seo Ho Youn, and Benjamin L. Lev. Strongly dipolar bose-einstein condensate of dysprosium. *Phys. Rev. Lett.*, 107:190401, Oct 2011.
- [58] K. Aikawa, A. Frisch, M. Mark, S. Baier, A. Rietzler, R. Grimm, and F. Ferlaino. Bose-Einstein Condensation of Erbium. *Phys. Rev. Lett.*, 108(May):210401, 2012.
- [59] K-K Ni, S Ospelkaus, MHG de Miranda, A Pe'er, B Neyenhuis, JJ Zirbel, S Kotochigova, PS Julienne, DS Jin, and J Ye. A high phase-space-density gas of polar molecules. *Science*, 322(5899):231–235, 2008.
- [60] Johann G. Danzl, Elmar Haller, Mattias Gustavsson, Manfred J. Mark, Russell Hart, Nadia Bouloufa, Olivier Dulieu, Helmut Ritsch, and Hanns-Christoph Nägerl. Reports 100 100. *Science*, 321:1062–1066, 2008.
- [61] J Deiglmayr, A Grochola, M Repp, K Mörtlbauer, C Glück, J Lange, O Dulieu, R Wester, and M Weidemüller. Formation of ultracold polar molecules in the rovibrational ground state. *Phys. Rev. Lett.*, 101:133004, 2008.
- [62] Alexey V. Gorshkov, Salvatore R. Manmana, Gang Chen, Jun Ye, Eugene Demler, Mikhail D. Lukin, and Ana Maria Rey. Tunable superfluidity and quantum magnetism with ultracold polar molecules. *Phys. Rev. Lett.*, 107:115301, Sep 2011.
- [63] Bo Yan, Steven A Moses, Bryce Gadway, Jacob P Covey, Kaden R A Hazzard, Ana Maria Rey, Deborah S Jin, and Jun Ye. Observation of dipolar spin-exchange interactions with lattice-confined polar molecules. *Nature*, 501:521–525, 2013.
- [64] L. Santos, G. V. Shlyapnikov, P. Zoller, and M. Lewenstein. Bose-Einstein condensation in trapped dipolar gases. *Phys. Rev. Lett.*, 85:1791–1794, 2000.
- [65] J. B. Balewski, A. T. Krupp, A. Gaj, S. Hofferberth, R. Löw, and T. Pfau. Ryd-

berg dressing: Understanding of collective many-body effects and implications for experiments. New J. Phys., 16, (2014).

- [66] Tony E. Lee, H. Häffner, and M. C. Cross. Collective quantum jumps of Rydberg atoms. Phys. Rev. Lett., 108, (2012).
- [67] A. W. Glaetzle, R. Nath, B. Zhao, G. Pupillo, and P. Zoller. Driven-dissipative dynamics of a strongly interacting Rydberg gas. Phys. Rev. A, 86, (2012).
- [68] C. Ates, B. Olmos, J. P. Garrahan, and I. Lesanovsky. Dynamical phases and intermittency of the dissipative quantum Ising model. Phys. Rev. A, 85(4), (2012).
- [69] C. Carr, R. Ritter, C.G Wade, C. S Adams, and K. J Weatherill. Nonequilibrium phase transition in a dilute Rydberg ensemble. Phys. Rev. Lett., 111(11), (2013).
- [70] H. Schempp, G. Günter, M. Robert-de Saint-Vincent, C. S. Hofmann, D. Breyel, A. Komnik, D. W. Schönleber, M. Gärtner, J. Evers, S. Whitlock, and M. Weidemüller. Full counting statistics of laser excited Rydberg aggregates in a one-dimensional geometry. Phys. Rev. Lett., 112(1), (2014).
- [71] N. Malossi, M. M. Valado, S. Scotto, P. Huillery, P. Pillet, D. Ciampini, E. Arimondo, and O. Morsch. Full counting statistics and phase diagram of a dissipative Rydberg gas. Phys. Rev. Lett., 113(2):1–5, (2014).
- [72] A. Urvoy, F. Ripka, I. Lesanovsky, D. Booth, J. P. Shaffer, T. Pfau, and R. Löw. Strongly correlated growth of Rydberg aggregates in a vapor cell. Phys. Rev. Lett., 114(20), (2015).
- [73] M. M. Valado, C. Simonelli, M. D. Hoogerland, I. Lesanovsky, J. P. Garrahan, E. Arimondo, D. Ciampini, and O. Morsch. Experimental observation of controllable kinetic constraints in a cold atomic gas. Phys. Rev. A, 93, 2016.
- [74] S. Helmrich, A. Arias, and S. Whitlock. Uncovering the nonequilibrium phase structure of an open quantum spin system. Phys. Rev. A, 98:022109, Aug 2018.
- [75] C. Ates, T. Pohl, T. Pattard, and J. M. Rost. Antiblockade in rydberg excitation of an ultracold lattice gas. Phys. Rev. Lett., 98:023002, Jan 2007.

- [76] P. Bak, C. Tang, and K. Wiesenfeld. Self-organized criticality: An explanation of the $1/f$ noise. Phys. Rev. Lett., 59:381–384, Jul 1987.
- [77] Matteo Marcuzzi, Michael Buchhold, Sebastian Diehl, and Igor Lesanovsky. Absorbing state phase transition with competing quantum and classical fluctuations. Phys. Rev. Lett., 116:245701, Jun 2016.
- [78] M. Buchhold, B. Everest, M. Marcuzzi, I. Lesanovsky, and S. Diehl. Nonequilibrium effective field theory for absorbing state phase transitions in driven open quantum spin systems. Phys. Rev. B, 95:014308, Jan 2017.
- [79] S. de Léséleuc, D. Barredo, V. Lienhard, A. Browaeys, and T. Lahaye. Analysis of imperfections in the coherent optical excitation of single atoms to Rydberg states. Phys. Rev. A, 97:053803, May 2018.
- [80] J. Zeiher, R. van Bijnen, P. Schauß, S. Hild, J. Choi, T. Pohl, I. Bloch, and C. Gross. Many-body interferometry of a Rydberg-dressed spin lattice. Nat. Phys., 12(12):1095–1099, 2016.
- [81] M. J. Martin, M. Bishof, M. D. Swallows, X. Zhang, C. Benko, J. von Stecher, A. V. Gorshkov, A. M. Rey, and J. Ye. A quantum many-body spin system in an optical lattice clock. Science, 341(6146):632–636, 2013.
- [82] J. Nipper, J. B. Balewski, A. T. Krupp, S. Hofferberth, R. Löw, and T. Pfau. Atomic pair-state interferometer: Controlling and measuring an interaction-induced phase shift in Rydberg-atom pairs. Phys. Rev. X, 2:031011, Aug 2012.
- [83] Kaden R a Hazzard, Bryce Gadway, Michael Foss-Feig, Bo Yan, Steven a Moses, Jacob P Covey, Norman Y Yao, Mikhail D Lukin, Jun Ye, Deborah S Jin, and Ana Maria Rey. Many-body dynamics of dipolar molecules in an optical lattice. Physical Review Letters, 113:195302, 2014.
- [84] M. Ebert, M. Kwon, T. G. Walker, and M. Saffman. Coherence and Rydberg blockade of atomic ensemble qubits. Phys. Rev. Lett., 115:093601, Aug 2015.
- [85] N. Takei, C. Sommer, C. Genes, G. Pupillo, H. Goto, K. Koyasu, H. Chiba, M. Weidemüller, and K. Ohmori. Direct observation of ultrafast many-body electron dynamics in an ultracold Rydberg gas. Nat. Commun., 7:13449, 2018.

- [86] C. Cohen-Tannoudji, J. Dupont-Roc, and G. Grynberg. Atom-Photon Interactions: Basic Processes and Applications. Wiley-VCH, (1998).
- [87] H. Mabuchi and A. C. Doherty. Cavity quantum electrodynamics: coherence in context. Science, 298:1372–1377, (2002).
- [88] S. Haroche. Nobel lecture: Controlling photons in a box and exploring the quantum to classical boundary. Rev. Mod. Phys., 85(3):1083, (2013).
- [89] I. Bloch, J. Dalibard, and W. Zwerger. Many-body physics with ultracold gases. Rev. Mod. Phys., 80:885, (2008).
- [90] M. Lewenstein, A. Sanpera, V. Ahufinger, B. Damski, A. Sen, and U. Sen. Ultracold atomic gases in optical lattices: mimicking condensed matter physics and beyond. Adv. Phys., 56:243–379, (2007).
- [91] A. D. Ludlow, M. M. Boyd, J. Ye, E. Peik, and P. O. Schmidt. Optical atomic clocks. Rev. Mod. Phys., 87(2):637, (2015).
- [92] P. Gill. When should we change the definition of the second? Phil. Trans. R. Soc. A, 369(1953):4109–4130, 2011.
- [93] F. Riehle. Towards a redefinition of the second based on optical atomic clocks. Comptes Rendus Physique, 16(5):506–515, 2015.
- [94] J. A. Jones, S. D. Karlen, J. Fitzsimons, A. Ardavan, S. C. Benjamin, G. A. D. Briggs, and J. J. L. Morton. Magnetic field sensing beyond the standard quantum limit using 10-spin noon states. Science, 324(5931):1166–1168, 2009.
- [95] O. Hosten, N. J. Engelsen, R. Krishnakumar, and M. A. Kasevich. Measurement noise 100 times lower than the quantum-projection limit using entangled atoms. Nature, 529(7587):505, 2016.
- [96] A. Tauschinsky, R. M. T. Thijssen, S. Whitlock, H. B. van Linden van den Heuvell, and R. J. C. Spreeuw. Spatially resolved excitation of Rydberg atoms and surface effects on an atom chip. Phys. Rev. A, 81(6):063411, (2010).
- [97] R. P. Abel, C. Carr, U. Krohn, and C. S. Adams. Electrometry near a dielectric surface using Rydberg electromagnetically induced transparency. Phys. Rev. A, 84(2), (2011).

- [98] H. Hattermann, M. Mack, F. Karlewski, F. Jessen, D. Cano, and J. Fortágh. Detrimental adsorbate fields in experiments with cold Rydberg gases near surfaces. *Phys. Rev. A*, 86(2), (2012).
- [99] T. Thiele, J. Deiglmayr, M. Stammeier, J.-A. Agner, H. Schmutz, F. Merkt, and A. Wallraff. Imaging electric fields in the vicinity of cryogenic surfaces using Rydberg atoms. *Phys. Rev. A*, 92(6), (2015).
- [100] M. G. Bason, M. Tanasittikosol, A. Sargsyan, A. K. Mohapatra, D. Sarkisyan, R. M. Potvliege, and C. S. Adams. Enhanced electric field sensitivity of rf-dressed Rydberg dark states. *New J. Phys.*, 12(6), (2010).
- [101] J. A. Sedlacek, A. Schwettmann, H. Kübler, R. Low, T. Pfau, and J.P. Shaffer. Microwave electrometry with Rydberg atoms in a vapour cell using bright atomic resonances. *Nat. Phys.*, 8:819–824, (2012).
- [102] I. Bouchoule and K. Mølmer. Spin squeezing of atoms by the dipole interaction in virtually excited Rydberg states. *Phys. Rev. A*, 65(4), (2002).
- [103] L. I. R. Gil, R. Mukherjee, E. M. Bridge, M. P. A. Jones, and T. Pohl. Spin squeezing in a Rydberg lattice clock. *Phys. Rev. Lett.*, 112, (2014).
- [104] M H Anderson, J R Ensher, M R Matthews, C E Wieman, and E A Cornell. Observation of bose-einstein condensation in a dilute atomic vapor. *Science*, 269(JULY):198–201, 1995.
- [105] K. B. Davis, M. O. Mewes, M. R. Andrews, N. J. Van Druten, D. S. Durfee, D. M. Kurn, and W. Ketterle. Bose-Einstein condensation in a gas of sodium atoms. *Phys. Rev. Lett.*, 75(November):3969–3973, 1995.
- [106] C. C. Bradley, C. A. Sackett, J. J. Tollett, and R. G. Hulet. Evidence of Bose-Einstein condensation in an atomic gas with attractive interactions. *Phys. Rev. Lett.*, 75(9):1687–1690, 1995.
- [107] Markus Greiner, Cindy A. Regal, and Deborah S. Jin. Emergence of a molecular Bose–Einstein condensate from a Fermi gas. *Nature*, 426(6966):537–540, 2003.
- [108] S. Jochim, M. Bartenstein, A. Altmeyer, G. Hendl, S. Riedl, C. Chin, J. Hecker Denschlag, and R. Grimm. Bose-Einstein Condensation of Molecules. *Science*, 302(5653):2101–2103, dec 2003.

- [109] M W Zwierlein, C A Stan, C H Schunck, S M F Raupach, S Gupta, Z Hadzibabic, and W Ketterle. Observation of Bose-Einstein condensation of molecules. Phys. Rev. Lett., 91(December):250401, 2003.
- [110] E. Dagotto. Complexity in Strongly Correlated Electronic Systems. Science, 309(5732):257–262, jul 2005.
- [111] P. G. de Gennes and J. Prost. The Physics of Liquid Crystals. Oxford University Press, International Series of Monographs on Physics 83, 1993.
- [112] J Deiglmayr, A Grochola, M Repp, O Dulieu, R Wester, and M Weidemüller. Permanent dipole moment of LiCs in the ground state. Phys. Rev. A, 82(3):32503, 2010.
- [113] Tetsu Takekoshi, Lukas Reichsöllner, Andreas Schindewolf, Jeremy M Hutson, C Ruth Le Sueur, Olivier Dulieu, Francesca Ferlaino, Rudolf Grimm, and Hanns-Christoph Nägerl. Ultracold dense samples of dipolar rbc molecules in the rovibrational and hyperfine ground state. Phys. Rev. Lett., 113(20):205301, 2014.
- [114] T Lahaye, C Menotti, L Santos, M Lewenstein, and T Pfau. The physics of dipolar bosonic quantum gases. Rep. Prog. Phys., 72:71, 2009.
- [115] J. Stuhler, A. Griesmaier, T. Koch, M. Fattori, T. Pfau, S. Giovanazzi, P. Pedri, and L. Santos. Observation of Dipole-Dipole Interaction in a Degenerate Quantum Gas. Phys. Rev. Lett., 95(October):150406, 2005.
- [116] Mingwu Lu, Nathaniel Q. Burdick, and Benjamin L. Lev. Quantum Degenerate Dipolar Fermi Gas. Phys. Rev. Lett., 108(21):215301, 2012.
- [117] D. Leibfried, R. Blatt, C. Monroe, and D. Wineland. Quantum dynamics of single trapped ions. Rev. Mod. Phys., 75:281–324, Mar 2003.
- [118] Rainer Blatt and Christian F Roos. Quantum simulations with trapped ions. Nature Physics, 8(4):277, 2012.
- [119] Thomas F Gallagher. Rydberg atoms, volume 3. Cambridge University Press, 2005.
- [120] M. Saffman, T. G. Walker, and K. Mølmer. Quantum information with Rydberg atoms. Rev. Mod. Phys., 82, (2010).

- [121] Hendrik Weimer, Markus Müller, Igor Lesanovsky, Peter Zoller, and Hans Peter Büchler. A Rydberg quantum simulator. *Nature Physics*, 6(5):382–388, 2010.
- [122] S Helmrich, A Arias, N Pehoviak, and S Whitlock. Two-body interactions and decay of three-level Rydberg-dressed atoms. *J. Phys. B*, 49(3):03LT02, (2016).
- [123] C.-J. Lorenzen and K. Niemax. Quantum defects of the $n^2P_{1/2,3/2}$ levels in ^{39}K I and ^{85}Rb I. *Physica Scripta*, 27:300–305, (1983).
- [124] Woldemar Voigt. Ueber das elektrische analogon des zeemaneffectes. *Annalen der Physik*, 309(1):197–208, 1901.
- [125] Johannes Stark. Beobachtungen über den effekt des elektrischen felde auf spektrallinien. i. quereffekt. *Annalen der Physik*, 348(7):965–982, 1914.
- [126] A. Facon, E. Dietsche, D. Grosso, S. Haroche, J. Raimond, M. Brune, and S. Gleyzes. A sensitive electrometer based on a Rydberg atom in a Schrödinger-cat state. *Nature*, 535(7611):262, 2016.
- [127] Ying Wu and Xiaoxue Yang. Strong-coupling theory of periodically driven two-level systems. *Physical review letters*, 98(1):013601, 2007.
- [128] Heinz-Peter Breuer, Francesco Petruccione, et al. *The theory of open quantum systems*. Oxford University Press on Demand, 2002.
- [129] Goran Lindblad. On the generators of quantum dynamical semigroups. *Communications in Mathematical Physics*, 48(2):119–130, 1976.
- [130] Michael Fleischhauer and Jonathan P Marangos. Electromagnetically induced transparency: Optics in coherent media. *Rev. Mod. Phys.*, 77(April):633–673, 2005.
- [131] Ashok K Mohapatra, Mark G Bason, Björn Butscher, Kevin J Weatherill, and Charles S Adams. A giant electro-optic effect using polarizable dark states. *Nature physics*, 4(11):890, 2008.
- [132] Lene Vestergaard Hau, Stephen E Harris, Zachary Dutton, and Cyrus H Behroozi. Light speed reduction to 17 metres per second in an ultracold atomic gas. *Nature*, 397(6720):594, 1999.
- [133] Chien Liu, Zachary Dutton, Cyrus H Behroozi, and Lene Vestergaard Hau.

Observation of coherent optical information storage in an atomic medium using halted light pulses. Nature, 409(6819):490, 2001.

- [134] D. F. Phillips, A. Fleischhauer, A. Mair, R. L. Walsworth, and M. D. Lukin. Storage of light in atomic vapor. Phys. Rev. Lett., 86:783–786, Jan 2001.
- [135] M Bajcsy, Alexander S Zibrov, and Mikhail D Lukin. Stationary pulses of light in an atomic medium. Nature, 426(6967):638, 2003.
- [136] John David Jackson. Classical electrodynamics, 1999.
- [137] Julian Schwinger, Lester L DeRaad Jr, Kimball Milton, and Wu-yang Tsai. Classical electrodynamics. Westview Press, 1998.
- [138] Th. Förster. Zwischenmolekulare energiewanderung und fluoreszenz. Annalen der Physik, 437(1-2):55–75.
- [139] Daniel Tiarks, Simon Baur, Katharina Schneider, Stephan Dürr, and Gerhard Rempe. Single-photon transistor using a förster resonance. Phys. Rev. Lett., 113:053602, Jul 2014.
- [140] Martin Gärttner, Kilian P. Heeg, Thomas Gasenzer, and Jörg Evers. Dynamic formation of rydberg aggregates at off-resonant excitation. Phys. Rev. A, 88:043410, Oct 2013.
- [141] Igor Lesanovsky and Juan P. Garrahan. Kinetic constraints, hierarchical relaxation, and onset of glassiness in strongly interacting and dissipative Rydberg gases. Phys. Rev. Lett., 111:215305, Nov 2013.
- [142] C. Simonelli, M. M. Valado, G. Masella, L. Asteria, E. Arimondo, D. Ciampini, and O. Morsch. Seeded excitation avalanches in off-resonantly driven Rydberg gases. J. Phys. B: At. Mol. Opt. Phys., 49:154002, 2016.
- [143] J. E. Johnson and S. L. Rolston. Interactions between Rydberg-dressed atoms. Phys. Rev. A, 82:033412, 2010.
- [144] Andreas Geißler, Ivana Vasić, and Walter Hofstetter. Condensation versus long-range interaction: Competing quantum phases in bosonic optical lattice systems at near-resonant rydberg dressing. Phys. Rev. A, 95:063608, Jun 2017.

- [145] Xiaopeng Li and S Das Sarma. Exotic topological density waves in cold atomic Rydberg-dressed fermions. Nature Communications, 6(May):7137, 2015.
- [146] T. Keating, R. L. Cook, A. M. Hankin, Y. Jau, G. W. Biedermann, and I. H. Deutsch. Robust quantum logic in neutral atoms via adiabatic Rydberg dressing. Phys. Rev. A, 91:012337, Jan 2015.
- [147] Alexander W Glaetzle, Rick MW van Bijnen, Peter Zoller, and Wolfgang Lechner. A coherent quantum annealer with rydberg atoms. Nature Communications, 8:15813, 2017.
- [148] E. A. Goldschmidt, T. Boulier, R. C. Brown, S. B. Koller, J. T. Young, A. V. Gorshkov, S. L. Rolston, and J. V. Porto. Anomalous broadening in driven dissipative Rydberg systems. Phys. Rev. Lett., 116:113001, 2016.
- [149] J. A. Aman, B. J. DeSalvo, F. B. Dunning, T. C. Killian, S. Yoshida, and J. Burgdörfer. Trap losses induced by near-resonant Rydberg dressing of cold atomic gases. Phys. Rev. A, 93:043425, Apr 2016.
- [150] H. Schempp, G. Günter, S. Wüster, M. Weidemüller, and S. Whitlock. Correlated exciton transport in Rydberg-dressed-atom spin chains. Phys. Rev. Lett., 115:093002, Aug 2015.
- [151] A. W. Glaetzle, R. Nath, B. Zhao, G. Pupillo, and P. Zoller. Driven-dissipative dynamics of a strongly interacting Rydberg gas. Phys. Rev. A, 86:043403, 2012.
- [152] B. Zhao, A. W. Glaetzle, G. Pupillo, and P. Zoller. Atomic Rydberg reservoirs for polar molecules. Phys. Rev. Lett., 108(19):193007, 2012.
- [153] S. D. Huber and H. P. Büchler. Dipole-Interaction-Mediated Laser Cooling of Polar Molecules to Ultracold Temperatures. Phys. Rev. Lett., 108(May):193006, 2012.
- [154] S. H. Autler and C. H. Townes. Stark effect in rapidly varying fields. Phys. Rev., 100:703–722, Oct 1955.
- [155] Martin Gärttner, Shannon Whitlock, David W. Schönleber, and Jörg Evers. Collective excitation of Rydberg-atom ensembles beyond the superatom model. Phys. Rev. Lett., 113:233002, Dec 2014.

- [156] H. Weimer, R. Löw, T. Pfau, and H. P. Büchler. Quantum critical behavior in strongly interacting Rydberg gases. *Phys. Rev. Lett.*, 101:250601, Dec 2008.
- [157] R. Löw, H. Weimer, U. Krohn, R. Heidemann, V. Bendkowsky, B. Butscher, H. P. Büchler, and T. Pfau. Universal scaling in a strongly interacting Rydberg gas. *Phys. Rev. A*, 80:033422, Sep 2009.
- [158] B. J. DeSalvo, J. A. Aman, C. Gaul, T. Pohl, S. Yoshida, J. Burgdörfer, K. R. A. Hazzard, F. B. Dunning, and T. C. Killian. Rydberg-blockade effects in Autler-Townes spectra of ultracold strontium. *Phys. Rev. A*, 93:022709, Feb 2016.
- [159] C. Ates, T. Pohl, T. Pattard, and J. M. Rost. Many-body theory of excitation dynamics in an ultracold Rydberg gas. *Phys. Rev. A*, 76:013413, Jul 2007.
- [160] M. Hoening, W. Abdussalam, M. Fleischhauer, and T. Pohl. Antiferromagnetic long-range order in dissipative Rydberg lattices. *Phys. Rev. A*, 90:021603, Aug 2014.
- [161] H Schempp, G Günter, M. Robert-De-Saint-Vincent, C S Hofmann, D Breyel, A Komnik, D W Schönleber, M Gärttner, J Evers, S Whitlock, and M Weidemüller. Full counting statistics of laser excited Rydberg aggregates in a one-dimensional geometry. *Physical Review Letters*, 112(1):13002, January 2014.
- [162] M. M. Valado, C. Simonelli, M. D. Hoogerland, I. Lesanovsky, J. P. Garrahan, E. Arimondo, D. Ciampini, and O. Morsch. Experimental observation of controllable kinetic constraints in a cold atomic gas. *Phys. Rev. A*, 93:040701, Apr 2016.
- [163] M. Marcuzzi, J. Schick, B Olmos, and I. Lesanovsky. Effective dynamics of strongly dissipative Rydberg gases. *Journal of Physics A: Mathematical and Theoretical*, 47(48):482001, 2014.
- [164] Lev D Landau. Zur theorie der energieübertragung ii. *Z. Sowjetunion*, 2:46–51, 1932.
- [165] Clarence Zener and Ralph Howard Fowler. Non-adiabatic crossing of energy levels. *Proceedings of the Royal Society of London. Series A, Containing Papers of a Mathematical and Physical Character*, 137(833):696–702, 1932.
- [166] M. Henkel, H. Hinrichsen, and S. Lübeck. *Non-equilibrium Phase Transitions Volume 1*. Springer, 2008.

- [167] Giovanni Gallavotti. Nonequilibrium and irreversibility. Springer, 2014.
- [168] Tobias. M. Wintermantel. In-situ fluorescence imaging of ultracold potassium in an optical trap. Master thesis, University of Heidelberg, 2016.
- [169] N. Pehoviak. Strongly interacting ultracold potassium atoms via Rydberg dressing. Master thesis, University of Heidelberg, 2015.
- [170] A. Sayer. Fiber-based beam-distribution-system for potassium magneto-optical traps. Bachelor thesis, University of Heidelberg, 2014.
- [171] J. H Shirley. Modulation transfer processes in optical heterodyne saturation spectroscopy. Opt. Lett, 7(11):537–539, (1982).
- [172] Camy G., Borde Ch., and Ducloy M. Heterodyne saturation spectroscopy through frequency modulation of the saturating beam. Opt. Comm., 41(5):325, 1982.
- [173] Silva Mezinska. Sub-Doppler spectroscopy of Rydberg states of potassium. PhD thesis, University of Heidelberg, 2014.
- [174] D. J. McCarron, S. A. King, and S. L. Cornish. Modulation transfer spectroscopy in atomic rubidium. Meas. Sci. Technol, 19(10), (2008).
- [175] G. Faraoni. Nonlinear light propagation through a strongly interacting Rydberg gas. Master thesis, Università di Pisa, 2011.
- [176] T. G. Tiecke. Properties of potassium, 2010.
- [177] B. Höltkemeier. 2D MOT as a source of a cold atom target. Master thesis, University of Heidelberg, 2011.
- [178] Claude Cohen-Tannoudji. Laser cooling and trapping of neutral atoms: theory. Physics Reports, 219(3):153 – 164, 1992.
- [179] G. Salomon, L. Fouché, P. Wang, A. Aspect, P. Bouyer, and T. Bourdel. Gray-molasses cooling of K-39 to a high phase-space density. EPL (Europhysics Letters), 104(6):63002, 2013.
- [180] Dipankar Nath, R Kollengode Easwaran, G. Rajalakshmi, and C. S. Unnikrishnan. Quantum-interference-enhanced deep sub-doppler cooling of ^{39}K atoms in gray molasses. Phys. Rev. A, 88:053407, Nov 2013.

- [181] Rudolf Grimm, Matthias Weidemüller, and Yurii B. Ovchinnikov. Optical dipole traps for neutral atoms. volume 42 of Advances In Atomic, Molecular, and Optical Physics, pages 95 – 170. Academic Press, 2000.
- [182] E. Pavlov. Setup and characterisation of stable optical traps for ultracold potassium. Master thesis, University of Heidelberg, 2016.
- [183] Waseem S Bakr, Jonathon I Gillen, Amy Peng, Simon Fölling, and Markus Greiner. A quantum gas microscope for detecting single atoms in a hubbard-regime optical lattice. Nature, 462(7269):74, 2009.
- [184] Jacob F Sherson, Christof Weitenberg, Manuel Endres, Marc Cheneau, Immanuel Bloch, and Stefan Kuhr. Single-atom-resolved fluorescence imaging of an atomic Mott insulator. Nature, 467(7311):68–72, 2010.
- [185] A. J. Moerdijk, B. J. Verhaar, and A. Axelsson. Resonances in ultracold collisions of ${}^6\text{Li}$, ${}^7\text{Li}$, and ${}^{23}\text{Na}$. Phys. Rev. A, 51:4852–4861, Jun 1995.
- [186] Chiara D’Errico, Matteo Zaccanti, Marco Fattori, Giacomo Roati, Massimo Inguscio, Giovanni Modugno, and Andrea Simoni. Feshbach resonances in ultracold 39 k. New Journal of Physics, 9(7):223, 2007.
- [187] L. Antoni-Micollier, B. Barrett, L. Chichet, G. Condon, B. Battelier, A. Landragin, and P. Bouyer. Generation of high-purity low-temperature samples of ${}^{39}\text{K}$ for applications in metrology. Phys. Rev. A, 96:023608, Aug 2017.
- [188] Alda Arias, Stephan Helmrich, Christoph Schweiger, Lynton Ardizzone, Graham Lohead, and Shannon Whitlock. Versatile, high-power 460 nm laser system for rydberg excitation of ultracold potassium. Opt. Express, 25(13):14829–14839, Jun 2017.
- [189] H. Hirzler. Analysis and reduction of spectral broadening in high resolution Rydberg excitation. Master thesis, University of Heidelberg, 2017.
- [190] P. A. Franken, A. E. Hill, C. W. Peters, and G. Weinreich. Generation of optical harmonics. Phys. Rev. Lett., 7:118–119, Aug 1961.
- [191] A. Koglbauer, P. Würtz, T. Gericke, and H. Ott. A laser system for the excitation of rubidium Rydberg states using second harmonic generation in a PPLN waveguide crystal. Appl. Phys. B, 104(3), (2011).
- [192] C. J. H. Pagett, P. H. Moriya, R. Celistrino Teixeira, R. F. Shiozaki, M. Hem-

merling, and Ph. W. Courteille. Injection locking of a low cost high power laser diode at 461 nm. *Rev. Sci. Instrum.*, 87(5), (2016).

- [193] Y. Hadjar, F. Ducos, and O. Aef. Stable 120-mw green output tunable over 2 thz by a second-harmonic generation process in a ktp crystal at room temperature. *Opt. Lett.*, 25:1367–1369, (2000).
- [194] H. Katori, T. Ido, Y. Isoya, and M. Kuwata-Gonokami. Magneto-Optical Trapping and Cooling of Strontium Atoms down to the Photon Recoil Temperature. *Phys. Rev. Lett.*, 82(6):1116–1119, (1999).
- [195] Jun Ye, H J Kimble, and Hidetoshi Katori. Quantum State Engineering and Precision Metrology Using State-Insensitive Light Traps. *Science*, 320:1734–1738, (2008).
- [196] F. Sorrentino, A. Alberti, G. Ferrari, V. V. Ivanov, N. Poli, M. Schioppo, and G. M. Tino. Quantum sensor for atom-surface interactions below 10 μm . *Phys. Rev. A*, 79(1):1–8, (2009).
- [197] T. M. Weber, T. Niederprüm, T. Manthey, P. Langer, V. Guarrera, G. Barontini, and H. Ott. Continuous coupling of ultracold atoms to an ionic plasma via Rydberg excitation. *Phys. Rev. A*, 86, (2012).
- [198] M. Robert-de Saint-Vincent, C.S. Hofmann, H. Schempp, G. Günter, S. Whitlock, and M. Weidemüller. Spontaneous avalanche ionization of a strongly blockaded Rydberg gas. *Phys. Rev. Lett.*, 110(4):045004, (2013).
- [199] S. Sachdev. *Quantum phase transitions*. Cambridge University Press, Cambridge, second edition, 2011.
- [200] H. Hinrichsen. Non-equilibrium critical phenomena and phase transitions into absorbing states. *Advances in Physics*, 49(7):815–958, 2000.
- [201] S Helmrich, A Arias, G Lothead, M Buchhold, S Diehl, and S Whitlock. Observation of self-organised criticality in an ultracold atomic gas. [arXiv:1806.09931](https://arxiv.org/abs/1806.09931), 2018.
- [202] S. Helmrich. *Phase structure and dynamics of driven-dissipative Rydberg spin systems*. PhD thesis, University of Heidelberg, 2018.
- [203] P. Schauß, J. Zeiher, T. Fukuhara, S. Hild, M. Cheneau, T. Macrì, T. Pohl,

- I. Bloch, and C. Groß. Crystallization in Ising quantum magnets. Science, 347(6229):1455–1458, 2015.
- [204] H. Labuhn, D. Barredo, S. Ravets, S. de Léséleuc, T. Macrì, T. Lahaye, and A. Browaeys. Tunable two-dimensional arrays of single Rydberg atoms for realizing quantum Ising models. Nature, 534:667–670, 2016.
- [205] R. Potvliege and C. Adams. Photo-ionization in far-off-resonance optical lattices. New Journal of Physics, 8(8):163, 2006.
- [206] R. Heidemann, U. Raitzsch, V. Bendkowsky, B. Butscher, R. Löw, L. Santos, and T. Pfau. Evidence for coherent collective Rydberg excitation in the strong blockade regime. Physical Review Letters, 99(16):163601, 2007.
- [207] A. Urvoy, F. Ripka, I. Lesanovsky, D. Booth, J. P. Shaffer, T. Pfau, and R. Löw. Strongly correlated growth of Rydberg aggregates in a vapor cell. Phys. Rev. Lett., 114:203002, May 2015.
- [208] Ricardo Gutiérrez, Cristiano Simonelli, Matteo Archimi, Francesco Castellucci, Ennio Arimondo, Donatella Ciampini, Matteo Marcuzzi, Igor Lesanovsky, and Oliver Morsch. Experimental signatures of an absorbing-state phase transition in an open driven many-body quantum system. Phys. Rev. A, 96:041602, Oct 2017.
- [209] B. Drossel and F. Schwabl. Self-organized critical forest-fire model. Phys. Rev. Lett., 69:1629–1632, Sep 1992.
- [210] J. A. Bonachela and M. A. Muñoz. Self-organization without conservation: true or just apparent scale-invariance? Journal of Statistical Mechanics: Theory and Experiment, 2009(09):P09009, feb 2009.
- [211] R. Dickman, M. A. Muñoz, A. Vespignani, and S. Zapperi. Paths to self-organized criticality. Brazilian Journal of Physics, 30:27 – 41, mar 2000.
- [212] N. W. Watkins, G. Pruessner, S. C. Chapman, N. B. Crosby, and H. J. Jensen. 25 years of self-organized criticality: Concepts and controversies. Space Science Reviews, 198(1):3–44, Jan 2016.
- [213] R. Dickman. Numerical study of a field theory for directed percolation. Phys. Rev. E, 50:4404–4409, Dec 1994.
- [214] I. Dornic, H. Chaté, and M. A. Muñoz. Integration of Langevin equations with

multiplicative noise and the viability of field theories for absorbing phase transitions. Phys. Rev. Lett., 94:100601, Mar 2005.

- [215] M. A. Muñoz, G. Grinstein, R. Dickman, and R. Livi. Critical behavior of systems with many absorbing states. Phys. Rev. Lett., 76:451–454, Jan 1996.
- [216] P. Schauß, M. Cheneau, M. Endres, T. Fukuhara, S. Hild, A. Omran, T. Pohl, C. Gross, S. Kuhr, and I. Bloch. Observation of spatially ordered structures in a two-dimensional Rydberg gas. Nature, 491:87–91, 2012.
- [217] G Günter, H Schempp, M Robert-de Saint-Vincent, V Gavryusev, S Helmrich, C S Hofmann, S Whitlock, and M Weidemüller. Observing the dynamics of dipole-mediated energy transport by interaction-enhanced imaging. Science (New York, N.Y.), 342(6161):954–6, 2013.
- [218] R. Gutiérrez, J. P. Garrahan, and I. Lesanovsky. Self-similar nonequilibrium dynamics of a many-body system with power-law interactions. Phys. Rev. E, 92:062144, Dec 2015.
- [219] C. Pérez-Espigares, M. Marcuzzi, R. Gutiérrez, and I. Lesanovsky. Epidemic dynamics in open quantum spin systems. Phys. Rev. Lett., 119:140401, Oct 2017.
- [220] A. Arias, G. Lochead, T. M. Wintermantel, S. Helmrich, and S. Whitlock. Realization of a rydberg-dressed ramsey interferometer and electrometer. Phys. Rev. Lett., 122:053601, Feb 2019.
- [221] F. Bloch. Nuclear induction. Phys. Rev., 70:460–474, Oct 1946.
- [222] C. Cohen-Tannoudji, B. Diu, and F. Laloe. Quantum Mechanics. Number Bd. 1 in Quantum Mechanics. Wiley, 1991.
- [223] D. Plankensteiner, J. Schachenmayer, H. Ritsch, and C. Genes. Laser noise imposed limitations of ensemble quantum metrology. J. Phys. B: At. Mol. Opt. Phys., 49(24):245501, 2016.
- [224] E. Arimondo, M. Inguscio, and P. Violino. Experimental determinations of the hyperfine structure in the alkali atoms. Rev. Mod. Phys., 49(1):31, 1977.
- [225] J. Dalibard and C. Cohen-Tannoudji. Dressed-atom approach to atomic motion in laser light: the dipole force revisited. J. Opt. Soc. Am. B, 2(11):1707–1720, Nov 1985.

- [226] A. N. Cleland and M. L. Roukes. A nanometre-scale mechanical electrometer. *Nature*, 392(6672):160, 1998.
- [227] J. S. Bunch, A. M. van der Zande, S. S. Verbridge, I. W. Frank, D. M. Tanenbaum, J. M. Parpia, H. G. Craighead, and P. L. McEuen. Electromechanical resonators from graphene sheets. *Science*, 315(5811):490–493, 2007.
- [228] S. Kumar, H. Fan, H. Kübler, J. Sheng, and J. P. Shaffer. Atom-based sensing of weak radio frequency electric fields using homodyne readout. *Scientific reports*, 7:42981, 2017.
- [229] I. Bouchoule and K. Mølmer. Spin squeezing of atoms by the dipole interaction in virtually excited Rydberg states. *Phys. Rev. A*, 65:041803, Apr 2002.
- [230] M. F. Riedel, P. Böhi, Y. Li, T. W. Hänsch, A. Sinatra, and P. Treutlein. Atom-chip-based generation of entanglement for quantum metrology. *Nature*, 464(7292):1170–1173, 2010.
- [231] C. Gross, T. Zibold, E. Nicklas, J. Esteve, and M. K. Oberthaler. Nonlinear atom interferometer surpasses classical precision limit. *Nature*, 464(7292):1165–1169, 2010.
- [232] A. Luis. Nonlinear transformations and the Heisenberg limit. *Physics Letters A*, 329(1):8 – 13, 2004.
- [233] S. Boixo, A. Datta, S. T. Flammia, A. Shaji, E. Bagan, and C. M. Caves. Quantum-limited metrology with product states. *Phys. Rev. A*, 77:012317, Jan 2008.
- [234] H. Bernien, S. Schwartz, A. Keesling, H. Levine, A. Omran, H. Pichler, S. Choi, A. S. Zibrov, M. Endres, M. Greiner, et al. Probing many-body dynamics on a 51-atom quantum simulator. *Nature*, 551(7682):579, 2017.
- [235] C. J. Picken, R. Legaie, K. McDonnell, and J. D. Pritchard. Entanglement of neutral-atom qubits with long ground-Rydberg coherence times. *Quantum Sci. Technol.*, 4(1):015011, 2019.
- [236] D. Wang, M. D. Lukin, and E. Demler. Quantum fluids of self-assembled chains of polar molecules. *Phys. Rev. Lett.*, 97:180413, Nov 2006.
- [237] M. Dalmonte, G. Pupillo, and P. Zoller. One-dimensional quantum liquids with

power-law interactions: The Luttinger staircase. Phys. Rev. Lett., 105:140401, Sep 2010.

- [238] Bo Yan, Steven a. Moses, Bryce Gadway, Jacob P. Covey, Kaden R. a. Hazard, Ana Maria Rey, Deborah S. Jin, and Jun Ye. Observation of dipolar spin-exchange interactions with lattice-confined polar molecules. Nature, 501(7468):521–525, 2013.
- [239] A. de Paz, A. Sharma, A. Chotia, E. Maréchal, J. H. Huckans, P. Pedri, L. Santos, O. Gorceix, L. Vernac, and B. Laburthe-Tolra. Nonequilibrium quantum magnetism in a dipolar lattice gas. Phys. Rev. Lett., 111(November):185305, 2013.
- [240] S. Baier, M. J. Mark, D. Petter, K. Aikawa, L. Chomaz, Z. Cai, M. Baranov, P. Zoller, and F. Ferlaino. Extended Bose-Hubbard models with ultracold magnetic atoms. Science, 352(6282):201–205, 2016.

List of Figures

2.1	Schematic representation of the one- and two-photon excitation process	10
2.2	Schematic representation of the blockade and antiblockade Rydberg effects	14
2.3	Simulation on the two-body interaction and scattering rate for one and two-photon excitation	18
2.4	Analysis of the decay rate and the interaction potential for the two-photon excitation scheme.	20
3.1	Overview of the experimental apparatus	26
3.2	Level scheme of potassium 39 and laser beam frequencies for the MOT	28
3.3	Laser system for laser cooling and trapping	30
3.4	Potassium 39 and potassium 40 in a MOT	31
3.5	Absorption image of potassium 39 in a tight optical dipole trap.	34
3.6	The variable and run controller	36
3.7	Main window of the experimental control program.	37
3.8	Logic box module interface.	39
3.9	Magnetic field nulling	41
3.10	Rabi oscillations between the $ F = 1, m_f = 0\rangle$ and $ F = 2, m_f = 0\rangle$ states	42
3.11	Calibration of the $ F = 1, m_f = 0\rangle$ to $ F = 2, m_f = 0\rangle$ transition	43
3.12	Population transfer efficiency to the $ F = 2, m_f = -2\rangle$ state	44
3.13	Spin polarization sequence	46
3.14	Spin polarization efficiency	47
4.1	Main elements of the laser system used for Rydberg excitation.	50
4.2	Laser system for the fundamental frequency light	52
4.3	Reference cavity for frequency stabilization	54
4.4	Performance of the frequency doubling by the second harmonic generation (SHG) for the two-photon excitation	56
4.5	Wavelength tuning range of the frequency doubled laser spanning from 455 – 463 nm	58
4.6	Linewidth measurement of the fundamental and frequency doubled laser light as a function of time	59
4.7	Relative frequency noise of the 456 nm light within the bandwidth from 100 Hz to 5MHz.	60

4.8	EIT measurement for analysing the long term frequency drift of the 456 nm laser.	61
4.9	Rydberg loss spectrum of ultracold ³⁹ K atoms in a magneto-optical trap.	63
4.10	Zoom in of a group of s-,p-,d- and l > 2-states	64
4.11	Linewidth measurement of the 572 nm laser system	66
4.12	Laser power histogram of the 286 nm laser system	67
4.13	One-photon Rydberg spectroscopy	68
4.14	Spectroscopy of a Rydberg atom in an electric field	69
5.1	Mapping of the experimental system in a pseudo-spin 1/2 model	72
5.2	Studies on loss rate measurements for different Δ and Ω	75
5.3	Power law scaling of the loss rate R as a function of driving strength .	76
5.4	Experimentally measured non-equilibrium phase diagram	78
5.5	Time evolution of a self-organized Rydberg ensemble	83
5.6	Scale invariance of the self-organised stationary state as a function of the driving intensity Ω^2	84
5.7	Response of the self-organised critical state to external perturbations. .	85
6.1	Schematic representation in the Bloch sphere of a Ramsey sequence. .	90
6.2	Schematic representation in the Bloch sphere of a spin echo sequence.	92
6.3	Experimental realization of a Rydberg-dressed Ramsey interferometer .	93
6.4	Example of the expected Ramsey fringes	94
6.5	Measurement of Ramsey fringes	95
6.6	Analysis of the Rydberg induced light shift and laser coupling as a function of the Rydberg dressing laser detuning Δ	97
6.7	Analysis of the dressed Ramsey interferometer regarding the Rydberg-dressed population and coherence decay	99
6.8	Electric field measurement with a Rydberg-dressed interferometer . . .	101
6.9	Determination fo the Rydberg-dressed electrometer sensitivity.	102
7.1	First results on the geometry and motional control of the atoms.	109
A.1	Experimental control program: General structure	115
A.2	The variable and run controlller	116
A.3	Main window of the experimental control program.	117
A.4	Camera module.	118
A.5	Absorption image module	121

List of Tables

2.1	Most relevant properties of Rydberg atoms and their corresponding scaling.	8
-----	--	---

Acknowledgement

I want to thank my boss first of all, for taking me into his research group, I learned a lot from him, felt always welcomed for discussions and enjoyed the group meetings outside the lab environment. Besides the physics background in Rydberg atoms, I owe him my love for whiskey and the motivation to work hard but keep it cool at the same time. A big thanks go also to Markus Oberthaler not only for reading my thesis but also for his authentic interest in discussing the results of this work and his nice suggestions.

To my colleagues in the experiment who enjoyed with me the lab and office work: Stephano, Tobs and Graham. To Stephan: I couldn't be luckier to have you as my colleague, the scientific and personal discussions were always fruitful, I learned from you how not to be German while being German ;). To Tobs: you are the nicest toberone (as Graham would say) in our group. I enjoyed a lot working with you, your presence was the best combination for the east German and the german-wanna be. Thanks for being always so supportive and for letting me stay at your place when I had no where to live :). To Graham: You are the best postdoc I've could ever asked for, thanks for you kind thesis corrections "Alda does not know the difference between proof an prove or between three and tree", I am sorry you had to suffer reading my thesis. Also thanks to all the guys that join the team for short or long periods: Raphael, Christoph, Nils, Henrik, Sayali and Yibo, I enjoyed working with all of you. To all the guys from the QD group and the Pans, thanks for the fruitful discussions. A big thanks goes to the Haitrap team for having adopted me during all these years. The trip to Amsterdam, the lama tour and the uncountable hours spent in the Braüstadel, made my life better. Also your suggestions about writing the introduction in the right way since the beginning made this process so much easier :)

I want to acknowledge all the wonderful people I met during this time in Heidelberg, my beautiful friends! Leah: I am so glad we got to spend quality time together and share a bed ;) all the hours in the gym made me a stronger person, girl look at that body, I work out! :P. Julia: Du bist immer noch die Beste, danke fürs Mitmachen in der Bib, du hast mich richtig motiviert. Ich freue mich auf unsere zukunftige Zeit mit Nora!

Bei Nicole und Familie wollte ich mich auch von Herzen bedanken. Ohne eure Unterstützung vor sieben Jahre (und auch während dessen), wäre alles nicht so einfach gewesen. Danke für die Zahlreiche Momente, ich habe mich immer gefühlt, als ob ich zu Familie gehörte.

A todo mis amigos hispanohablantes tambien les quiero agradecer por todos los buenos momentos vividos. A los pingüinos: no puedo creer lo afortunada que soy de haberlos encontrado en este rincón del mundo, ustedes son como mi familia, los quiero y espero que pronto podamos celebrar juntos! A mi pingüina favorita (claramente siempre hay favoritos :P) Tina le quiero agradecer los fines de semana de relajación "echando pelo", su amor y comprensión en mis momentos de estrés. A mis chilenos preferidos Migue y Fabian también les quiero dedicar unos renglones, en particular por los carretes, las horas de tertulia y la paciencia para enseñarme su espanhol. Los quiero po!

A Ivan tendría que escribirle toda una tesis para expresarle todos mis sentimientos. Gracias por ser la constante de lost a la que siempre puedo referirme cuando me pierdo en el tiempo y por quererme así yo sea difícil y nunca conteste el teléfono. Ese intento fallido del doble con mecánica me dejó algo mucho mejor que un título :) te adoro y te deseo lo mejor con Marie y en el doctorado :*

Mis amigos que están en la distancia también tienen todo mi agradecimiento. En especial a las mujeres que siempre me han apoyado con sus palabras de cariño, esta tesis lleva una especial dedicación para ellas que son ejemplo de emprendimiento, trabajo fuerte, creatividad y responsabilidad. Todo lo que yo espero ser cuando grande :) esto es para Joha, Jelly, la Mona, Tefita y Nohora ustedes son lo máximo. También le quiero agradecer a Javier con quien empezamos este proyecto de aprender física y quien desde el otro lado del oceano siempre ha tenido una palabra de aliento para mi.

Ein grossen Dank habe ich auch für Sebastian: du bist das schönste Ergebnis aus meiner Doktorarbeit ;). Danke für deine Unterstützung und Liebe, dein Vorbild hat mich immer motiviert, und die Korrekturlesen "sounds a bit bullshitty" haben mir geholfen :D. Ich freue mich auf unsere Zukunft zusammen!

El mayor de los agradecimientos es para mis padres, ellos han sido mi motor desde pequeña, gracias a su apoyo pude estudiar física y alcanzar las metas que soñamos juntos. A la mami en especial le agradezco su paciencia y amor, la constancia de estar siempre pendiente de mi y los consejos que me han servido en los momentos complicados. A papi quiero agradecerle su comprensión, la tranquilidad que siempre me transmite y su alegría. Gracias a los dos por creer en mi, en este proyecto de vida que somos los tres. Los amo!

Declaration

I declared that this thesis has been written by myself and that the work has not been submitted for any other degree or professional qualification. I confirm that the work submitted is my own, except of work which has formed part of jointly-authored publications have been included. My contribution and those of other authors have been explicitly indicated.

Heidelberg, February 4, 2019

Alda Lisseth Arias Suarez

